THREE STUDIES OF IMPACT PHENOMENA IN THE SOLAR SYSTEM

By

John E. Chappelow

RECOMMENDED:

Graduate Advisory Committee Chair

Chair, Department of Geology and Geophysics

APPROVED:

Dean, College of Natural Sciences and Mathematics

Dean of the Graduate School

November 14, 2005

Date

THREE STUDIES OF IMPACT PHENOMENA IN THE SOLAR SYSTEM

A

THESIS

Presented to the Faculty

Of the University of Alaska Fairbanks

in Partial Fulfillment of the Requirements

for the Degree of

DOCTOR OF PHILOSOPHY

By

John E. Chappelow

Fairbanks, Alaska

December 2005

Abstract

Meteoritic activity affects every body in the solar system; its effects are ubiquitous and therefore very useful in the exploration of many planetary bodies. This work addresses two different current problems associated with the use of impact phenomena in the study of other planetary bodies in our solar system.

In Chapter 1 of this thesis, an original method of measuring depths and inferring cross-sectional shapes of impact craters using shadows cast within them by the Sun is developed. The method has the advantage of not requiring that the shadow-front pass through the center of the crater, as the current shadow-measuring technique does. It also has considerable advantages over the methods of stereogrammetry, which requires two images taken from different angles, and photoclinometry, which is sensitive to variations in reflectivity. Three examples providing a check of this method against real lunar impact craters, and demonstrating its utility, are provided.

The rest of this work consists of two closely related studies of the effects of Mars's atmosphere, and its variations, on martian impact cratering and meteorite production rates. To date, little account has been taken of these, since the martian atmosphere has been considered too thin to have significant effects. Here, an original approach to the study of large impactor populations, and their effects on planetary surfaces, is developed and applied to Mars. The results show that for small crater sizes (2 m $\leq D \leq$ 250 m) and impactor masses (10^{-1} kg $\leq m \leq 10^{7}$ kg), both processes depend strongly on atmospheric density. Even the current martian atmosphere is dense enough to produce meteorites of over 50 kg, and to substantially reduce small diameter (<30 m) impact cratering. Past, denser atmospheres would have had even greater effects. Therefore, Mars's atmosphere may interfere with surface age estimates based on counts of small craters, and its variations may be reflected in martian impact crater and meteorite populations.

Table of Contents

List of Figures

List of Tables

List of Appendices

Acknowledgements

I would like to thank the following people who have made this work, and my final degree, possible:

My Mother and Father, for Life, the Universe and Everything.

The UVM Physics and Mathematics departments, for completing my Science Jedi training.

Buck Sharpton for the chance to use that training doing exactly the kind of Science I've always wanted to do: exploring the Universe.

Drs. Doug Christensen, Paul Layer, Hans Nielsen and Rob Herrick for taking the time to serve on my graduate committee (Dr. Nielsen for letting my defense cut into beer-drinking time).

Douglas Adams, for writing the ultimate science-geek's favorite book, "The Hitchhiker's Guide to the Galaxy". 42, Doug.

NASA's Planetary Geology and Geophysics Program and Mars Data Analysis Program, whose grants made this thesis possible. This work was supported by NASA Planetary Geology and Geophysics Program grant NAG5-9392 and NASA Mars Data Analysis Program grant NAG5-10605.

Chapter 1
General Introduction

1.1 INTRODUCTION

Meteoritic activity and related processes are ubiquitous in our solar system. From micron-sized micro-meteorites to asteroid-sized dinosaur-killers, every solar system body is subject to the effects of meteoritic bombardment. Thus the effects of meteoritic bombardment represent a useful tool in the study of a wide range of solar system bodies and of the meteoroid population itself. Two processes which have been particularly useful in Planetary Science are impact cratering and meteorite deposition. In this thesis, three outstanding problems related to these impact processes are explored.

1.2 IMPACT CRATER SHAPE AND DEPTH DETERMINATION

Studies of impact crater morphologies, including depth-to-diameter ratio surveys, have been much-used to study planetary surface properties and processes (e.g., Cintala, 1977; Hale and Head, 1980; Sharpton, 1997; Kieniewicz, et al., 2000) as well as the impact process itself (e.g., Oberbeck, 1971; Pike, 1980; Herrick et al., 1997). Widely used methods for determination of crater depths include stereogrammetry, photoclinometry and shadow-length measurement. Of these, the shadow method has certain distinct advantages over the other two. Unlike stereogrammetry the shadow method can be used on single-image photography, and unlike photoclinometry it is not sensitive to variations in albedo. In addition, the shadow method does not require the intensive computations needed to construct stereograms or perform photoclinometry.

However, the currently used shadow method produces none of the impact crater shape information provided by the other two techniques, even though morphological information is contained in crater shadows. It also only yields the 'true' crater depth if the shadow-front passes through the crater center, where the floor is deepest. In the past attempts have been made to circumvent the second of these limitations by choosing from an image only those craters whose shadow tips lie very near the crater center, or by

adding 'guesstimated' corrections to the calculated depths of craters whose shadows do not transect the crater center. But, for any given solar elevation angle, the first approach is equivalent to selecting the depth-to-diameter ratio of the craters to be studied; shallower and deeper craters are excluded. The second approach is based on making the unsupported assumption that the craters to be studied all have the same cross-sectional shape (typically parabolic), then estimating an 'empirical correction factor' to be added to the depth detemined from the shadow length (e.g., Pike, 1980).

Since neither of these approaches is very satisfactory for performing a robust depth-to-diameter survey on a crater population, or for constraining crater morphology, the first purpose of Chapter 2 of this thesis is to develop a more general method of calculating crater depths from the shapes and lengths of shadows cast within them. The second purpose is to discover how crater cross-sectional shape can be constrained from inspection of the shadow shape.

1.3 ATMOSPHERIC EFFECTS ON IMPACT CRATERING ON MARS

Relative age relationships between planetary surfaces can be inferred by the relative abundance of impact craters upon them. When combined with independent age information (e.g., returned samples), crater population statistics can be used to estimate absolute ages by constructing "isochrons", as has been done for the Moon (e.g., Hartmann, 1970; Neukum et al., 2001). These isochrons have been transposed to other planetary bodies, such as Mars, by estimating cratering rates there relative to those on the Moon (e.g., Hartmann, 1977; Hartmann and Neukum, 2001; Ivanov, 2001). Several factors that must be taken into account when determining these relative cratering rates, include differing encounter velocities and impactor populations due to Mars's orbital location, and different impact velocities and cratering dynamics due to Mars's higher gravity.

However, one difference between Mars and the Moon has been largely neglected to this point: the martian atmosphere. The atmosphere affects impact cratering via the processes of ablation, aerobraking and fragmentation, all of which tend to decrease

cratering rates, and therefore have the potential to affect crater-count-based surface dating methods. Until recently, researchers have been primarily interested in crater sizes and impactor masses considered too large to be significantly affected by the current thin (6 mbar), martian atmosphere. Lately this has changed, as instruments of increasing resolution arrive at Mars, such as the Mars Orbiter Camera (MOC), aboard Mars Global Surveyor (MGS), and the upcoming High Resolution Imager and Spectrometer Experiment (HiRISE) instrument aboard Mars Reconnaissance Orbiter (MRO). However, atmospheric effects on martian small-cratering rates (craters that are meters to hundreds of meters in diameter) have still not been meaningfully explored. Therefore, the first goal of Chapter 3 of this work is to quantify the reductions that occur in martian small-cratering rates due to the presence of its atmosphere.

The filtering effects on cratering must depend strongly on the density of the atmosphere encountered by the impacting population, and the martian atmosphere apparently undergoes rapid and drastic obliquity-driven variations in density, corresponding to surface pressure variations between zero and several tens of millibars (Ward, 1974; James et al., 1992). Therefore martian cratering rates must also vary, possibly significantly, over time. Though we currently have no physical evidence of these variations in atmospheric density, the martian cratering record may provide an opportunity to detect them. Populations of small craters are especially well suited for such a purpose, because impact rates are much higher for small objects than for larger ones. Therefore, populations of small craters respond much faster to changes in impact rates than do populations of larger ones. Thus a second goal of Chapter 3 is to investigate how the atmospheric effects on martian impact cratering vary with changes in atmospheric density (or surface pressure).

1.4 ATMOSPHERIC EFFECTS ON MARTIAN METEORITE PRODUCTION

In addition to reducing impact cratering, planetary atmospheres can aerobrake entering objects to low enough velocities that they survive impact and remain on the surface as meteorites. Meteorite falls are well known on Earth, and have been presumed

to occur on Mars as well (e. g., Dycus, 1969; Bland and Smith, 2000). This was recently confirmed when the Mars Exploration Rover (MER) Opportunity discovered that a rock lying on the surface of Terra Meridiani, Mars, is in fact a 50 kg iron meteorite. Like impact cratering, martian meteorite production must depend on the density of Mars's atmosphere, and its variations, so meteorite populations represent another potential, future source of physical evidence for variations in the martian climate.

However meteorite production on Mars has also received little attention in the literature, so far. Dycus, (1969) and Bland and Smith (2000) are two of the only works that address the subject, and they consider only special cases of meteor entry into the martian atmosphere (e.g., vertical entry), not the general problem. And no previous study considers meteorite production under martian atmospheres other than today's.

Thus the primary purpose of Chapter 4 is to investigate the dependence of martian meteorite production rates on Mars's atmospheric density and its variations. The resulting set of martian impactor outcomes vs. entry parameters will also be used to study the dynamics of martian meteorite production in detail. I will address the questions: What ranges of entry parameters may result in meteorites on Mars? What ranges could produce the iron meteorite Heat Shield Rock? How do these ranges depend upon Mars's atmospheric density? What are the other possible fates of objects that enter Mars's atmosphere? Another goal of this Chapter is to compare my results to existing works in this field (i.e., Dycus, (1969), and Bland and Smith (2000)) and, if possible, use them to provide context for these previous works.

I am first author of all three manuscripts included in this thesis. Each has been written in collaboration with my advisor and committee chair, Dr. Buck Sharpton of the University of Alaska Fairbanks' Geophysical Institute.

1.5 REFERENCES

Bland, P. A., Smith, T. B. 2000. Meteorite accumulations on Mars. Icarus 144, 21-26.

Cintala M. J. 1977. Martian fresh crater morphology and morphometry - a pre-Viking review. In Impact and Explosion Cratering (eds. D. Roddy, R. Pepin and R. Merrill), pp. 575-591. Pergamon Press, New York, New York, USA.

Dycus, R. D. 1969. The meteorite flux at the surface of Mars. Pub. Astron. Soc. Pacific 91, 399-414.

Hale W. and Head J. W. 1980. Central peaks in mercurian craters: comparisons to the Moon. Proc. Lunar Planet. Sci. Conf. 11th, 2191-2205.

Hartmann, W. K 1970. Lunar cratering chronology. Icarus 13, 299-301.

Hartmann, W. K 1977. Relative crater production rates on planets. Icarus 31, 260-276.

Hartmann, W. K., Neukum, G. 2001. Cratering chronology and the evolution of Mars. Space Sci. Rev. 96, 165-194.

Herrick R. R., Sharpton V. L., Malin M. C., Lyons S. N., and Feely K. 1997. Morphology and morphometry of impact craters. In Venus II: Geology, Geophysics, Atmosphere and Solar Wind Environment (eds. S. Bougher, D. Hunten and R. Philips), pp.1015-1046. University of Arizona Press, Tucson, Arizona, USA.

Ivanov, B. A. 2001. Mars/Moon cratering rate ratio estimates. Space Sci. Rev. 96, 87-104.

James, P. B., Kieffer, H. H., Paige, D. A. 1992. The seasonal cycle of carbon dioxide on Mars. In: Kieffer, H. H., Jakosky, B. M., Snyder, C. W., Matthews, M. S. (eds.), Mars. U. of Arizona Press, Tucson, 934-968.

Kieniewicz, J. M., Sharpton, V. L., Chappelow, J. E. and Pitiss, S. E. 2000. Properties of martian surfaces from the morphology of small impact craters. Abstract published in supplement to EOS, Transactions, AGU, Vol. 81, no. 48.

Neukum, G., Ivanov, B. A., Hartmann, W. K. 2001. Cratering records in the inner solar system in relation to the lunar reference system. Space Sci. Rev. 96, 55-86.

Oberbeck V. R. 1971. Laboratory simulation of impact cratering with high explosives. J. Geophys. Res. 76, 5732-5749.

Pike R. J. 1980. Control of crater morphology by gravity and target type: Mars, Earth, Moon. Proc. Lunar Planet. Sci. Conf. 11th, 2159-2189.

Sharpton V. L. 1997. Evidence from Magellan for unexpectedly deep complex craters on Venus. In Large Meteorite Impacts and Planetary Evolution (eds. B. Dressler, R. Grieve and V. Sharpton), pp.19-27. Geological Society of America, Boulder, Colorado, USA.

Ward, W. R. 1974. Climatic variations on Mars, 1: Astronomical theory of insolation. J. Geophys. Res. 79, 3375-3386.

Chapter 2
An Improved Shadow Measurement Technique for Constraining the Morphometry of Simple Impact Craters*

2.1 INTRODUCTION

Impact crater morphometry is a powerful tool, which is often relied upon for deriving information about planetary surface evolution (e.g., Cintala, 1977; Hale and Head, 1979, 1980; Sharpton, 1997) and gaining insights into the impact process itself (e.g., Pike, 1980a,b; Oberbeck, 1971; Herrick et al., 1997). Generally, craters are classified according to their shape, which, because of the influence of gravity, is dependent upon crater size (e.g., Melosh, 1980, 1989). At small diameters, morphologically 'fresh' craters are usually simple bowl-shaped depressions with raised rims. The shapes of larger complex craters are affected by late-stage collapse of the original deep craterform, thus producing a final shape characterized typically by terraced walls, a shallow floor, and central structures, such as peaks and one or more concentric rings (e.g., Pike, 1980b; Melosh, 1989). The transitional diameter between simple and complex craters is inversely related to the target body's surface gravity (e.g., Pike and Arthur, 1979; Pike, 1980a); for Earth the transition to the complex craterform occurs at diameters between 2 km and 4 km (e.g., Dence et al., 1977); for the moon, it is between 15 km and 20 km (e.g., Pike, 1971, 1974).

The shape of simple craters is thought to superficially resemble the shape of the original 'transient' crater (e.g., Melosh, 1989), i.e., the initial cavity formed by the effects of excavation and structural displacements of the impacted target. Furthermore, studies have shown that the shapes of simple craters can vary with impact velocity (e.g., Oberbeck, 1971, 1977) and target characteristics (e.g., Quaide and Oberbeck, 1968; Oberbeck, 1977; Mouginis-Mark and Hayashi, 1991), such as strength, presence of layering, etc. Consequently, understanding the morphometry of such features is of particular interest. A classic means of characterizing craters is to measure the rim-to-floor

---

* Chappelow, J. E. and V. L. Sharpton. 2002. Meteoritics and Planetary Science (37), 479-486.

depth as a function of crater diameter. Stereogrammetry (e.g., Pike, 1974; Herrick and Sharpton, 2000) and photoclinometry (e.g., Davis and Soderblom, 1984; Schenk, 1989; Craddock et al., 1997) have both been used to determine crater depths and morphologies, but both methods have limitations. Stereogrammetry requires at least two images of the target area, taken from different angles, making it difficult to apply in general to most of the solid bodies in the solar system. Photoclinometry requires knowledge of the target's photometric function; changes in albedo across a feature can severely affect the accuracy of the resulting measurement. Both of these methods are adversely affected by atmospheric scattering, and by the presence of shadows in images taken at low sun angles.

Cast shadows provide an independent means of measuring crater depths and shadow measurements have been widely used to determine crater depths on many solar system bodies (e.g., Arthur, 1974; Pike, 1980a; Pike and Clow, 1983; Schenk, 1989). This method is complementary to the other methods of constraining crater depths in that it requires only one image and works for images taken at lower sun angles. It is also simple: Consider a simple crater exhibiting a shadow that is exactly half the crater diameter (D) in length as shown in FIG. 2.1. The crater rim-to-floor depth (d) can be determined from the following simple equation

$$d = L/\tan\theta\,, \tag{2.1}$$

or, to get the depth-to-diameter ratio

$$\frac{d}{D} = \frac{L}{D\tan\theta}\,, \tag{2.2}$$

where L is the shadow length, measured from the crater rim to the floor and θ is the solar incidence angle measured from the vertical.

Inspection of FIG. 2.1 shows that this method only measures the true crater depth if the shadow edge passes through the crater center. For this reason crater depth studies usually include only craters in which the shadow edge lies very near the crater center (e.g., Arthur, 1974; Pike, 1980a; Pike and Clow, 1983), typically within $0.05D$-$0.10D$ of

the center, to limit the error due to crater shape. However, this crater selection process itself may produce serious artifacts. Choosing a sample of craters based on whether or not they show shadow lengths approximately equal to $D/2$ is equivalent to artificially constraining the depth-to-diameter ratio, d/D, for any given solar incidence angle. Consider, for example, a case where only simple craters for which $L = D/2 \pm 0.05D$ are measured. The limits on d/D are determined from Equation 2.2 to be

$$\left(\frac{d}{D}\right)_{max} = \frac{0.5D + 0.05D}{D\tan\theta} = \frac{0.55}{\tan\theta} \quad ; \quad \left(\frac{d}{D}\right)_{min} = \frac{0.5D - 0.05D}{D\tan\theta} = \frac{0.45}{\tan\theta} .$$

For a given value of θ, these limits are fixed. Hence, by selecting only those craters whose shadows fall near their centers, all craters that are shallower or deeper than this narrow range of d/D are excluded from the analysis.

A graph of d vs. D for the measured craters will be a straight line population, with an artificial slope of $(2\tan\theta)^{-1}$, because the selection process has excluded craters that do not lie near this line. The conventional $\log(d)$ vs. $\log(D)$ graph will be a straight line with a slope approaching unity -- irrespective of what the actual depth vs diameter trend may be. The scatter of the data about this line will also depend on how much the shadow is allowed to deviate from the crater center point. Narrow limits will result in data that cluster near the regression line with artificially low variances and artificially high regression coefficients.

Some attempts have been made to mitigate this effect by either including craters with shadows that are considerably longer or shorter than $D/2$, or adding an empirical correction factor to the value of d arrived at using Equation 2.1 (e.g., Pike, 1980a). Both methods potentially impart errors that are poorly constrained.

For large enough study areas, or if several images of a smaller study area are available, θ could vary, allowing measurements of craters of various d/D ratios to be made. However in the first case one must assume that the d/D distribution is constant over a large study area, and within any region of approximately constant θ, the only craters measured will still be those with appropriate d/D values. Thus each d/D value will

represent a region of the image. No account is taken for any anomalously deep or shallow craters in a given region, and regional variations in the *d*/*D* distribution will not be seen. In addition, foreshortening of craters may cause severe problems in making measurements, if the images are not ortho-rectified. In the second case, several images of the study area, taken at different incidence angles are required, but are often not available.

Here, we derive a more precise and general method of constraining simple crater depths that does not require the shadow edge to be near the crater center, nor is it limited to any particular size or number of images. The problem of foreshortening may be avoided by using nadir-looking or ortho-rectified images. By assuming reasonable, mathematically simple shapes (paraboloid, cone, flat-floored) for simple craters we can derive equations that describe the shapes of the shadows cast inside them. The shapes of actual shadows can then be used to classify the shapes of simple craters and to constrain the craters' depths.

2.2 SHADOWS IN PARABOLIC CRATERS

Laboratory impact experiments (Oberbeck, 1971, 1977) and morphometric studies of actual impact craters relying upon photogrammetry indicate that simple craters normally are closely approximated by a paraboloid (Oberbeck, 1971) with shape defined by the equation

$$z(r) = A\left(x^2 + y^2\right) = Ar^2, \tag{2.3}$$

where the origin is the center of the crater floor. Herein, the positive z-axis is up, the x-axis is perpendicular to z and points in the direction opposite the solar azimuth, and y forms a right-handed orthogonal coordinate system with x and z. The constant A is arbitrary and r is the perpendicular distance from the z-axis. Evaluating (3) at the point $x = R, y = 0, z = d$ yields $A = d/R^2$. Consequently,

$$z(r) = \frac{d}{R^2}\left(x^2 + y^2\right) = \frac{d}{R^2} r^2, \tag{2.4}$$

where R is the radius of the crater and d its depth.

As shown in FIGS. 2.2 and 2.3, the shaded area of such a simple crater is defined by a solar ray, which passes just over the crater rim at point P (coordinates (x_0, y_0, z_0)) and intersects the crater floor at point Q, (coordinates (x, y, z)). The locations of all such points Q define the shadow boundary. This boundary can be mathematically described by equations of the form $z = z(x, y(x))$, the solution of which will be in the form of Equation 2.4, and $y = y(x)$, which describes the plan view of the shadow. Assuming (1) that the crater rim is perfectly circular and horizontal, with height $z = d$ and (2) that solar rays are parallel, i.e., the crater is far from the sun, I have

$$x_0 = -\sqrt{R^2 - y_0^2} \tag{2.5a}$$

and

$$y_0 = y. \tag{2.5b}$$

Consequently, from Equation 2.4:

$$z = d - \frac{x + \sqrt{R^2 - y^2}}{\tan\theta}. \tag{2.6}$$

Then, combining Equation 2.4 and Equation 2.6 eliminates z from the equation. The result may be written

$$\frac{d\tan\theta}{R^2} x^2 + x - d\tan\theta + \frac{d\tan\theta}{R^2} y^2 = -\sqrt{R^2 - y^2}. \tag{2.7}$$

Equation 2.7, which relates the x and y coordinates of any point on the shadow boundary, has two solutions,

$$y_1(x) = \pm\sqrt{R^2 - x^2} \tag{2.8a}$$

and

$$y_2(x) = \pm\sqrt{R^2 - \left(x + R^2/d\tan\theta\right)^2} = \pm\sqrt{R^2 - (x - x_C)^2}\,, \qquad (2.8b)$$

where

$$x_C = -\left(\frac{R}{d\tan\theta}\right)R = -\left(\frac{D}{4d\tan\theta}\right)D\,. \qquad (2.9)$$

Equations 2.8 fully describe the boundary of the shadow, as viewed from above. Both are circles of radius R in the x-y plane. The first is centered at the origin, coincides with the crater rim and forms the boundary of the shadow in the sunward direction. The other, the shadow boundary circle, forms the rest of the shadow boundary and is centered at $x = x_C$, $y = 0$. The intersection of these circles is the shadowed area (FIG. 2.4).

We can now describe what the shadow looks like and how it evolves as the Sun rises over the crater. At sunrise over the crater θ is 90 degrees, $\tan\theta$ is infinite, and x_C is zero, i.e., the circles described by Equations 2.8 coincide and shadow fills the crater. As the Sun rises, θ and $\tan\theta$ decrease, x_C increases in the negative direction, and the shadow boundary circle shifts in the direction of the Sun. The shadow, bounded by the arcs of the two circles, diminishes (FIG. 2.5a). When $\tan\theta$ falls to R/d in magnitude, x_C becomes $-R$, and the shadow intersects the center of the crater (FIG. 2.5b). This is the special case where the depth calculated from (1) is correct.

Finally, when $\tan\theta$ equals $R/2d$, x_C equals $-2R$, the circles become tangent to each other and the shadow disappears completely (FIG. 2.5d). At this point the solar elevation angle is greater than the slope of the top of the crater rim and the entire interior of the crater is illuminated. This value of θ marks the absolute lower limit of the usefulness of any shadow method of depth determination for parabolic craters because for $\theta < \tan^{-1}(R/2d)$ there is no shadow in the crater.

Shadow length L is simply the distance between point A, at $x = -R$, and point B at $x = x_C + R$ (FIG. 2.4). Consequently,

$$L = 2R - \frac{R^2}{d\tan\theta}$$

and

$$d = \frac{D}{4(1 - L/D)\tan\theta} \tag{2.10}$$

for a parabolic crater.

2.3 SHADOWS IN CONICAL CRATERS

Cone-shaped craters are another common variety of simple crater, possibly caused by relatively low velocity impacts (Oberbeck, 1971). The shape of a conical crater is given by

$$z = \left(d/R\right)\sqrt{x^2 + y^2} \ . \tag{2.11}$$

Inserting this crater shape into Equation 2.6 yields:

$$\left(d/R\right)\tan\theta\sqrt{x^2 + y^2} = d\tan\theta - x + \sqrt{R^2 - y^2} \ . \tag{2.12}$$

The solutions of this equation are the circle

$$x^2 + y^2 = R^2,$$

which represents the rim, and the ellipse

$$\frac{(x - x_C)^2}{\alpha^2 R^2} + \frac{y^2}{R^2} = 1, \tag{2.13}$$

where

$$\alpha = \left[\frac{\left(\frac{d\tan\theta}{R}\right)^2 + 1}{\left(\frac{d\tan\theta}{R}\right)^2 - 1}\right] \tag{2.13a}$$

and

$$x_C = -\frac{2\left(d\tan\theta/R\right)}{\left(d\tan\theta/R\right)^2 - 1}R\,, \tag{2.13b}$$

which forms the other shadow boundary (FIG. 2.6).

As in the circular case, we can now describe the evolution of this shadow with increasing sun angles. As the Sun rises above the crater rim, the ellipse extends along the surface in the illumination direction, becoming increasingly eccentric, as shown in FIG. 2.7. Finally, when $\theta = \tan^{-1}(R/d)$, the solar incidence angle is greater than the slope of the crater walls and the entire crater is illuminated.

Using the same method as in the previous section, we derive an equation for the depth of a conical crater:

$$d = \frac{L}{2(1 - L/D)\tan\theta}. \tag{2.14}$$

2.4 SHADOWS IN CRATERS WITH FLAT BOTTOMS

The effect of a flat bottom on the shadow inside a crater can be seen by considering the parallel rays from a light source (Sun) incident on two parallel planes at some incidence angle θ (FIG. 2.8). The upper plane contains a hole of diameter D and corresponds to the crater rim, while the lower plane represents the flat bottom of the crater. An illuminated circle of diameter D will be projected onto the lower plane, displaced away from the Sun by an amount x_C, where

$$x_C = d'\tan\theta\,,$$

where d' is the separation of the two planes. A flat region at the bottom of a crater will be illuminated in the same way (FIG. 2.9).

2.5 APPLICATIONS

In this section, we illustrate the utility of the shadow analysis technique derived above by examining three lunar craters, as represented in Clementine imagery. We will

use shadow shape to determine the simple shape that most closely fits the crater and then constrain its depth. In all three of the craters (FIGS. 2.10a-c), the crater axes, crater rims and shadow boundary shapes are marked. All images have been rotated so that solar illumination is from the -*y* direction.

The crater in FIG. 2.10a has D = 19,900 m, L = 15,200 m and is illuminated at θ = 82.6°. The circular shadow boundary indicates that the crater is parabolic in shape (compare to FIG. 2.4), so from Equation 2.10, d = 2700 m and d/D is 0.13. Note that d is a maximum depth constraint, because constraints on the parabolic shape only apply to the sunlit portion of the crater interior. Unless additional, higher sun angle imagery is available to determine the conflguration of the shadowed region of the crater bottom, the possibility that the crater floor could flatten out immediately inside the shadowed region cannot be dismissed. In this case, the maximum diameter of a hidden flat bottom would be $D_f = 2L - D$ = 10,500 m and the minimum depth of the crater is given by:

$$d_{min} = \left(1 - \frac{D_f^2}{D^2}\right) d$$

or, more simply, by $d_{min} = L/\tan\theta$ = 2000 m, from Equation 2.1. The minimum value of d/D is 0.10.

The shadow in crater FIG. 2.10b is fit well by an ellipse, not by a circle, showing that it is conical in shape (compare to FIG. 2.7). Its diameter is 15,500 m, L = 9700 m and θ = 72.0°. From Equation 2.14 the maximum depth, d, is 4200 m giving a maximum d/D = 0.27. If a flat floor with the maximum permissible diameter of D_f = 3900 m is assumed, the minimum permissible depth is simply:

$$d_{min} = \left(1 - \frac{D_f}{D}\right) d .$$

Using this equation, or Equation 2.1, the minimum depth is 3100 m, giving a minimum d/D = 0.20. These examples illustrate a limitation of the shadow measurement technique: the farther the shadow extends beyond the crater center the greater the

potential for error due to unseen topography. In both cases the term D_f/D is a measure of the potential error.

FIG. 2.10c shows a crater with a conspicuous flat bottom. The effect of the flat bottom on the shadow shape is clearly visible (compare to FIG. 2.9). The sides of the shadow are best fit with an ellipse, indicating that the crater walls are probably conical, although the limited length of the contact between the shadow and the fit leaves this interpretation open to question. The diameter is 14,100m and the shadow length along the y-axis is 6100m. From (1) the depth is 1600m, giving $d/D = 0.11$. Note in all three of these cases that the shape of the shadow is used only to select the proper crater shape, if any, for the depth calculation. There is no need to actually fit a curve to the shadow edge.

In all three figures, a darkening of the ends of the illuminated crescents inside the crater is apparent. These dark broad 'wings' indicate that rims of real craters are usually rounded and, therefore, deviate from the simple shapes assumed here. The points along the shadow edge, where it begins to broaden, indicate the locations where the wall-rim slopes begin to shallow and rounding begins. This could be a useful morphometric indicatrix: for instance the size of the shadow 'wings' could be used to determine how rounded (and, therefore, how modified) the crater rim is.

2.6 CONCLUSIONS

1. Previously used shadow methods of measuring crater depths suffer from the fact that the currently used formula for the depth is only useful when the shadow boundary passes near to the center of the crater. This method may introduce artifacts, because, for any fixed solar incidence angle, the selection process is equivalent to selecting only craters that fall within a very narrow range of d/D, where d is the depth and D the diameter.
2. Parabolic craters show shadow shapes that are defined by the intersection of two circles, both with diameters equal to the crater rim diameter. The equation for determining the maximum depth of a parabolic crater is

$$d = \frac{D}{4(1 - L/D)\tan\theta},$$

where L is the shadow length and θ the solar incidence angle.

3. Craters with conical walls show shadows that are defined by the intersection of the crater rim and an ellipse whose semi-minor axis is the same as the crater rim diameter and whose semi-major axis is dependent on the solar incidence angle. The maximum of depth a conical crater is given by

$$d = \frac{L}{2(1 - L/D)\tan\theta}.$$

4. The equations for the depths of both of these craters actually represent upper bounds on the depth, since any topography not crossed by the shadow boundary, particularly flat bottoms, cannot be accounted for using this method. When the shadow edge crosses a flat bottom, the simple equation

$$d = \frac{L}{\tan\theta}$$

gives its depth.

2.7 REFERENCES

ARTHUR D. W. G. (1974) Lunar crater depths from Orbiter IV long focus photographs. *Icarus* **23**, 116-122.

CINTALA M. J. (1977) Martian fresh crater morphology and morphometry - a pre-Viking review. In *Impact and Explosion Cratering* (eds. D. Roddy, R. Pepin and R. Merrill), pp. 575-591. Pergamon Press, New York, New York, USA.

CRADDOCK R. A., MAXWELL T. A. AND HOWARD A. D. (1997) Crater morphometry and modification in the Sinus Sabaeus and Margaritifer Sinus regions of Mars. *J. Geophys. Res.* **102E**, 13321-13340.

DAVIS P. A. AND SODERBLOM L. A. (1984) Modeling crater topography and albedo from monoscopic Viking orbiter images. *J. Geophys. Res.* **89**, 9449-9457.

DENCE M. R., GRIEVE R. A. F. AND ROBERTSON P. B. (1977) Terrestrial impact structures: principal characteristics and energy considerations. In *Impact and Explosion Cratering* (eds. D. Roddy, R. Pepin and R. Merrill), pp. 247-275. Pergamon Press, New York, New York, USA.

HALE W. AND HEAD J. W. (1979) Central peaks in lunar craters: morphology and morphometry. *Proc. Lunar Planet. Sci. Conf.* **10th**, 2623-2633.

HALE W. AND HEAD J. W. (1980) Central peaks in mercurian craters: comparisons to the Moon. *Proc. Lunar Planet. Sci. Conf.* **11th**, 2191-2205.

HERRICK R. R. AND SHARPTON V. L. (2000) Implications from stereo-derived topography of Venusian impact craters. *J. Geophys. Res.* **105E**, 20245-20262.

HERRICK R. R., SHARPTON V. L., MALIN M. C., LYONS S. N., AND FEELY K. (1997) Morphology and morphometry of impact craters. In *Venus II: Geology, Geophysics, Atmosphere and Solar Wind Environment* (eds. S. Bougher, D. Hunten and R. Philips), pp.1015-1046. University of Arizona Press, Tucson, Arizona, USA.

MELOSH H. J. (1980) Cratering mechanics--observational, experimental, and theoretical. *Ann. Rev. Earth Planet. Sci.* **8**, 65-93.

MELOSH H. J. (1989) *Impact Cratering: A Geologic Process.* Oxford University Press, New York, New York, USA.

MOUGINIS-MARK P. J. AND HAYASHI J. N. (1991) Depth/diameter relationships of fresh craters within Hesperia Planum, Mars. *NASA Tech. Memo. 4300*, 370-372.

OBERBECK V. R. (1971) Laboratory simulation of impact cratering with high explosives. *J. Geophys. Res.* **76**, 5732-5749.

OBERBECK V. R. (1977) Application of high explosion cratering data to planetary problems. In *Impact and Explosion Cratering* (eds. D. Roddy, R. Pepin and R. Merrill), pp. 45-65. Pergamon Press, New York, New York, USA.

PIKE R. J. (1971) Genetic implications of the shapes of martian and lunar craters. *Icarus* **15**, 384-395.

PIKE R. J. (1974) Depth/diameter relations of fresh lunar craters: revision from spacecraft data. *Geophys. Res. Letters* **1**, 291-294.

PIKE R. J. (1980a) Control of crater morphology by gravity and target type: Mars, Earth, Moon. *Proc. Lunar Planet. Sci. Conf.* **11th**, 2159-2189.

PIKE R. J. (1980b) Formation of complex impact craters: evidence from Mars and other planets. *Icarus* **43**, 1-19.

PIKE R. J. AND ARTHUR D. W. G. (1979) Simple to complex impact craters: the transition on Mars. *NASA Tech. Memo. 80339*, 132-134.

PIKE R. J. AND CLOW G. D. (1983) Ode to gravity: Depth/diameter for fresh craters on Mercury. *NASA Tech. Memo. 86246*, 104-106.

QUAIDE W. L. AND OBERBECK V. R. (1968) Thickness determinations of the lunar surface layer from lunar impact craters. *J. Geophys. Res.* **73**, 5247-5270.

SCHENK P. M. (1989) Crater formation and modification on the icy satellites of Uranus and Saturn: depth/diameter and central peak occurrence. *J. Geophys. Res.* **94**, 3813-3832.

SHARPTON V. L. (1997) Evidence from Magellan for unexpectedly deep complex craters on Venus. In *Large Meteorite Impacts and Planetary Evolution* (eds. B. Dressler, R. Grieve and V. Sharpton), pp.19-27. Geological Society of America, Boulder, Colorado, USA.

2.8 FIGURES:

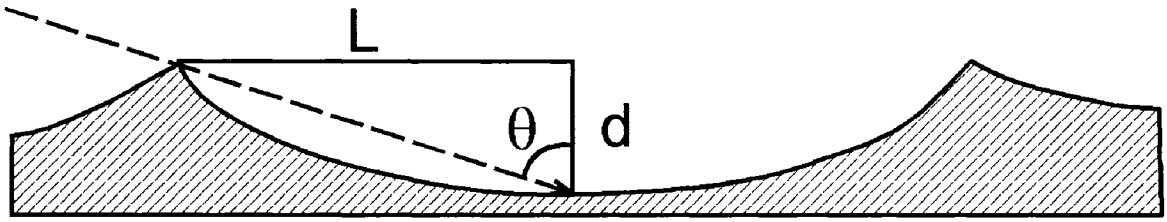

Figure 2.1: An idealized cross section showing a shadow of width D/2. An idealized cross section showing a shadow of width D/2 cast inside a simple crater.

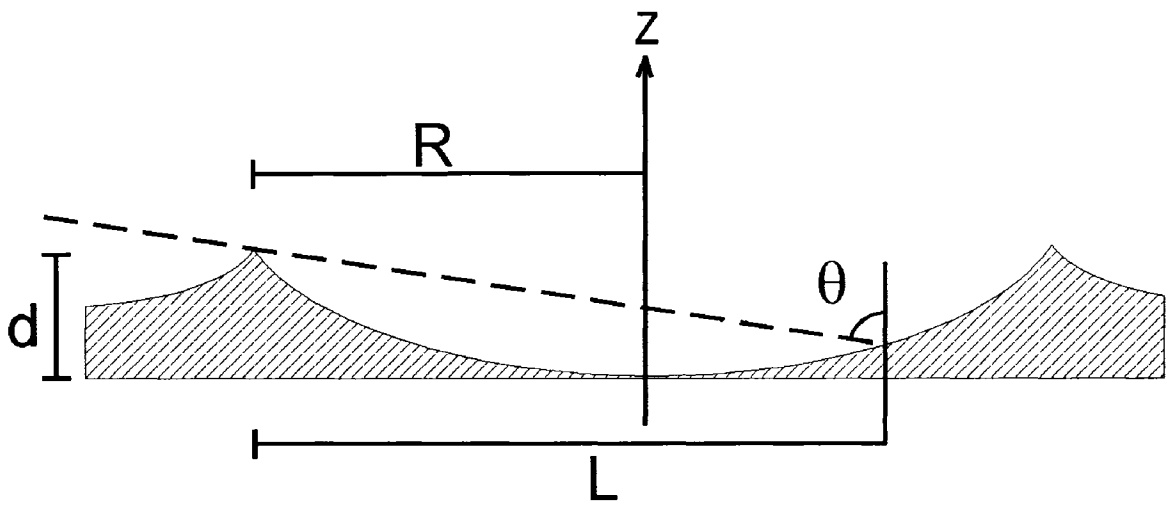

Figure 2.2: Section through a paraboloidal crater.

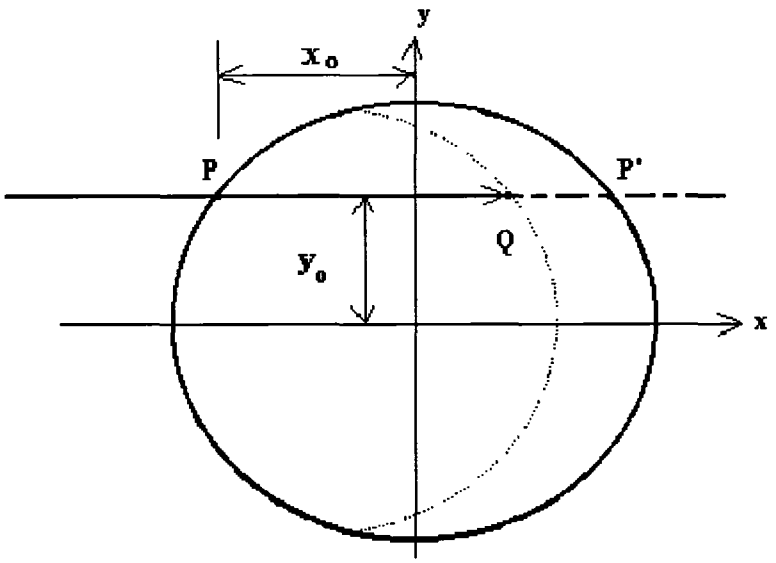

Figure 2.3: Plan view of a solar ray passing just over the crater rim at P.

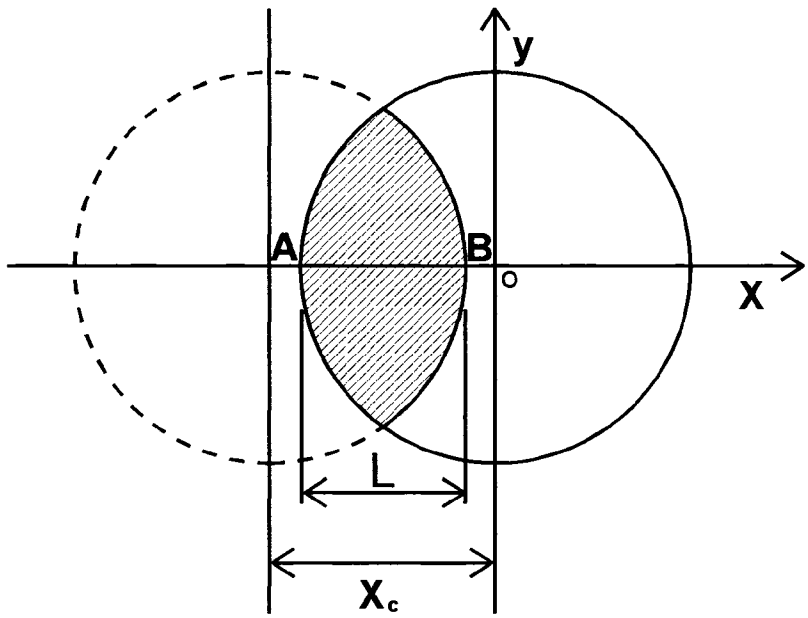

Figure 2.4: Overhead view of the two circles that define the shadow.

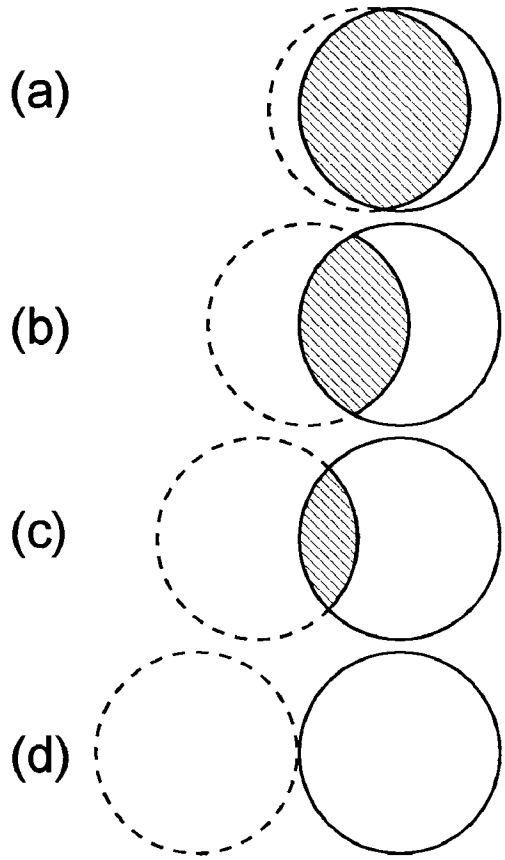

Figure 2.5: Evolution of the shadow as the sun rises.

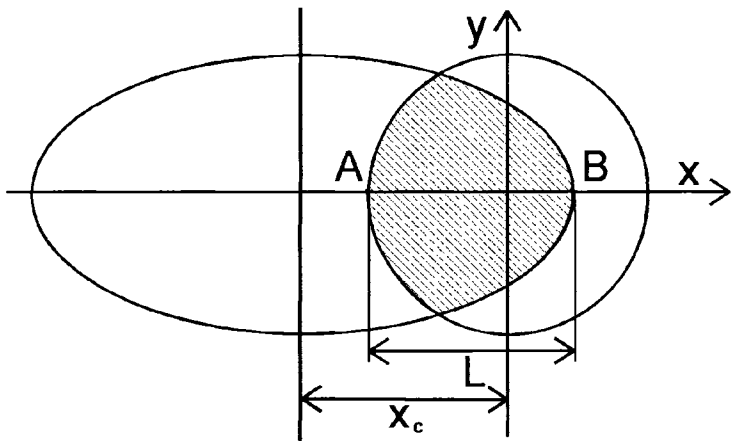

Figure 2.6: Shadow geometry in a cone shaped crater.

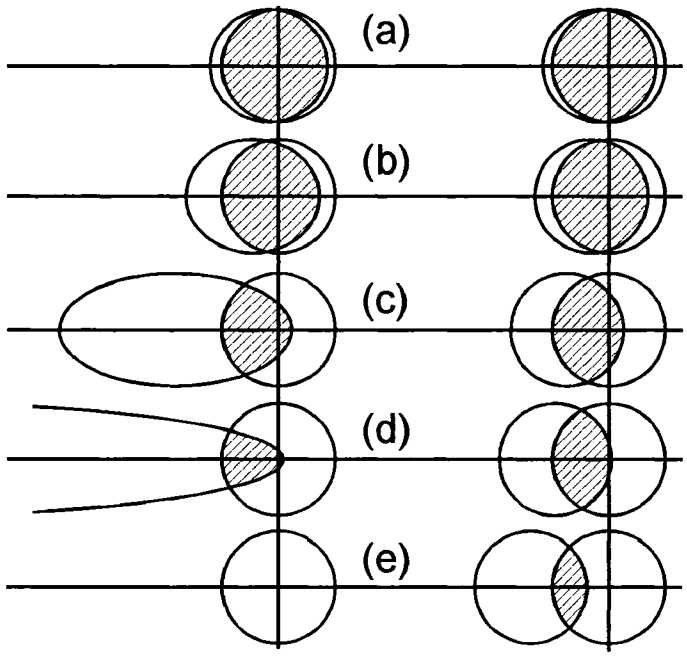

Figure 2.7: Comparison of the shadows in parabolic and conical craters. The solar elevation increases from near-zero (a) to $\tan^{-1}(R/d)$, in (e).

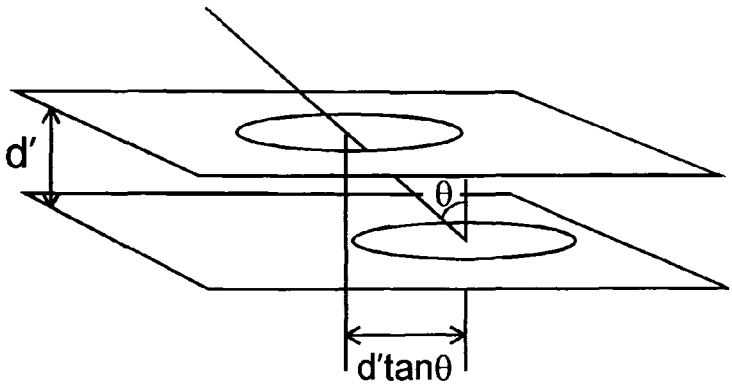

Figure 2.8: Projection of a circle onto a plane.

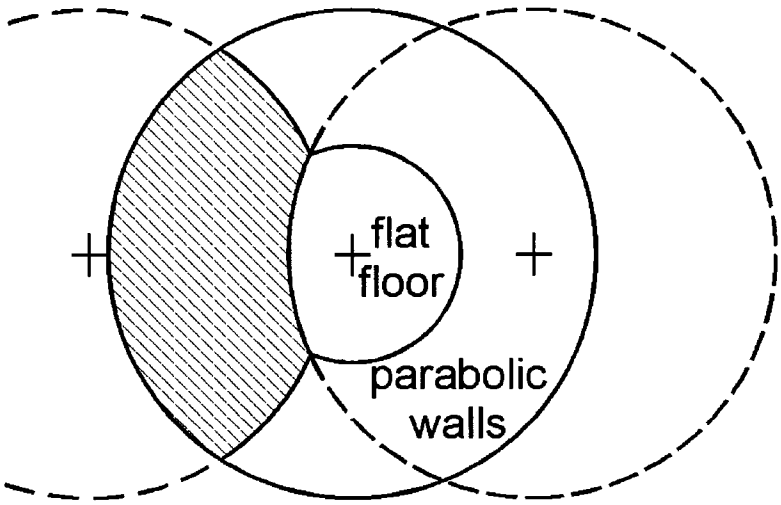

Figure 2.9: Effect of a flat bottom on the shape of the shadow in a parabolic crater.

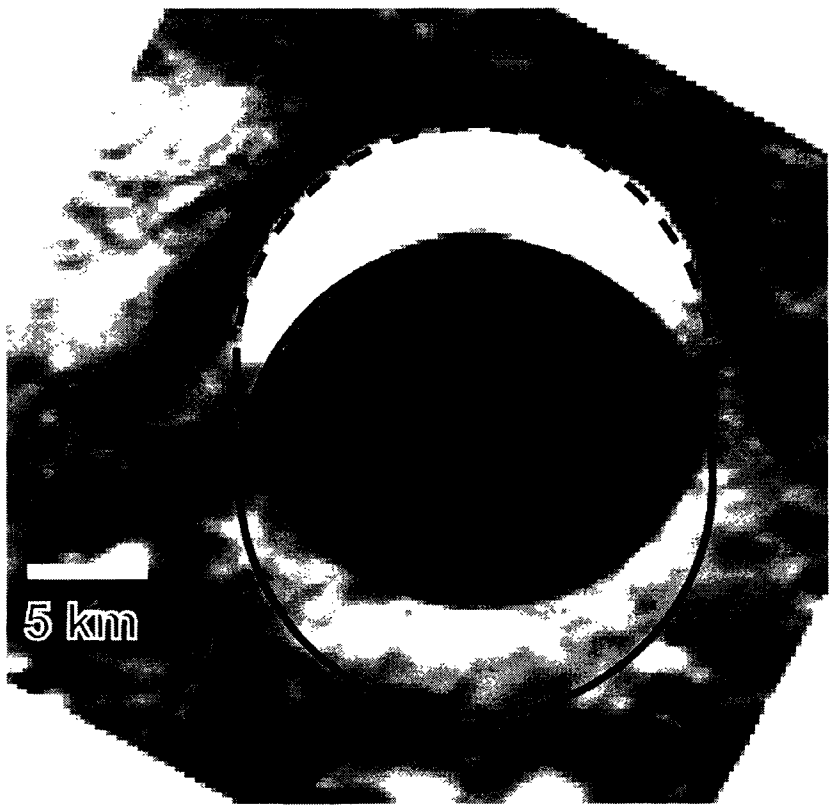

Figure 2.10a: Detail of Clementine image lub4315r.328.

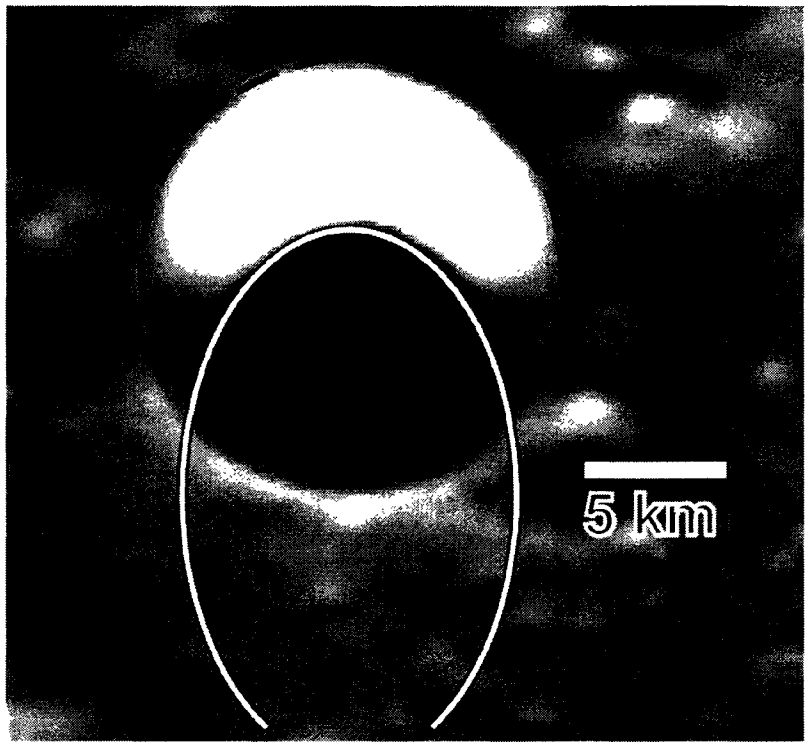

Figure 2.10b: Detail of Clementine image luc5578q.125.

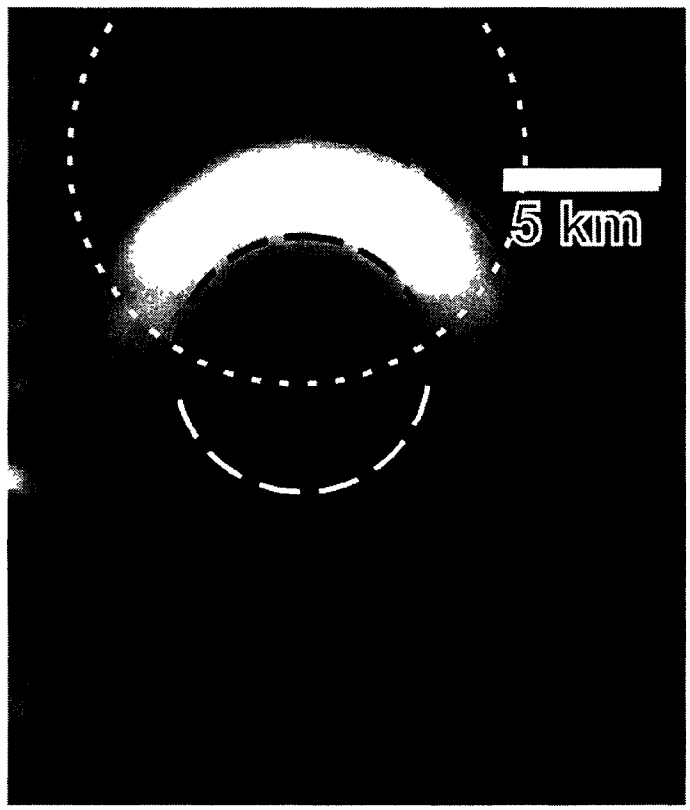

Figure 2.10c: Detail of Clementine image lua0594b.148.

Chapter 3

Influences of Atmospheric Variations on Mars's Record of Small Craters*

3.1 INTRODUCTION

Statistical analysis of impact crater populations is currently the only method available for estimating absolute ages of martian surfaces. Crater size-frequency "isochrons" were originally developed for the Moon (e.g., Hartmann, 1970; Neukum et al., 2001) by combining lunar impact crater populations with isotopic dating of returned samples. They were later transposed to Mars by estimating cratering rates for Mars relative to those of the Moon (e.g., Hartmann, 1977; Hartmann and Neukum, 2001; Ivanov, 2001), a procedure made necessary by the lack of site-specific samples from Mars. Differences occur in martian cratering rates relative to those on the Moon due to the two planets' different orbital positions and masses, and the presence of the martian atmosphere.

Because of Mars's position in an orbit more distant from the Sun than the Earth-Moon system, it encounters a different population of impactors, as described by a mass-frequency law, and encounters these impactors at lower cosmic velocities than does the Moon. Currently the population difference is handled by supposing that the martian impactor population is a simple multiple of the Earth-Moon population

$$N_{Mars}(m) = F_{pop} \times N_{Moon}(m),$$

where N is the number of objects larger than mass m each planet encounters, per unit time, and the multiplying factor, F_{pop}, is greater than unity due to Mars's proximity to the asteroid belt; a currently accepted value seems to be about 2.6 (Crown et al., 2005). This has the effect of shifting the martian isochrons upward relative to those of the Moon (Fig. 3.1) on the standard incremental size-frequency diagram (see Crater Analysis Techniques Working Group, 1979).

---

* Chappelow, J. E. and V. L. Sharpton. 2005. Icarus, in press.

Impact velocities on Mars are different than those on the Moon due to lower meteoroid encounter velocities at Mars's orbit, and to Mars's larger gravitational acceleration. The net effect is that martian impact velocities are generally lower than lunar impact velocities. In addition, Mars's higher surface gravity affects cratering rates, since a higher impact energy is required to raise the gravitational potential energy of material excavated from inside a crater and deposit it as ejecta on the surface, under Mars's higher gravity. These effects tend to further reduce the diameter of crater that would be formed on Mars versus the Moon, for any given impactor. Here again, the assumption is commonly made that the amount by which martian craters are reduced in size by these effects, relative to lunar ones, is a constant factor for all impactors which form simple craters,

$$D_{Mars} = F_{dia} \times D_{Moon},$$

where D is the crater diameter for the reasons given above. This has the effect of shifting the Mars isochrons to the left relative to the the lunar set (Fig. 3.1)

These transpositions displace the martian isochrons relative to the lunar ones, but do not change their slope. The net result is that, for the range of crater diameters of interest in this study (~2-250 m; completely within the range of the "steep branch" of Hartmann (Hartmann, 1999; Ivanov, 2001)), the Mars isochrons lie somewhat below, but still parallel to, the the lunar ones, since the martian crater production function is a simple multiple of that for the Moon. Plotting size-frequency data on top of these isochrons then allows estimation of the absolute crater-retention ages of martian surfaces.

Mars's atmosphere also affects cratering rates, via three main mechanisms: deceleration (often called aerobraking), ablation (burnup), and fragmentation (breakup) of incident impactors. These mechanisms affect cratering rates differently depending upon the properties and velocities of the entering bodies, and the state of the atmosphere.

Assuming that the drag force is much larger than any other forces that may be acting (e.g., gravity), the expression for the acceleration of a mass moving through an atmosphere is

$$dv/dt = -C_D \frac{\rho_{atm} A}{2m} \cdot v^2 \tag{3.1}$$

where C_D is the drag coefficient, ρ_{atm} is the atmospheric density, and A and v are the object's cross sectional area and speed, respectively. Assuming a spherical object, this can also be written in the form

$$dv/dt = -C_D \frac{\rho_{atm}}{2}\left(\frac{9\pi}{16}\right)^{1/3} \cdot m^{-1/3} \rho^{-2/3} \cdot v^2, \tag{3.2}$$

where m is the impactor mass and ρ its density.

Ablation is governed by the equation

$$dm/dt = -C_H \frac{\rho_{atm} A}{2Q} \cdot v^3 \tag{3.3}$$

or

$$dm/dt = -C_H \frac{\rho_{atm}}{2Q}\left(\frac{9\pi}{16}\right)^{1/3} \cdot m^{2/3} \rho^{-2/3} \cdot v^3 \tag{3.4}$$

where C_H is the heat transfer coefficient and Q is the heat of ablation of the meteor. The third equation of motion, governing the trajectory angle of the meteor, θ, as measured from the local horizontal, is:

$$d\theta/dt = \frac{g(z)\cos\theta}{v}$$

where $g(z)$ is the gravity at altitude z. With parameters appropriate to the planet of interest (e.g., gravity, atmospheric profile), integration of these governing equations, by semi-analytical (e.g., Zahnle, 1992; Davis, 1993; Bland and Smith, 2000) or numerical (e.g., Dycus, 1969; Rochelle et al., 1999) means, describes the behavior of objects passing through Mars's atmosphere. Various researchers have employed these methods to study the effects of atmosphere on martian (e.g., Dycus, 1969; Vasavada et al., 1993; Bland and Smith, 2000), as well as venusian (e.g., Zahnle, 1992; Herrick and Phillips, 1994),

terrestrial (e.g., Passey and Melosh, 1980; Chyba et al., 1993) and titanian (e.g., Ip, 1990; Engel et al., 1995) impact cratering.

From Eqs. 3.2 and 3.4 it is clear that the effects of ablation and aerobraking on a meteor depend upon its mass, velocity, entry angle and material properties (density and heat of ablation). We may, therefore, expect that atmospheric effects on cratering will vary for different sizes and types of impactors; for example they will be different for icy, high velocity, cometary-type impactors, than for relatively slower, but much denser, iron objects from the asteroid belt.

The effects of atmospheric breakup on cratering rates are much more difficult to quantify since they depend on the size and unknown structural details of the meteor as well as its material composition. I follow a simple approach wherein break up of an entering meteor occurs when the dynamic pressure, $\frac{1}{2}\rho_{atm}v^2$ (sometimes called stagnation pressure), on the meteor exceeds its characteristic compressive strength (e.g., Melosh, 1989). Once an object has broken up, it must be determined what effect breakup has on the impact process. Does the meteor still impact as essentially a single coherent mass and thereby form a crater as if intact, or do its fragments spread out before impact to form an irregularly shaped structure, a cluster of many small craters, or even no crater at all? The answer to this question depends on many factors, including meteor size, density, and the altitude and velocity at which breakup occurs.

Despite these effects, however, Mars's atmosphere has often been neglected in deriving martian isochrons from lunar ones. Common justification for neglecting Mars's atmosphere is its low density and the apparent failure to detect any atmosphere-related "turndowns" in observed size-frequency plots of martian populations for diameters larger than about 16 m (Hartmann, 1999). However, below some diameter value the presence of an atmosphere must begin to strongly influence cratering rates. Vasavada et al. (1993) concluded that Mars's present atmosphere is sufficiently dense (~6.1 mbar average surface pressure) to completely ablate all stony, icy and carbonaceous chondrite meteoroids up to masses of ~10 kg. This result implies that there must be a turndown at meter-scale diameters, since 10 kg impactors are capable of producing meter-scale

craters. More recently, Hörz et al. (1999) concluded that the smallest martian craters should be sub-meter in size, while Popova (2003) found that craters down to 0.3 m should be formed by iron impactors, under current atmospheric conditions. Presumably the long-sought martian atmospheric turndown begins somewhere in this range.

Exactly how Mars's atmosphere has influenced cratering rates depends on its history. Several researchers (e.g., Ward, 1974; Bills, 1990) have found that radical changes in Mars's obliquity may cause its surface pressure to vary between essentially zero and 30-40 mbar (James et al., 1992) or higher on timescales of 10^5-10^6 years, though recent work has cast some doubt on whether Mars has enough CO_2 stored in its ice caps to support such large pressures (Titus et al., 2003; Byrne and Ingersoll, 2003). Other recent work suggests that Mars may presently be emerging from an 'ice age', which, on Mars, is a period of high obliquity (Head et al., 2003; Feldman et al., 2003). Martian ice ages are actually times of relative warmth, rather than cold, at the poles, which appears to cause migration of water ice from poles to mid-latitudes, and CO_2 from polar caps and regolith to atmosphere. Thus martian ice ages are periods of increased atmospheric pressure and density. Though we currently have no physical evidence that Mars has experienced any recent, large changes in atmospheric pressure, the cratering record may provide an opportunity to detect such variations, since their effects may be observable in populations of small impact craters resolvable with current Mars Orbiter Camera – Narrow Angle (MOC-NA) imagery or with upcoming capabilities of even higher spatial resolution, such as the High Resolution Imaging Science Experiment (HiRISE) instrument scheduled for launch in 2005 (McEwen et al., 2002).

Populations of small craters are especially well suited for studying such short timescale changes because impact rates are much higher for small objects than for larger ones; populations of small craters, therefore, respond much faster to changes in impact rates than do populations of larger ones. Unfortunately, such features are probably rapidly erased on Mars and are difficult to detect from orbit or the surface (Hörz et al., 1999).

Martian topographical relief also results in pressure variations from place to place on the surface that currently span an order of magnitude from ~10 mbar in Hellas to less

than 1 mbar on Olympus Mons (Fig. 3.2). Vast regions of Mars lie under surface pressures of 4-5 mbar (southern highlands) and 7-8 mbar (northern lowland plains). Since the northern plains lie under a significantly denser, deeper atmosphere than the southern highlands, rates of small crater formation there may be considerably lower.

In this Chapter I report the results of my investigation into how the presence of the martian atmosphere, and its variations, affect impact cratering rates at small diameters (2-250 m), and isochrons and surface ages derived therefrom, and how atmospheric variations may be expressed in the small cratering record. In the process, many estimates and assumptions must be made; however, wherever this is necessary my approximations err on the conservative side, so far as possible, thus tending to underestimate the effects of Mars's atmosphere on impact cratering, rather than exaggerate them. Therefore, my results should tend to represent lower bounds on the effects of the martian atmosphere on cratering rates, and actual effects may well be larger.

3.2 METHODS

To investigate the effects of Mars's atmosphere on its cratering rates at small diameters, I constructed a computer model which simulates atmospheric passage and surface impact of large effective populations of meteoroids capable of producing ~2.0-250.0 m craters. The program numerically integrates the differential equations of motion of meteor flight in an atmosphere (Eq. 3.2 - 3.4), then calculates crater size from impact angle and kinetic energy.

3.2.1 Simulating large numbers of impactors

The mass range 10^{-1} kg to 10^{7} kg includes all masses commonly able to produce 2.0-250.0 m craters on Mars. Objects smaller than 10^{-1} kg would have to hit the surface vertically at velocities well above 60 km s^{-1} to produce 2 m size craters, while ones larger than 10^{7} kg produce craters larger than 300 m unless their impact velocities are less than Mars's escape velocity (~5 km s^{-1}), even if they strike at very shallow impact angles (see Eq. 3.14, below). The brute-force method of simply simulating the atmospheric passage and impact of very large numbers of meteors with masses in this range, and with an

appropriate mass-frequency distribution, would produce a crater population which reflects the impact of the given projectile population, plus the influence of whatever atmosphere it encountered (e.g., Vasavada et al., 1993). However, using this method over the required large range of masses would entail moving billions of meteors through the simulation in order to include statistically meaningful numbers of the largest objects. For this range of projectile masses, I rely on a mass-frequency distribution that reproduces the slope of the "Steep branch" of the Hartmann isochrons,

$$N(m) = \alpha m^{-1.27}, \tag{3.5}$$

where N is the number of objects in a population more massive than m, and α is a constant. Therefore, in order to include just 1000 objects greater than 10^6 kg in mass in my population, I would have to simulate more than 500 billion objects more massive than 0.1 kg, which would be prohibitively time-consuming.

My solution to this problem is to simulate a number, k, of sub-populations of impactors, $P(m_j)$, each composed of l impactors of fixed mass m_j (where j = 1, 2, 3 ..., k), but otherwise randomly generated as described below. The number of sub-populations must be chosen to cover the mass range of interest in sufficient density to avoid artifacts due to the discrete nature of the meteor masses, and the number of impactors per sub-population must be large enough to adequately represent the distributions of the other variables (meteoroid type, strength, entry velocity and entry angle) in each sub-population. I found that seventeen, 2000-meteoroid sub-populations (ie. k = 17, l = 2000) at mass-values spaced by powers of ½ (i. e. $m_j = 10^{(j-3)/2}$ kg) and covering the range $10^{-1}\text{kg} \le m \le 10^{7}\text{kg}$ satisfied these criteria for my purposes. The m_j were spaced apart by powers of ½ rather than 1 to minimize artifacts in the final crater population caused by the discretization of meteoroid masses represented by j.

Each meteoroid sub-population, $P(m_j)$ was then run through the entry/impact simulation to produce a corresponding crater sub-population, $n_j(D)$, where $n_j(D)$ is the number of craters larger than D produced by the l objects of mass m_j. The final, total

impact crater population, $n(D)$, is then constructed by adding up a weighted sum of the crater sub-populations,

$$n(D) = w_1 n_1(D) + w_2 n_2(D) + w_3 n_3(D) + \ldots\ldots + w_n n_n(D). \quad (3.6)$$

The weight factors, w_j, represent the relative importance of each meteoroid sub-population, $P(m_j)$, according to Eq. 3.5, and therefore the relative importance of its corresponding crater sub-population, $n_j(D)$, relative to an arbitrarily selected reference sub-population, $P(m_{ref})$, is

$$N_{bin}(m_j) = w_j \cdot N_{bin}(m_{ref}),$$

where $N_{bin}(m)$ stands for the binned, or incremental, representation of the mass-frequency distribution and where the jth bin has boundaries at $m_{j-½}$ and $m_{j+½}$. The weight factors are then

$$w_j = \frac{N_{bin}(m_j)}{N_{bin}(m_{ref})} = \frac{N(m_{j-½}) - N(m_{j+½})}{N(m_{ref-½}) - N(m_{ref+½})}. \quad (3.7)$$

Using Eq. 3.5, this can be rewritten in terms of the masses

$$w_j = \frac{m_{j-½}^{-1.27} - m_{j+½}^{-1.27}}{m_{ref-½}^{-1.27} - m_{ref+½}^{-1.27}}. \quad (3.8)$$

To implement this procedure I computed the weight factor for each crater sub-population from Eq. 3.8, then assembled the total crater distribution from the sub-populations by summing the sub-populations (Eq. 3.6). This procedure resulted in a final crater population function which reflects several orders of magnitude more impact events than were actually simulated by the program. For example, using the values for k, l, and m_j given above, and $m_{ref} = 10^4$ kg, $n(D)$ represents the crater population produced by entry into Mars's atmosphere of over 5 billion meteoroids larger than 0.1 kg, while only 34,000 are actually simulated.

3.2.2 Constructing meteoroid populations and sub-populations

Separate populations of meteoroids were constructed for each of four types: icy, carbonaceous chondrite, stone, and iron. For each of the four types, subpopulations of 2000 objects each were compiled at each of 17 mass-values (as discussed above); each meteoroid was assigned entry velocity, entry angle and crushing strength selected randomly from a probablity distribution appropriate to its type, to each of the 34,000 objects required of each type. In addition, densities and heats of ablation were assigned based on type (see Table 3.1).

Entry angles, θ_o, measured from the horizontal, were generated according to the usual $\sin\theta\cos\theta$ incremental probability distribution (e.g., Gilbert, 1893) for all impactors. This function has a maximum at 45° and drops off to zero at 0° and 90°. Velocities and crushing strengths obviously depend on object type, and were assigned as described below.

The first step in generating entry velocities was calculation of minimum and maximum possible values, $v_{\min}$ and $v_{\max}$, for each type of object. Energy conservation was used to calculate the velocities of Mars-crossing asteroids, short-period comets and long-period comets, assuming aphelia in their source regions. The limiting Mars entry velocities, for prograde orbits, are then given by

$$v_{\min} = \left[\left(v_{obj} - v_{Mars}\right)^2 + v_{esc}{}^2\right]^{1/2} \tag{3.9a}$$

for orbits with perihelia at Mars' orbit, and

$$v_{\max} = \left(v_{obj}{}^2 + v_{Mars}{}^2\right)^{1/2} + v_{esc} \tag{3.9b}$$

for ones with perihelia at the Sun. Here v_{Mars} is Mars's orbital velocity, v_{obj} is the velocity of the Mars-crossing object at Mars's orbital distance, and v_{esc} is Mars's escape velocity.

For cometary-type objects, velocities were then obtained from a gaussian (normal) probability function centered at the average value of $v_{\min}$ and $v_{\max}$ (v_o) and which falls off such that $v_{\min}$ and $v_{\max}$ lie at v_o-3σ and v_o+3σ respectively. For asteroidal type objects, a half-gaussian with peak at $v_{\min}$, and falling off such that $v_{\max} = v_{\min}$+3σ,

was chosen for the probability function. The gaussian and half-gaussian were chosen to approximate the shape of data found in Chyba (1991) for impact velocity probabilities on Earth. Object strengths, S, were generated from gaussians centered at the values given in Table 3.1, with a σ given by 3σ = S/2.

Assigning appropriate values for meteor crushing strength is problematic, as they are poorly known, but strongly influence breakup altitudes. The only samples available for direct testing are meteorites that have survived passage through Earth's atmosphere and are therefore strongly selected for high density, heat of ablation and strength, and obviously do not include any icy objects. Indirect methods that have been used to estimate strengths include observations of comets undergoing tidal failure (e.g., Sekanina, 1982; 1993) and breakups of terrestrial fireballs (e.g., Brown et al., 2002), however such methods are quite complex, and available results are very limited in number and subject to large uncertainties. Further complicating matters, meteoroid strengths are almost certainly dependent upon mass, with larger ones weaker on average than smaller ones (Weibull, 1939), so that the small objects studied in this work are probably considerably stronger than the ones observed in tidal failure studies, for example. In view of these facts, and in keeping with my conservative philosophy, in this study I use values for the strengths of my meteoroids that fall toward the high end of estimates found in the literature (see Table 3.1).

3.2.3 Modelling the atmosphere

Mars's atmosphere is represented by a simple exponential,

$$P_{atm}(z) = P_0 e^{-z/H},$$

where $P_{atm}(z)$ is the atmospheric pressure, P_0 is surface pressure, z is altitude, and scale height, H, is assumed constant and equal to 10.9 km. This assumption is equivalent to supposing an isothermal atmosphere, in which case the above can also be written in terms of atmospheric densities,

$$\rho_{atm}(z) = \rho_0 e^{-z/H} \tag{3.10}$$

assuming that Mars's atmosphere can be treated as an ideal gas. Here $\rho_{atm}(z)$ is the atmospheric density and ρ_0 its value at the surface.

3.2.4 Effects of atmospheric passage

As a meteor passes through an atmosphere it loses mass to ablation, velocity to drag, and its trajectory angle, which has initial value θ_0 with respect to the horizontal, steepens toward 90°. Occasionally ablation will strip off enough mass to reduce a meteor to less than 0.05 kg, which is insufficient to form a crater larger than 2 m except in extraordinary cases, or drag may reduce its velocity to below that required to generate shock waves of sufficient magnitude to crush, and excavate a crater in a silicate target. For purposes of this study, an impact is considered crater-forming only if its impact velocity is greater than 500 m s^{-1}. If the mass or velocity fall below these figures during entry, the meteor is considered to have "burned up" or "soft landed", respectively, in which case the integration is halted, no crater is formed, and the program moves on to the next impactor. Otherwise integration continues until the object either breaks up or impacts the surface.

Atmospheric breakup occurs if aerodynamic stresses on the object exceed some limiting strength, though the fragments may still impact the surface clustered tightly enough to form an impact crater. In my simulation, a meteor is deemed to "break up" if the dynamic (stagnation) pressure, $\frac{1}{2}\rho_{atm}v^2$, exceeds its characteristic crush strength. The same forces that cause the object to break up will flatten it and accelerate its fragments transversely to the original flight path, imparting transverse velocities up to about the order of

$$v_{trans} = \left(\rho_{atm,b} / \rho \right)^{1/2} \cdot v_b$$

(Passey and Melosh, 1980; Melosh, 1989; Hills and Goda, 1993), where the subscript b denotes values at breakup. The resultant cross-range scatter of the fragments is given approximately by

$$S_{cross} = \frac{2z_b}{\sin\theta_b}\left(\rho_{atm,b}/\rho\right)^{1/2}$$

assuming the fragments move in straight lines at constant speeds after breakup. The down-range scatter, S_{down}, is greater by an additional factor of $1/\sin\theta_b$

$$S_{down} = \frac{2z_b}{\sin^2\theta_b}\left(\rho_{atm,b}/\rho\right)^{1/2}. \tag{3.11}$$

Note that several important phenomena are ignored in the derivation of Eq. 3.11, including increased aerobraking (see Eq. 3.1) and ablation (see Eq. 3.3) after break up due to the larger effective cross-sectional area of the flattening impactor, differential aerobraking (see Eq. 3.2) and ablation (see Eq. 3.4) of fragments of differing masses, and potential secondary breakup of meteor fragments. Aerodynamic side forces are also neglected after the brief period of interaction between fragments, as Passey and Melosh (1980) have shown that these are probably quite small. However, the omission of these effects is in line with my stated intent to err on the conservative side in my assumptions, since they would all have a tendency to increase the effectiveness of atmospheric filtering of the impactor population if they were included in the simulation. In any case, these effects cannot be accounted for without introducing some compromising assumptions about the poorly constrained details of breakup and the dynamics of all the various fragments after breakup.

Next, criteria are needed to determine the significance of break up in terms of crater formation. To simplify the discussion that follows, I introduce the 'scatter parameter', K,

$$K \equiv S_{down}/D$$

where D is the diameter of a crater that would be formed, if the impactor struck the surface intact. An object which breaks up but fails to significantly scatter before impact (i. e. $K = 0$) will produce a crater that is indistinguishable from one generated by an intact projectile. At the other extreme, if the scatter is large ($K \to \infty$), the meteor fragments will

impact as essentially independent objects, forming a field of craters. Between these extremes is a continuum of craterforms, one grading into the next (Schultz and Gault, 1985). The question becomes: for purposes of crater-counting, at what scatter parameter does the resultant impact structure no longer resemble a single crater?

Experimental results obtained by Schultz and Gault (1985) indicate that the structure formed by a scatter field of impacts which has $K \approx 1/3$ is still surrounded by a circular raised rim, and thus still resembles a single crater for purposes of crater counting. Its interior is not the usual bowl shape of a simple crater, but a chaotic terrain containing sub-structures associated with the impacts of individual fragments, and with a rim-to-rim diameter of approximately $2/3 D$. With these results in mind, I require that $K \leq 1/3$ for a disrupted object to produce a single recognizable craterform, and the diameter of the resultant crater is $D - S_{down}$; if $K > 1/3$ no recognizable, single crater is formed. I do not include the possibility of multiple crater formation in this analysis.

It should be mentioned at this point, that more advanced methods do exist for simulating the motions of post-breakup meteor fragments, including the "pancake" model (e.g., Zahnle, 1992; Chyba et al., 1993) and the "separate fragments" model (Shuvalov et al., 2000; Artemieva and Shuvalov, 2001; Artemieva and Bland, 2003). However, these methods are very computationally intensive and are well beyond the needs of this study, in view of its objectives, as I expect that such events (breakup, followed by dispersion and multiple, independent impacts) are quite rare on Mars. Both Passey and Melosh (1980) and Artemieva and Shuvalov (1996) indicate that the optimum breakup altitude for maximum spreading of fragments is two atmospheric scale heights, or 20-25 km for Mars, regardless of entry angle. My results indicate that the vast majority of asteroidal-type objects that break up, do so well below 20 km, even for the densest (60 mbar) atmosphere studied. The resultant fragments simply do not have time to separate sufficiently to form individual craters.

As for the cometary-type, quite a few icy objects were found to break up in the 20-25 km range, and thus may spread out enough to form crater clusters if their trajectory angle is low enough. However these objects still have alot of Mars's atmosphere to

traverse, and their low density, low heat of ablation, and fragmental state make them especially vulnerable to further ablation and deceleration; in addition there would be the potential for further fragmentation. As a result, very few even of these objects will create crater clusters under atmospheres I have studied. Results found in Aremieva and Shuvalov (1996), Artemieva and Bland (2003), and Popova et al. (2003) all tend to support this view.

For these reasons I neglect the small fraction of icy and carbonaceous objects that may manage to form multiple craters, and consider them to have fragmented catastrophically.

3.2.5 Atmospheric flight simulation

In the atmospheric flight simulation, individual meteoroids, assumed spherical, are started at an altitude of eight martian atmospheric scale heights (~87 km), where the atmospheric pressure is 0.03% of its surface value (0.002 mbar when the surface pressure is 6.1 mbar). The equations governing their passage through the atmosphere are

$$dv/dt = -C_D \frac{\rho_{atm} A}{2m} \cdot v^2 + g_0 \sin\theta, \tag{3.12a}$$

$$dm/dt = -C_H \frac{\rho_{atm} A}{2Q} \cdot v^3, \tag{3.12b}$$

$$d\theta/dt = \frac{g_0 \cos\theta}{v}, \tag{3.12c}$$

(e.g., Baldwin and Schaeffer, 1971) where g_0 is Mars's surface gravity, and C_D and C_H are the drag and heat transfer coefficients, respectively. These equations are integrated using a 4th-order Runge-Kutta method (see the Appendix to this thesis), subject to the criteria for burnup, breakup and soft landing given above. Several important assumptions are implicit in Eqs. 3.12:

(1) Flat Mars approximation. Mars's curvature is neglected, so Eq. 3.12c does not have a term to account for variations in θ due to horizonal motion. Note that this assumption precludes the possibility of "skip-out" of low-incidence-angle meteors.

(2) Constant gravitational acceleration. A consequence of assumption (1) is that the direction of Mars's gravity is constant. Since the variation of its magnitude between Mars's surface and the starting altitude of $8H$ is quite small (~5%), gravity is simply considered to be constant in magnitude and direction.

(3) No aerodynamic side forces. Passey and Melosh (1980) have demonstrated that these are probably small, even for meteors in Earth's much denser atmosphere, therefore they are neglected for Mars and no side force term appears in Eq. 3.12c.

The drag coefficient in Eq. 3.12a is considered constant in this work, however the heat transfer coefficient varies with velocity. Experiments by Masson et al. (1961) with rough spheres in hypersonic gas flows indicate that C_D varies from about 0.92 in the continuum flow regime, to about 2.0 in the free molecular regime; I chose the commonly used intermediate value of 1.0 (e.g., Passey and Melosh, 1980; Chyba et al., 1990; Zahnle, 1992; Hills and Goda, 1993) for simplicity. It is worth noting at this point that an ambiguity exists in the literature concerning the definition of C_D. In some other works the factor of two in the denominator of Eq. 3.12a is absorbed into the drag coefficient (e.g., Passey and Melosh, 1980; Hills and Goda, 1993), which makes the value of the drag coefficient that appears in these works equal to one half that used here.

Results of numerical studies by Biberman et al. (1980) show that the heat transfer coefficient depends strongly on v and ρ_{atm}. For atmospheric densities like those encountered in this investigation C_H is approximately 0.1 when the impactor's velocity is 15 km s^{-1} or greater, dropping sharply to less than 0.01 for velocities less than 10 km s^{-1}. Since this large change in C_H occurs at velocities quite typical of the objects I am

simulating, I employed a three-part heat transfer coefficient, where the segment between $v = 10$ km s^{-1} and $v = 15$ km s^{-1} is a simple linear interpolation:

$$\begin{aligned} C_H &= 0.1 && v > 15 \text{ km s}^{-1}, \\ C_H &= 1.8\times10^{-2}\, v - 0.17 && 10 \text{ km s}^{-1} < v < 15 \text{ km s}^{-1}, \\ C_H &= 0.01 && v < 10 \text{ km s}^{-1}. \end{aligned}$$

3.2.6 Crater diameter from impact energy

Once a meteor successfully negotiates Mars's atmosphere and strikes the surface, the rim-to-rim diameter of the crater must be calculated from the impact conditions. For simplicity, a form of the scaling law

$$D = D_0 \left(KE / KE_0 \right)^{1/3} \tag{3.13}$$

(Glasstone, 1957; Melosh, 1989) was adopted, where KE is the impact kinetic energy and the subscript 0 denotes some reference values. Experimental results on oblique impact into a non-cohesive target (Gault and Wedekind, 1978) indicate that D also goes as $(\sin\theta_f)^{1/3}$. Incorporating this into Eq. 3.13, we have

$$D = D_0 \left(\frac{KE \cdot \sin\theta_f}{KE_0} \right)^{1/3}. \tag{3.14}$$

In order to use this expression the diameter, D_0, of the crater produced by an impact of some known reference impact energy, KE_0, is required. To find such a reference pair, crater diameters were calculated using the "pi-scaling" method (Holsapple and Schmidt, 1982; Melosh, 1989) for each of twelve imaginary impacts, each with the same kinetic energy, $KE_0 = 10^{11}$ J and vertical incidence angle. Mass, velocity and density were varied (subject to the constant energy constraint) to cover the ranges of interest for each of these variables, and crater diameters calculated. The results were averaged and a value of 22.5 m ($\sigma = 3.0$ m) was obtained for D_0, the average size of crater produced by a 10^{11} J impact.

3.2.7 Assembling the crater population

All of the impactors were processed for atmospheric passage and surface impact, generating four populations of impact craters, one for each impactor type. Each crater population was then binned according to procedures defined by the Crater Analysis Techniques Working Group (1979), so that it is represented by an incremental diameter-frequency distribution. The total impact crater diameter-frequency distribution, $N(D)$, was then formed by adding up a linear combination of these distributions

$$N(D) = A_{icy} \cdot N_{icy}(D) + A_{c.c.} \cdot N_{c.c.}(D) + A_{stone} \cdot N_{stone}(D) + A_{iron} \cdot N_{iron}(D),$$

where the weight coefficients, A_{type}, are the mass fractions of each type of impactor. This method has the advantage that $N(D)$ can be constructed for any composition of impactor population, simply by changing the weight coefficients. In this study, weight coefficients for the asteroidal (carbonaceous chondrite, stony, and iron) part of the impactor population are based on the taxonomy of their parent bodies, the asteroids, (Tholen, 1989) with an added cometary component. Of the asteroidals types, 75% are carbonaceous chondrite, 16% are stony, and 9% irons.

3.2.8 The question of small cometary impactors

Very little evidence, one way or the other, exists concerning a putative inner solar system population of small cometary impactors. To date, the Solar and Heliospheric Observatory (SOHO) spacecraft has detected over 850 small sungrazing comets and comet fragments (see http://ares.nrl.navy.mil/sungrazer/ for latest count) with aphelia in the Kuiper Belt. The fragments have estimated diameters down to tens of meters or less (e.g., Raymond et al., 1998; Uzzo et al., 2001), which puts them in the mid- to upper end of my mass range of interest. The current discovery rate suggests that there are at least tens of thousands of these comets; many more may remain undetected because they are too small, are not in sungrazing orbits, or are too depleted in volatiles.

Other studies of martian meteor entry and impact do not consider the possibility of small, cometary impactors (e.g., Dycus, 1969; Artemieva and Bland, 2003), even ones that acknowledge the likelyhood of much thinner atmospheres in Mars's past (e.g., Vasavada et al., 1993; Hörz, et al., 1999). Others neglect them by assuming that there are

very few (Neukum et al., 2001), or that they are too fast, friable and weak to survive the atmosphere (e.g., Davis, 1993). Popova, et al. (2003) is a notable exception to this rule. However, studies by Oberst and Nakamura (1987, 1991) provide evidence that a population of small cometary impactors capable of planetary impact does indeed exist in the inner solar system. The question becomes, how significant a population? In the absence of good quantitative evidence, I take advantage of the adjustable nature of my method to consider the cratering effects of small impactor populations containing several different percentages of icy objects, by mass.

Using procedures described above, I simulated the atmospheric passage and surface impact of large populations of four types of meteoroids for several different atmospheric surface pressures in the range 0-60 mbar, in order to investigate the effects of Mars's atmosphere and its possible variations on martian impact cratering rates. Cases included the 0 mbar 'airless Mars' and 6 mbar 'current average' conditions; the 0 mbar results serve as an atmosphereless reference case with which to compare other cases.

Crater populations for each impactor type (carbonaceous chondrite, stony, iron, and icy) and six atmospheric densities (0, 2, 6, 20, 40, and 60 mbar) were plotted on incremental log-log axes. Outcomes (burnup, fragmentation, soft-landing, or crater-forming impact) were recorded and sorted, and stacked histograms of the results were prepared for each type of impactor, and four atmospheric densities (2, 6, 20, 60 mbar). Finally the data for the four types of objects was combined to form total crater populations corresponding to four different proportions (0%, 5%, 10%, 20%) of icy, cometary impactors, and the resulting SFDs were plotted.

3.3 RESULTS AND DISCUSSION

3.3.1 Asteroidal impactors

Figures 3.3a-c display the cratering effects of passing separate populations of the three asteroidal types of impactors through several potential martian atmospheres. A 'turndown' occurs in the size-frequency distribution (SFD) of carbonaceous chondrite impactors (Fig. 3.3a) for each atmosphere, increasing in magnitude with atmospheric density. At

large diameters (D > 100 m, m > 10^5 kg) the SFDs generally approach the 0 mbar SFD, though only those due to the low density atmospheres (2 mbar and 6 mbar) actually converge with it. Those representing high density atmospheres (20, 40 and 60 mbar) depart from it significantly, even at diameters approaching 200 m, and represent cratering deficits of an order of magnitude or more at diameters less than 25 m. In addition, at small diameters (D < ~10 m) the turndowns due to high density atmospheres also have more pronounced downward curvatures.

The SFDs for the other asteroid types are qualitatively similar (Figs. 3.3b,c), though the departures of their SFDs from the 0 mbar line decrease slightly with object type, from carbonaceous chondrite to stone to iron, due to higher heats of ablation and densities. However, one notable difference is that the SFDs for stony and iron impactors converge more strongly to the 0 mbar line at large diameters than do those of the carbonaceous chondrites, especially under the higher density (20-60 mbar) atmospheres, an effect which is discussed below. It is not generally possible to define a starting diameter for the observed turndowns, since they are not sudden changes in slope, but gradual increases in downward curvature toward smaller crater diameters; in fact, the broadness of the turndowns caused by low density atmospheres, including that due to the 6 mbar 'current martian average' atmosphere, may make them quite difficult to detect in real cratering data.

Figure 3.3d shows the results of combining the separate SFDs into one crater population consisting of 75% carbonaceous chondrite, 16% stone, and 9% iron impactors, reflecting a combination of the effects described above, including the significant reduction in cratering at large diameters (D > 100 m) for high density atmospheres seen in Fig. 3.3a. This feature remains because of the large proportion of carbonaceous chondrites in the impactor population.

There is no sign of an 'atmospheric cutoff', below which no craters are formed, for atmospheres up to 60 mbar of surface pressure. This is consistent with results found in Hörz et al. (1999), who have reported evidence for martian craters less than 1 m in diameter, Popova et al. (2003), who found that the smallest iron impactors should

produce craters down to D = 0.3 m, and Hörz et al. (2004) who concluded that sub-meter cratering should be common on Mars, all under present martian conditions.

These results indicate that the meter-scale cratering record may be a good place to look for evidence of martian climate change. High production rates, combined with strong atmospheric influences on these rates, means that populations of small craters respond rapidly and strongly to excursions in atmospheric density associated with climate change, and ultimately obliquity variation. Since small craters are also removed relatively quickly, the record they preserve would probably be that of the most recent such variation. Detection of a sharp turndown in meter-scale cratering could provide physical evidence of a recent period of denser atmosphere; the absence of such a feature may indicate a recent period of near lunar-like conditions. These results emphasize the desirability of a higher resolution imager, such as the High Resolution Imaging Science Experiment (HiRISE), to examine the martian cratering record at meter scales and below.

It is also possible using Figs. 3.2 and 3.3d to estimate the differences in cratering that can be attributed to altitude differences from place to place. Taking as an example, the southern highlands vs. the northern plains, which differ in average altitude by ~6 km and in average pressure by ~3 mbar, Fig. 3.3d shows that, all else being equal, one may expect approximately twice as many 2.7-3.9 m craters in the south as in the north, due to the altitude difference alone. Thus these results predict an important altitude dependence on local cratering records on Mars that has nothing to do with relative age.

3.3.2 Asteroidal impactors - effects of low density atmospheres

Both turndowns produced by the low density atmospheres (2 mbar, 6 mbar) are quite small (Fig. 3.3d). Reductions in cratering are less than an order of magnitude (except, at very small diameters, in the 6 mbar case), the SFDs are nearly parallel to the 0 mbar SFD, and they merge into the 0 mbar line at about D = 100 m. The reductions in cratering are due almost entirely to the effects of ablation and drag on the impactors; very little fragmentation of asteroidal type objects occurred in any of these low density atmospheres (Figs. 3.4). The vast majority of the small asteroidal objects (m < ~3 kg; D_{0mB} < ~3.0 m) burned up completely or are so ablated and decelerated that they form

only very small (sub- 2 m) craters, though the 6 mbar atmosphere did aerobrake a handful of the smallest (m < ~ 1 kg; D_{0mB} < ~2 m) to soft landings on the surface.

Larger objects (~3 kg < m < ~3×10^5 kg; ~3 m < D_{0mB} < ~100 m) survived to impact crater the surface, but many were so reduced in mass and velocity that their resulting craters were much smaller than the ones they formed in the airless-Mars case, so they ended up in smaller diameter bins; the mass-frequency law (Eq. 3.5) guarantees that this 'bin hopping' effect results in a net decrease in cratering in each bin. Bin hopping is responsible for essentially all of the observed reduction in the cratering SFD of asteroidals at diameters greater than about 4 m, under less than 6 mbar of atmosphere. This effect diminishes to zero at about D = 100 m, and impact cratering rates are largely unaffected beyond about D = 50 m.

3.3.3 Asteroidal impactors - effects of high density atmospheres

The results of passing my populations of asteroidal impactors through high density (20, 40, 60 mbar) atmospheres are presented in Figs. 3.5. Three effects are immediately apparent: (1) bin hopping is greatly increased over the low density atmospheres, (2) fragmentation becomes a major outcome among the carbonaceous chondrites, and (3) the number of objects that are decelerated into soft landing on the surface increases very dramatically.

Bin hopping alone accounts for essentially all of the reduction in cratering by stony and iron objects larger than m = ~1000 kg (D_{0mB} = ~20 m) and for much of it by similarly sized carbonaceous chondrites, under all of the atmospheres investigated. For the stones and irons, bin hopping due to ablation/deceleration is the dominant filtering effect all the way down to m = ~100 kg (D_{0mB} = ~8 m). These results clearly demonstrate how an atmosphere can sharply reduce impact cratering rates, without actually destroying any impactors. The general increase in crater deficits with increasing atmospheric density is due primarily to this process.

In addition to bin hopping, Fig. 3.5a shows that the 20 mbar atmosphere begins to break up significant numbers of carbonaceous chondrites in the 10^4 kg - 10^7 kg range (D_{0mB} > ~40 m), as maximum dynamic pressures become comparable to the strengths of

these objects. The effect grows with increasing atmospheric density and results in substantial cratering reductions under 40 mbar and 60 mbar atmospheres at diameters larger than 40 m. This effectively prevents the 20, 40 and 60 mbar SFDs for carbonaceous chondrites-only (Fig. 3.3a), and for the asteroidal population as a whole (Fig. 3.3d), from converging with the 0 mbar SFD, resulting in cratering deficits even at large (100 – 200 m) diameters.

It should be noted that the details of this phenomenon depend on the strengths of the carbonaceous chondrite objects. If they are higher than my estimates, this effect would be weaker, though my strength estimates tend toward the high end of those published in the literature, as mentioned above.

Probably the most striking difference between the results for low and high density atmospheres is the major increase in the proportions of all three types of objects that were aerobraked into soft landings (compare, for example, Figs. 3.4d and 3.5c). No asteroidal objects were found to impact the surface at less than 500 m s^{-1} under the 2 mbar atmosphere (Figs. 3.4a,c,e) and only a small number did so under the 6 mbar atmosphere (Figs. 3.4b,d,f). But about 50% of small (m < 3 kg; D_{0mB} < 2.6 m) carbonaceous and stony meteors, a few carbonaceous chondrites as large as 100 kg, and even some small (m < 1.0 kg; D_{0mB} < 2 m) iron objects, soft landed under the 20 mbar atmosphere (Figs. 3.5a,c,e). The effects of the 60 mbar atmosphere were greater still (Figs. 3.5b,d,f): more than half of the stone and carbonaceous chondrite meteors less than ~30 kg in mass (D_{0mB} < ~6 m), and many irons up to ~10 kg, soft landed on the surface. This large difference in meteorite production between low density and high density atmospheres indicates that the presence of large numbers of asteroidal-type meteorites on the surface of Mars would provide evidence of previous denser martian atmospheres, even if intervening atmospheric lows have reworked the cratering record.

3.3.4 Icy impactors

Icy impactors are dealt with here, separately, because of their many differences from the asteroidal population and because of the great uncertainty concerning their contribution to the total martian impactor population, as previously discussed.

A major difference between impact cratering by a population of icy, cometary bodies, and one made up of asteroidals (both characterized by the same mass-frequency distribution) is that, in the absence of an atmosphere, the cometary population will produce cratering rates up to an order of magnitude greater. This high cratering efficiency is not due to the presence of ten times more comets than asteroids, but because the comets encounter Mars at much higher velocities and therefore excavate larger craters than asteroids of the same mass. This 'velocity effect' is illustrated in Fig. 3.6, which compares the crater population produced by two thousand, 1000 kg icy impactors to that formed by a like number of 1000 kg stones. It also explains why the 0 mbar SFD for the cometary population (Fig. 3.7) lies a full order of magnitude higher than for any of the asteroidal impactor populations (Figs. 3.3a-c). It is worth noting that the Moon is also subject to this phenomenon.

Figure 3.7 shows that even the 2 mbar atmosphere devastates the icy impactor population and Fig. 3.8a shows how. Almost no icy objects smaller than ~300 kg (D_{0mB} = ~28 m) impacted the surface, and the very few that did are massively ablated and slowed; practically all the rest burned up. Cratering at diameters less than ~30 m was extremely rare, and was all caused by impacts of icy objects which formed much larger craters in the 0 mbar, airless case. Many larger objects (m > ~1000 kg; D_{0mB} > ~40 m) survived ablation only long enough for them to fragment rather than burn up, so even at D = 250 m cratering by cometaries was cut by more than 75%, even by only 2 mbar of atmosphere.

The 6 mbar atmosphere prevented almost all cratering by icy objects in my diameter range of interest (Fig. 3.8b); the results are not plotted on Fig. 3.7 because the few cratering events that do occur are statistically insignificant and so cannot be represented as an SFD. Needless to say, cratering by icy objects through the higher density atmospheres is virtually non-existent in my range of interest, so there are no SFDs or histogram plots for these cases.

Since the cometary part of the impactor population is quite efficient at cratering an airless planetary body, but is nearly completely wiped out by almost any atmosphere, the effect of adding a cometary part to to the asteroidal population from which Fig. 3.3d

is derived is basically to shift the 2-60 mbar SFDs downward on the graph relative to the 0 mbar SFD. Fig. 3.9, together with Fig. 3.3d, display cratering results for impactor populations containing four different proportions of cometary objects (in addition to the usual proportions of the asteroidal types). Of particular interest is the cratering deficit at large diameters ($50 < D < 200$ m), which grows with increasing percentage of icy bodies, for the current martian atmosphere (see Figs. 3.9). If the inner solar-system impactor population contains significant numbers of cometary bodies, this across-the-board cratering deficit may present a problem for surface dating based on crater counts since, uncorrected, it would tend to cause underestimation of surface ages.

3.4 CONCLUSIONS

1) In the diameter range 2 - 250 m, low density (2 mbar, 6 mbar) martian atmospheres reduce impact cratering by asteroidal-type impactors primarily via the effect of 'bin hopping'. Only some of the smallest ($m < \sim 3$ kg; $D_{0mB} = < \sim 3$ m) of these objects completely burn up before impact; a very small number of these are decelerated to soft landings on the surface instead.

2) Higher density (20, 40, 60 mbar) atmospheres further reduce impact cratering due to enhanced bin hopping, but their effects differ in two other important ways: (i) Peak dynamic pressures encountered by entering objects begin to exceed the strengths of many carbonaceous chondrite projectiles, causing numbers of them to fragment in the atmosphere. Still no significant numbers of stones or irons break up. (ii) Instead of burning up, as they do in the low density atmospheres, large numbers of small asteroidals (mainly less than 10 kg in mass) are aerobraked to soft landings; thus the presence of large numbers of meteorites on Mars could constitute evidence of past atmospheres denser than today's.

3) Atmospheric filtering of the impactor population results in increasing turndowns in the cratering SFDs produced by a composite population of asteroids composed of 75% carbonaceous chondrites, 16% stones and 9% irons, with increasing atmospheric density. These diminish at larger diameters, but only converge with the 0 mbar reference line for

the 2 mbar and 6 mbar atmosphere cases. Thus, the high density atmospheres produce cratering deficits even at diameters above 100 m; these are due primarily to fragmentations of carbonaceous chondrite objects in atmospheres denser than today's.

4) Turndowns produced by the low density atmospheres have little curvature and are nearly parallel to isochrons; this could lead to underestimation of crater-count-derived surface ages, if SFDs are interpreted as unfiltered production functions.

5) Turndowns produced by high density atmospheres have considerably more curvature, especially below D = ~10 m. Detection of such a turndown in martian cratering data may constitute evidence of past denser atmospheres, since today's martian atmosphere does not appear capable of causing such sharp turndowns.

6) The presence of significant numbers of icy projectiles (0.1 kg < m < 10^7 kg) in the lunar and martian impactor populations may present a problem for surface dating from crater counts, since such projectiles make a disproportionately large contribution to cratering rates under no-atmosphere conditions (via the 'velocity effect'), but are nearly wiped out by even a 2 mbar atmosphere.

3.5 REFERENCES

Artemieva, N. A., Bland, P. A. 2003. Crater fields on Earth, Venus and Mars, Proc. Lunar Planet. Sci. Conf. 34th, abst.# 1319.

Artemieva, N. A., Shuvalov, V. V. 1996. Interaction of shock waves during the passage of a disrupted meteoroid through the atmosphere. Shock Waves 5, 359-367.

Artemieva, N. A., Shuvalov, V. V. 2001. Motion of a fragmented meteoroid in the planetary atmosphere. J. Geophys. Res. 106, 3297-3310.

Baldwin, B., Schaeffer, Y. 1971. Ablation and breakup of large meteoroids during atmospheric entry. J. Geophys. Res. 76, 4653-4668.

Biberman, L. M., Bronin, S. Y., Brykin, M. V. 1980. Moving of a blunt body through the dense atmosphere under conditions of severe aerodynamic heating and ablation. Acta Astronautica 7, 53-65.

Bills, B. G. 1990. The rigid body obliquity history of Mars. J. Geophys. Res. 95, 14137-14153.

Bland, P. A., Smith, T. B. 2000. Meteorite accumulations on Mars. Icarus 144, 21-26.

Bland, P. A., Artemieva, N. A. 2003. Efficient disruption of small asteroids by Earth's atmosphere. Nature 424, 288-291.

Brown, P. G., ReVelle, D. O., Tagliaferri, E., Hildebrand, A. R. 2002. An entry model for the Tagish Lake fireball using seismic, satellite an infrasound records. Meteorit. Planet. Sci. 37, 661-675.

Byrne, S., Ingersoll, A. P. 2003. A sublimation model for martian south polar features. Science 299, 1051-1053.

Chyba, C. F. 1991. Terrestrial mantle siderophiles and the lunar impact record. Icarus 92, 217-233.

Chyba, C. F., Thomas, P. J., Brookshaw, L., Sagan, C. 1990. Cometary delivery of organic molecules to the early Earth. Science 249, 366-373.

Chyba, C. F., Thomas, P. J., Zahnle, K. J. 1993. The 1908 Tunguska explosion: atmospheric disruption of a stony asteroid. Nature 361, 40-44.

Crater Analysis Techniques Working Group 1979. Standard techniques for presentation and analysis of crater size-frequency data. Icarus 37, 467-474.

Crown, D. A., Berman, D. C., Bleamaster, L. F., Chuang, F. C., Hartmann, W. K. 2005. Martian Highland Paterae: Studies of Volcanic and Degradation Histories from High-Resolution Images and Impact Crater Populations, Proc. Lunar Planet. Sci. Conf. 36th, abst. #1476.

Davis, P. M. 1993. Meteoroid impacts as seismic sources on Mars. Icarus 105, 469-478.

Dycus, R. D. 1969. The meteorite flux at the surface of Mars. Pub. Astron. Soc. Pacific 91, 399-414.

Engel, S., Lunine, J. I., Hartmann, W. K. 1995. Cratering on Titan and implications for Titan's atmospheric history. Planet. Space Sci. 43, 1059-1066.

Feldman, W. C., Maurice, S., Mellon, M. T., Prettyman, T. H., Elphic, R. C., Funsten, H. O., Lawrence, D. J., Tokar, R. L. 2003. Evidence for non-equilibrium distributions of water-equivalent hydrogen deposits near the surface of Mars. Eos (Fall Suppl.) 84, Abstract P32C-02.

Gault, D. E., Wedekind, J. A. 1978. Experimental studies of oblique impact, Proc. Lunar Planet. Sci. Conf. 9th, 3843-3875.

Gilbert, G. K. 1893. The Moon's face, a study of the origin of its features. Bull. Philos. Soc. Wash. DC 12, 241-292.

Glasstone, S. (Ed.) 1957. The Effects of Nuclear Weapons., U. S. Govt. Printing Office, Washington, D. C..

Hartmann, W. K. 1970. Lunar cratering chronology. Icarus 13, 299-301.

Hartmann, W. K. 1977. Relative crater production rates on planets. Icarus 31, 260-276.

Hartmann, W.K. 1999. Martian cratering VI: Crater count isochrons and evidence for recent volcanism from Mars Global Surveyor. Meteorit. Planet. Sci. 34, 167-177.

Hartmann, W. K., Neukum, G. 2001. Cratering chronology and the evolution of Mars. Space Sci. Rev. 96, 165-194.

Head, J. W., Mustard, J. F., Kreslavsky, M. A., Milliken, R. E., Marchant, D. R. 2003. Recent ice ages on Mars. Nature 426, 797-802.

Herrick, R. R., Phillips, R. J. 1994. Effects of the venusian atmosphere on incoming meteoroids and the impact crater population. Icarus 112, 253-281.

Hills, J. G., Goda, M. P. 1993. The fragmentation of small asteroids in the atmosphere. J. Geophys. Res. 105, 1114-1144.

Holsapple, K. A., Schmidt, R. M. 1982. On the scaling of crater dimensions 2: impact processes. J. Geophys. Res. 87, 1849-1870.

Hörz, F., Cintala, M. J., Rochelle, W. C., Kirk, B. 1999. Collisionally processed rocks on Mars. Science 285, 2105-2107.

Hörz, F., Cintala, M. J., Rochelle, W. C., Mitchell, C. M., Smith, R. N., Dobarco-Otero, J., Finch, B. K., See, T. H. 2004. Atmospheric entry studies and the smallest impact craters on Mars, Proc. Lunar Planet. Sci. Conf. 35th, abstract #1116

Ip, W.-H. 1990. Meteoroid ablation processes in Titan's atmosphere. Science 345, 511-512.

Ivanov, B. A. 2001. Mars/Moon cratering rate ratio estimates. Space Sci. Rev. 96, 87-104.

James, P. B., Kieffer, H. H., Paige, D. A. 1992. The seasonal cycle of carbon dioxide on Mars. In: Kieffer, H. H., Jakosky, B. M., Snyder, C. W., Matthews, M. S. (eds.), Mars. U. of Arizona Press, Tucson, 934-968.

Masson, D. J., Morris, D. N., Bloxsom, D. E. 1961. Measurements of sphere drag from hypersonic continuum to free-molecular flow. Rarefied Gas Dyn. 3, 643-661.

McEwen, A. S. and 12 others 2002. HiRISE: the High Resolution Imaging Science Experiment, Proc. Lunar Planet. Sci. Conf. 33rd, abstract #1163.

McEwen, A., Turtle, E., Burr, D., Milazzo, M., Lanagan, P., Christensen, P., Boyce, J. 2003. Discovery of a large rayed crater on Mars: Implications for recent volcanic and fluvial activity and the origin of martian meteorites, Proc. Lunar Planet. Sci. Conf. 34th, abstract #2040.

Melosh, H. J. 1989. Impact Cratering: A Geologic Process (1st ed.). Oxford Univ. Press, New York.

Neukum, G., Ivanov, B. A., Hartmann, W. K. 2001. Cratering records in the inner solar system in relation to the lunar reference system. Space Sci. Rev. 96, 55-86.

Neukum, G., Wise, D. U. 1976. Mars: A standard crater curve and possible new time scale. Science 194, 1381-1387.

Oberst, J., Nakamura, Y. 1987. Distinct meteoroid families identified on the lunar seismograms, Proc. Lunar Planet. Sci. Conf. 17th, J. Geophys. Res., 92, E769-E773.

Oberst, J., Nakamura, Y. 1991. A search for clustering among the meteoroid impacts detected by the Apollo Lunar Seismic Network. Icarus 91, 315-325.

Passey, Q. R., Melosh, H. J. 1980. Effects of atmospheric breakup on crater field formation. Icarus 42, 211-233.

Podolak, M., Pollack, J. B., Reynolds, R. T., 1988. Interactions of planetisimals with protoplanetary atmospheres. Icarus, 73, 163-179

Popova, O., Nemtchinov, I., Hartmann, W. K. 2003. Bolides in the present and past martian atmosphere and effects on cratering processes. Meteorit. Planet. Sci. 38, 905-925.

Rahe, J., Vanysek, V., Weissman, P. R. 1994. Properties of cometary nuclei. In: Gehrels, T. (ed.), Hazards due to comets and asteroids. U. of Arizona Press, Tucson, 597-634.

Raymond, J. C. and 12 others 1998. Solar wind at 6.8 solar radii from UVCS observation of comet C/1996Y1. AstroPhys. J. 508, 410-417.

Remo, J. L. 1994. Classifying and modeling NEO material properties and interactions. In: Gehrels, T. (ed.), Hazards due to comets and asteroids. U. of Arizona Press, Tucson, 551-596.

Rochelle, W. C., Kirk, B., Smith, N., DeVall, M., Hörz, F. 1999. Atmospheric entry and survival of small meteorites on Mars, Proc. Lunar Planet. Sci. Conf. 30th, abst.# 1651.

Schultz, P. H., Gault, D. E. 1985. Clustered impacts: Experiments and implications. J. Geophys. Res. 90, 3701-3732.

Sekanina, Z. 1982. The problem of split comets in review. In: Wilkening, L. L. (ed.), Comets. U. of Arizona Press, Tucson, 251-287.

Sekanina, Z. 1993. Disintegration phenomena expected during collision of comet Shoemaker-Levi 9 with Jupiter. Science 262, pp.382-387.

Shuvalov, V. V., Artemieva, N. A., Trubetskaya, I. A. 2000. Simulating the motion of a disrupted meteoroid with allowance for evaporation. Sol. Syst. Res. 34, 49-60.

Smith, D. E., Zuber, M. T. 1998. The relationship between MOLA northern hemisphere topography and the 6.1 mbar atmospheric pressure surface of Mars. Geophys. Res. Let. 25, 4397-4400.

Tholen, D. J. 1989. Asteroid Taxonomy classifications. In: Binzel, R. P., Gehrels, T., Matthews, M. S. (eds.), Asteroids II. U. of Arizona Press, Tucson, 1139-1150.

Titus, T. N., Kieffer, H. H., Christensen, P. R. 2003. Exposed water ice discovered near the south pole of Mars. Science 299, 1051-1053.

Uzzo, M., Raymond, J. C., Biesecker, D., Marsden, B., Wood, C., Ko Y.-K., Wu, R. 2001. Results from UVCS and LASCO observation of the sungrazing comet C/2000C6, AstroPhys. J. 558, 403-410.

Vasavada, A. R., Milavec, T. J., Paige, D. A. 1993. Microcraters on Mars: Evidence for past climate variations. J. Geophys. Res. 98, 3469-3476.

Ward, W. R. 1974. Climatic variations on Mars, 1: Astronomical theory of insolation. J. Geophys. Res. 79, 3375-3386.

Weibull, W. A. 1939. A statistical theory of the strength of materials, Proc. Royal Swedish Acad. of Engineering and Science, no. 151.

Wetherill, G. W., Shoemaker, E. M. 1982. Collision of astronomically observable bodies with the Earth. Geological Society of America Special Paper 190, 1-13.

Zahnle, K. J. 1992. Airburst origin of dark shadows on Venus. J. Geophys. Res. 97, 10243-10255.

3.6 TABLES

Table 3.1: Mars meteoroid properties.

Physical Properties	Object Type			
	Icy	*Carbonaceous*	*Stony*	*Iron*
% of asteroidals by mass	N/A	75%	16.25%	8.75%
Density (kg m^{-3})	1100.0[2,4]	2500.0[4]	3500.0[2,4,8]	7500.0[2,4,8]
Heat of ablation (kJ kg^{-1})	1600.0[3]	3200.0[3]	5000.0[3]	5000.0[1,3]
Mean strength (MN m^{-2})	2.0[4,5,6]	10.0[4,5]	50.0[4,5,7,8]	200.0[1,5,7,8]

	S. P.	*L. P.*	*Asteroidal*
v_{min} (km s^{-1})	14	30	7
v_o (km s^{-1})	29	40	--
v_{max} (km s^{-1})	44	50	31

Works consulted:

[1] Passey and Melosh, 1980.
[2] Podolak, et al., 1988.
[3] Chyba et al., 1990.
[4] Chyba, et al., 1993.
[5] Hills and Goda, 1993.
[6] Rahe et al., 1994.
[7] Remo, 1994.
[8] Bland and Artemieva, 2003.

Abbreviations:

L. P. : Long-period comet.
S. P. : Short-period comet.

3.7 FIGURES

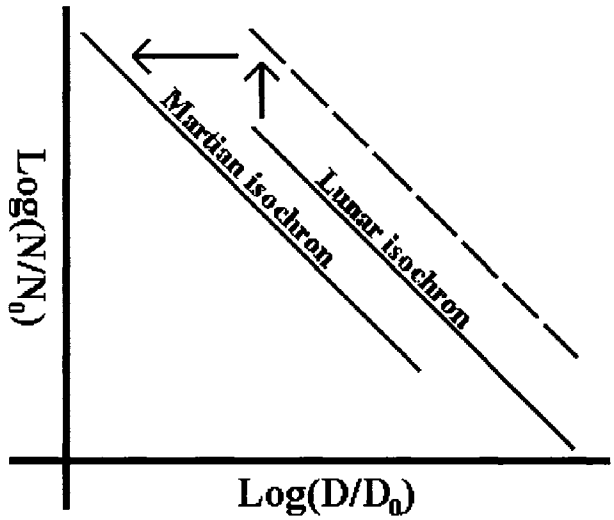

Figure 3.1: Translation of a lunar isochron into a martian isochron. The upward shift accounts for higher impact rates and the leftward shift accounts for lower impact velocites and higher surface gravity (Neukum and Wise, 1976), on Mars vs. the Moon.

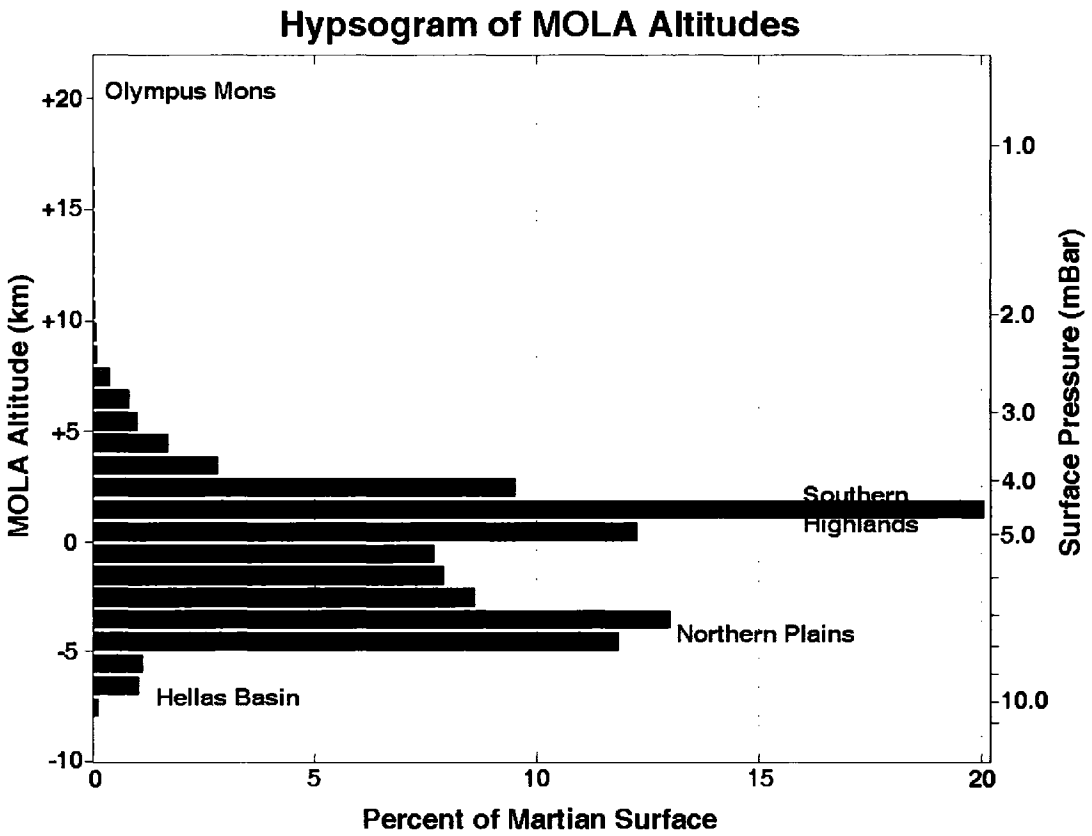

Figure 3.2: Hypsogram of Mars from MOLA measurements. A hypsogram of Mars derived from Mars Orbital Laser Altimeter measurements. Surfaces range from ~ -8 to 22 km in altitude relative to the MOLA datum (Smith and Zuber, 1998).

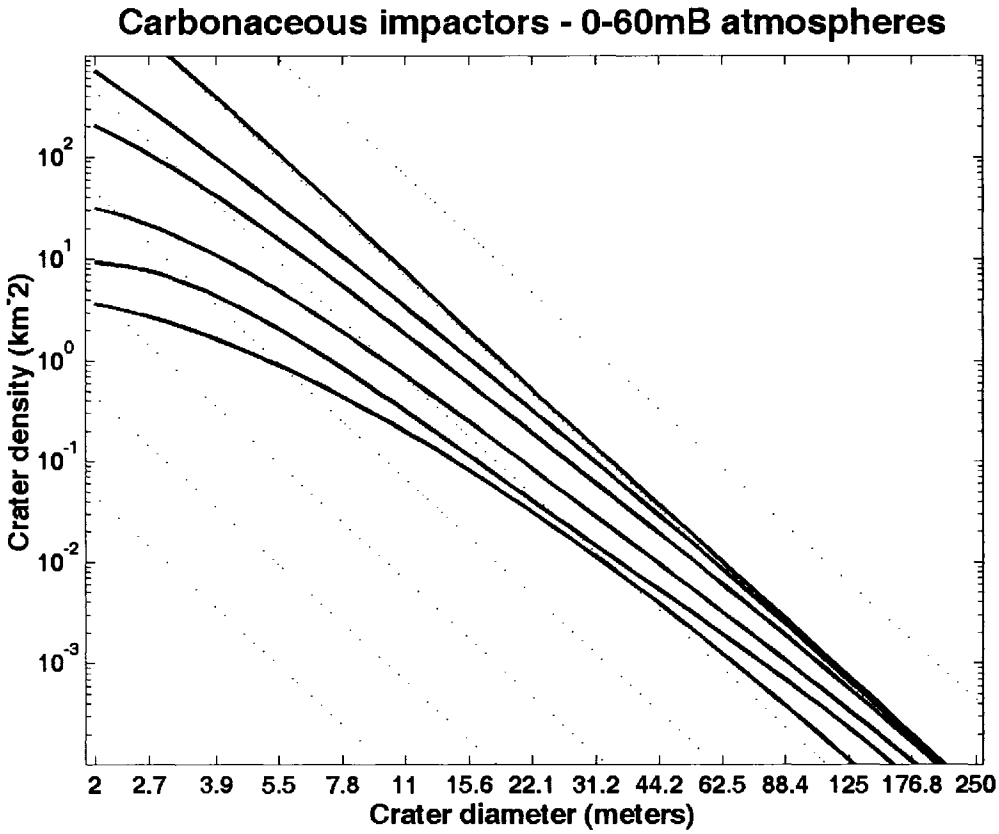

Figure 3.3a: SFDs for cratering by carbonaceous chondrite objects. Incremental size-frequency distributions for cratering by carbonaceous chondrite objects under atmospheres of (top to bottom) 0, 2, 6, 20, 40 and 60 mbar, plotted over arbitrary reference isochrons. Cratering densities are arbitrary.

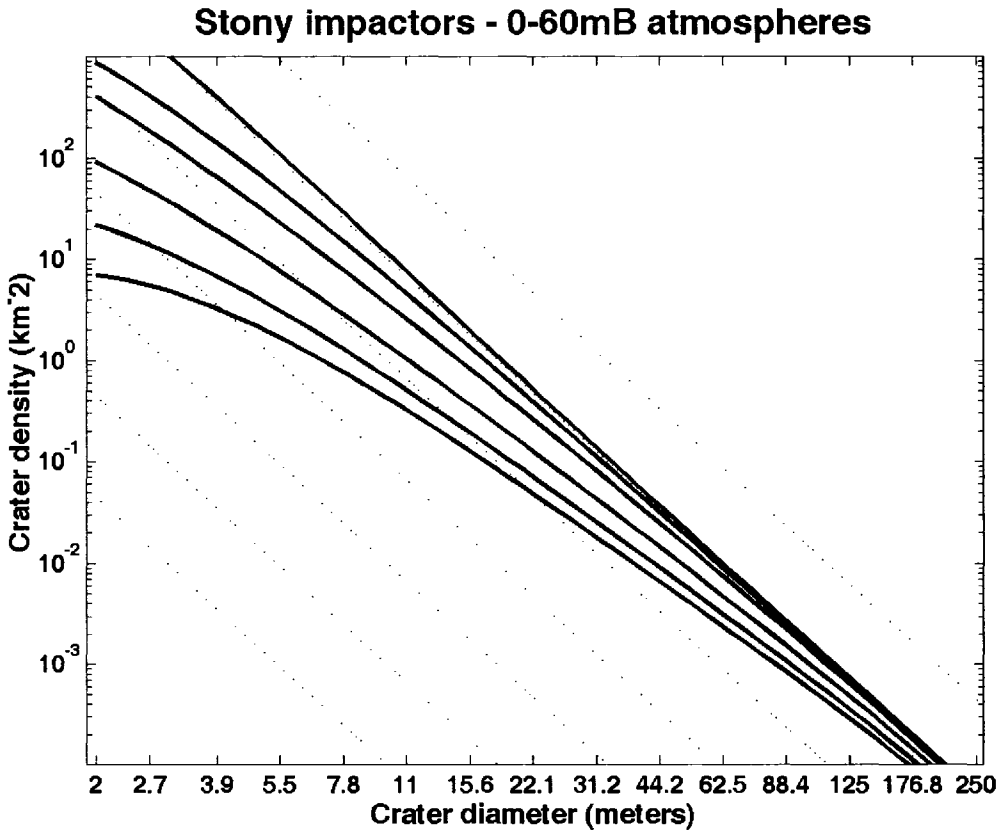

Figure 3.3b: SFDs for cratering by stony objects. Incremental size-frequency distributions for cratering by stony objects under atmospheres of (top to bottom) 0, 2, 6, 20, 40 and 60 mbar, plotted over arbitrary reference isochrons. Cratering densities are arbitrary.

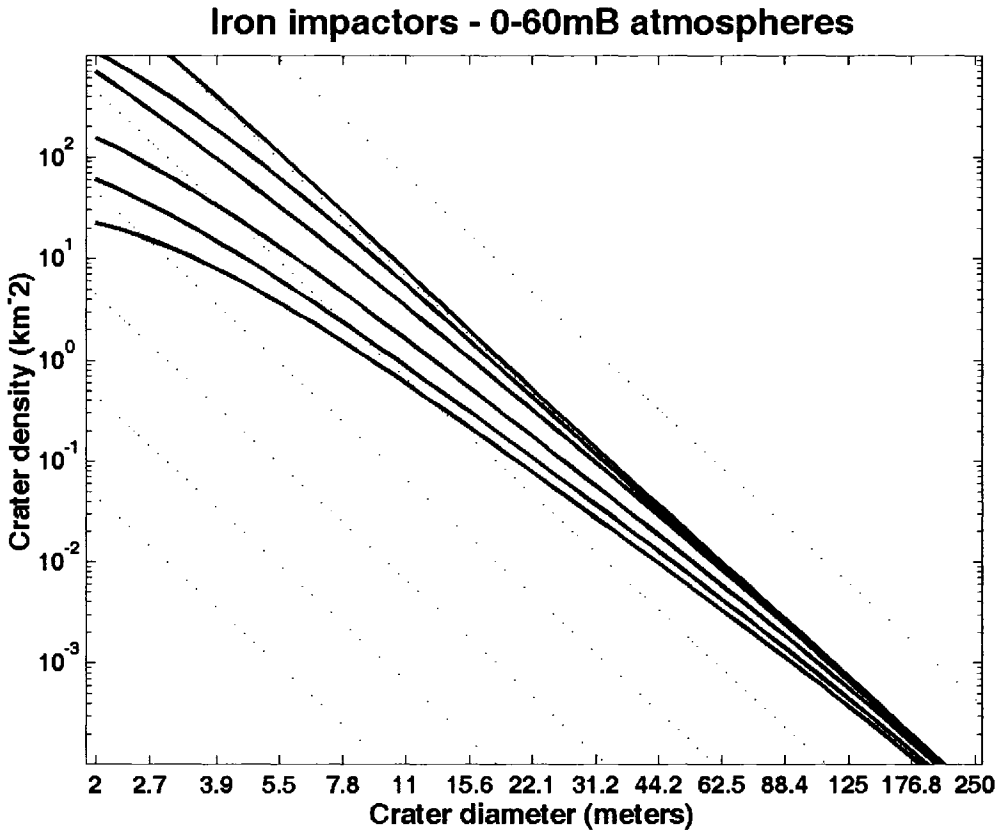

Figure 3.3c: SFDs for cratering by iron objects. Incremental size-frequency distributions for cratering by iron objects under atmospheres of (top to bottom) 0, 2, 6, 20, 40 and 60 mbar, plotted over arbitrary reference isochrons. Cratering densities are arbitrary.

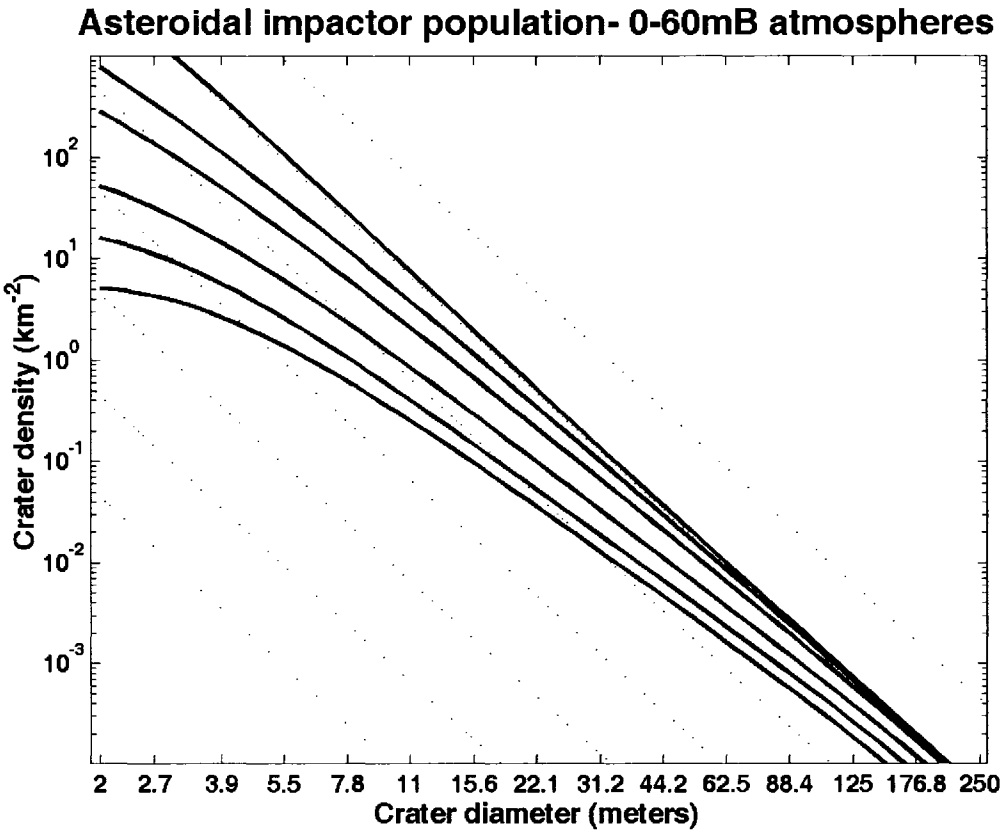

Figure 3.3d: SFDs for cratering by carbonaceous chondrite, stony and iron objects. Incremental size-frequency distributions for cratering by a population of 75% carbonaceous chondrite, 16% stony, and 9% iron objects under atmospheres of (top to bottom) 0, 2, 6, 20, 40 and 60 mbar, plotted over arbitrary reference isochrons. Cratering densities are arbitrary.

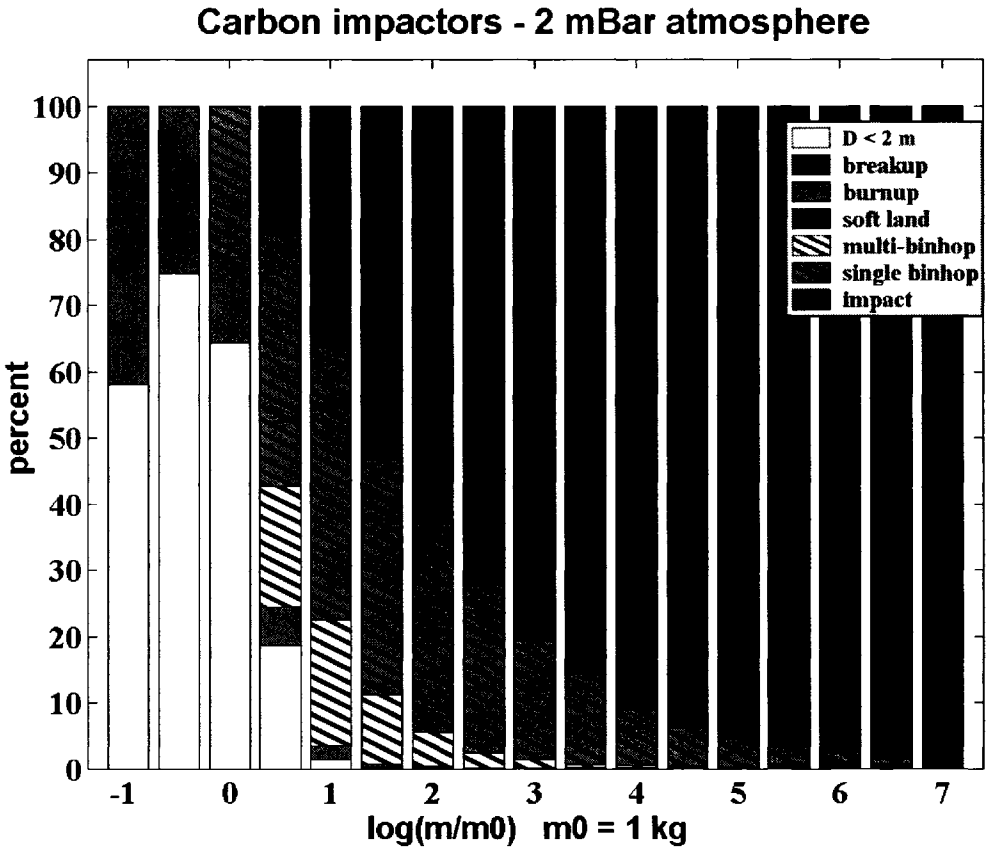

Figure 3.4a: Outcomes for carbonaceous chodrites passing through 2 mbar atmosphere. Stacked histograms of outcomes for carbonaceous impactors passing through a 2 mbar martian atmosphere. Cross-hatched area represents crater-forming impacts.

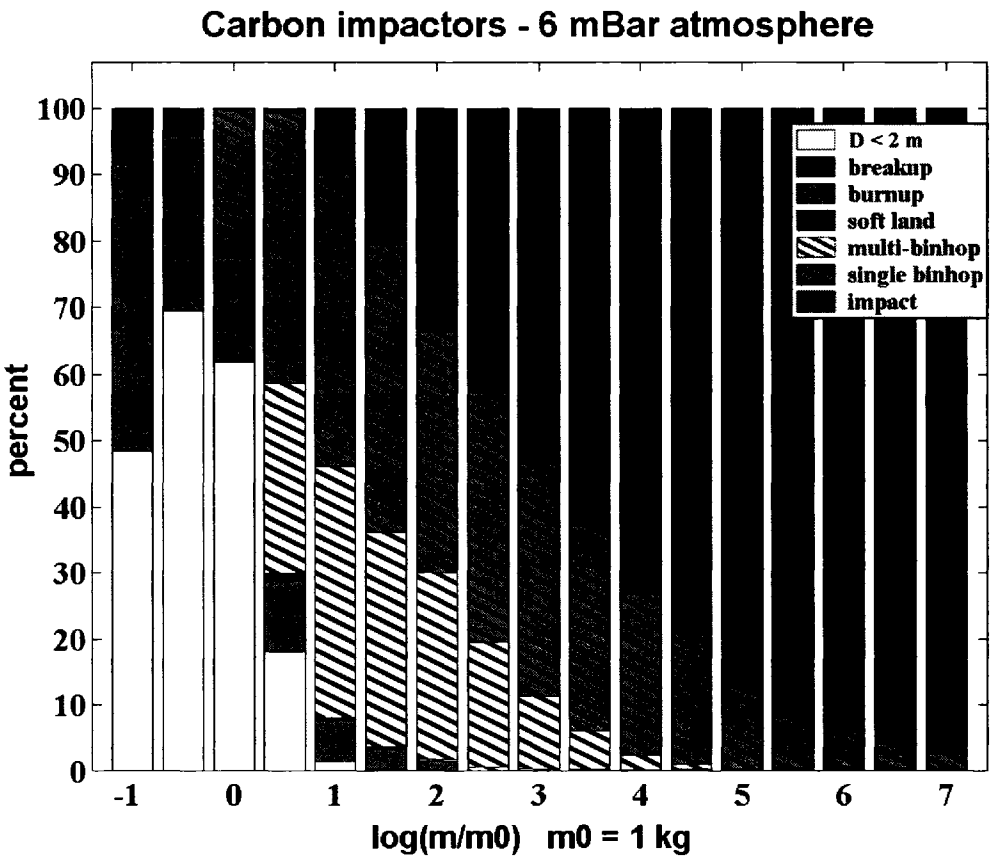

Figure 3.4b: Outcomes for carbonaceous chodrites passing through 6 mbar atmosphere. Stacked histograms of outcomes for carbonaceous impactors passing through a 6 mbar martian atmosphere. Cross-hatched area represents crater-forming impacts.

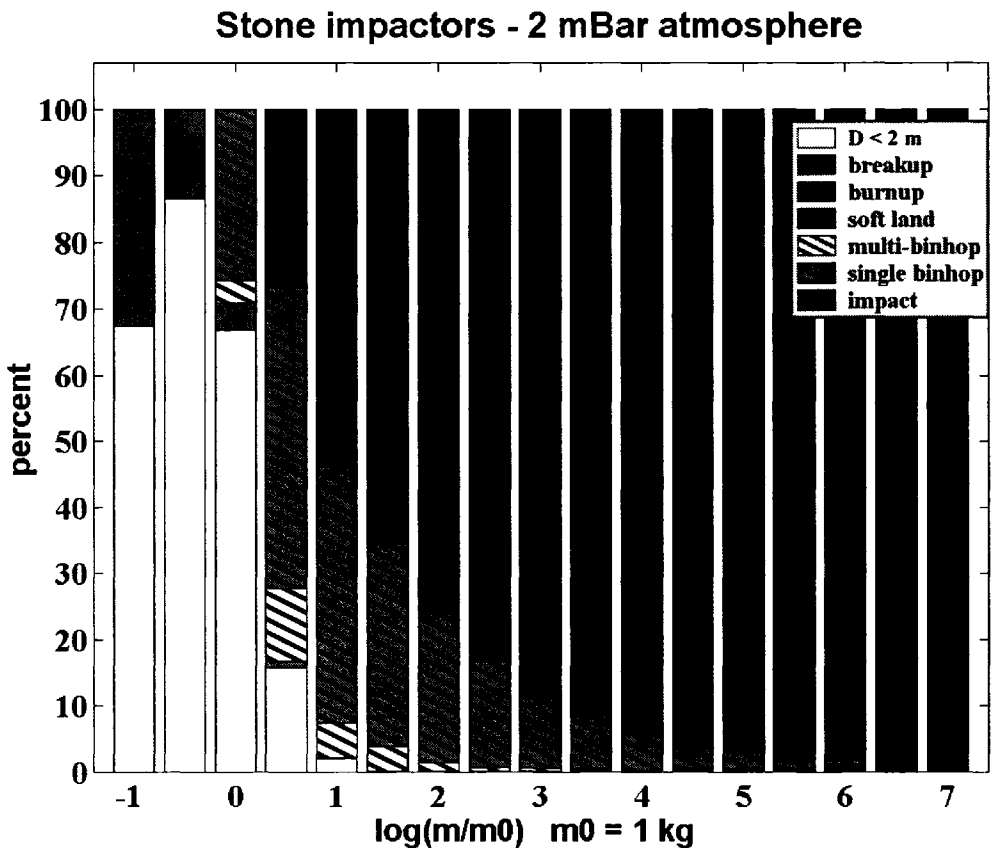

Figure 3.4c: Outcomes for stones passing through 2 mbar atmosphere. Stacked histograms of outcomes for stony impactors passing through a 2 mbar martian atmosphere. Cross-hatched area represents crater-forming impacts.

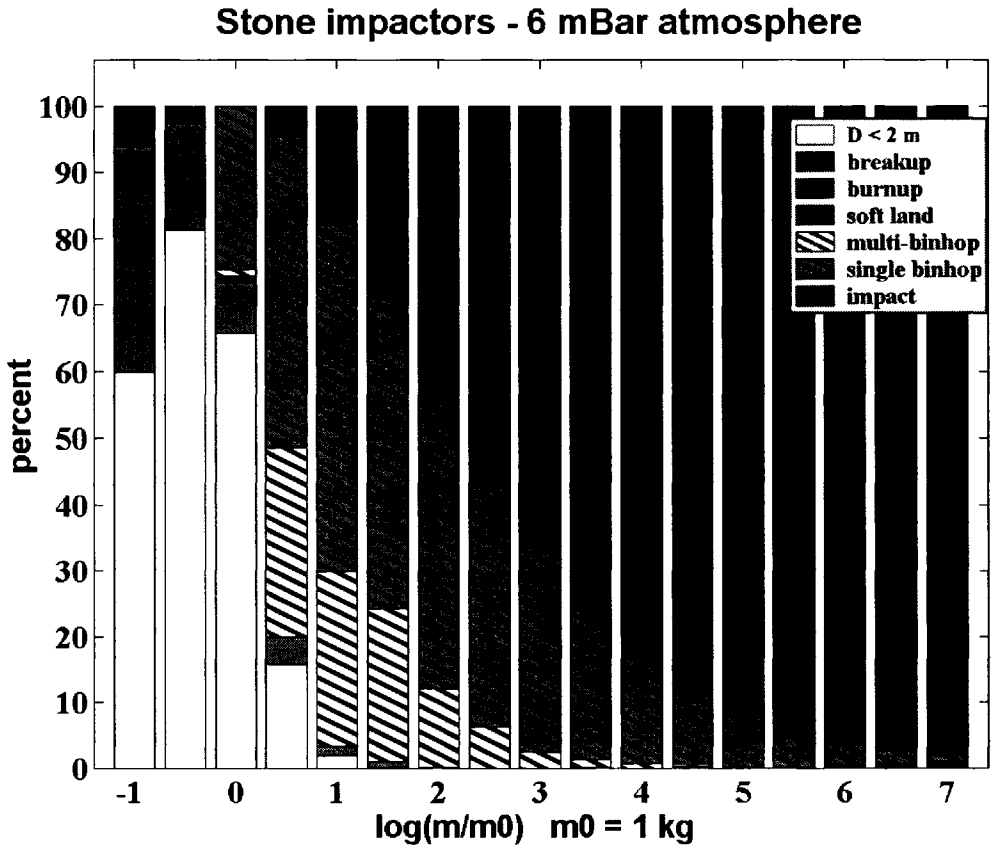

Figure 3.4d: Outcomes for stones passing through 6 mbar atmosphere. Stacked histograms of outcomes for stony impactors passing through a 6 mbar martian atmosphere. Cross-hatched area represents crater-forming impacts.

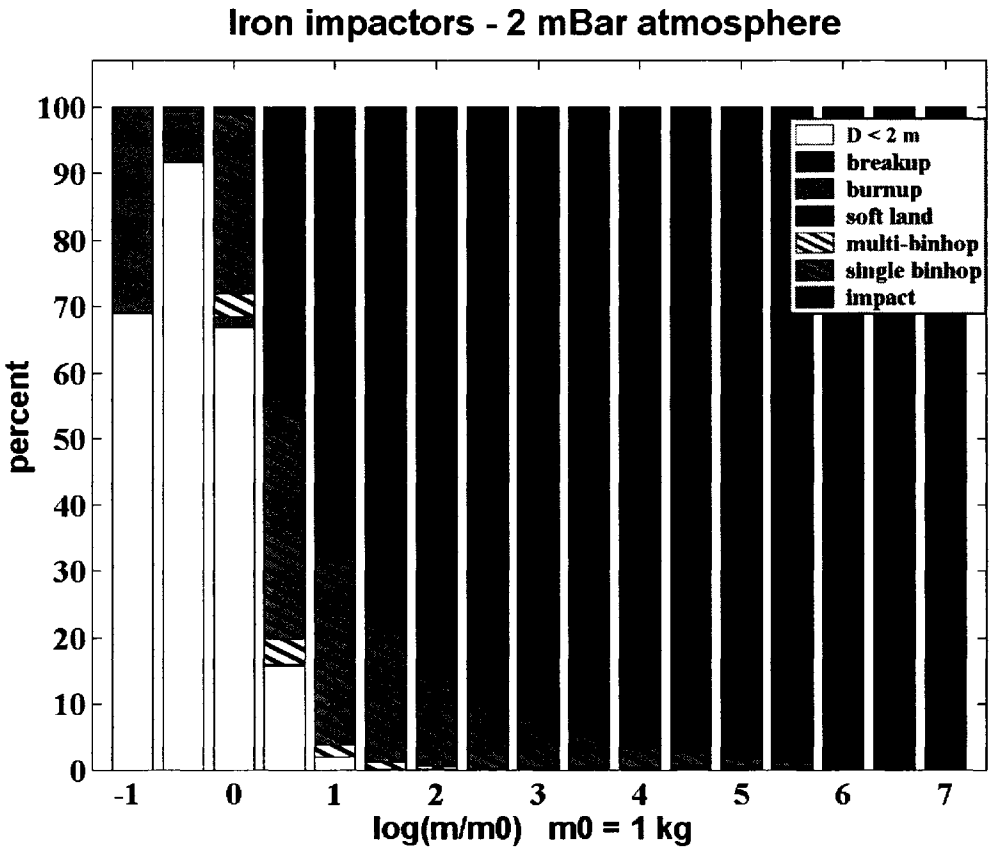

Figure 3.4e: Outcomes for irons passing through 2 mbar atmosphere. Stacked histograms of outcomes for iron impactors passing through a 2 mbar martian atmosphere. Cross-hatched area represents crater-forming impacts.

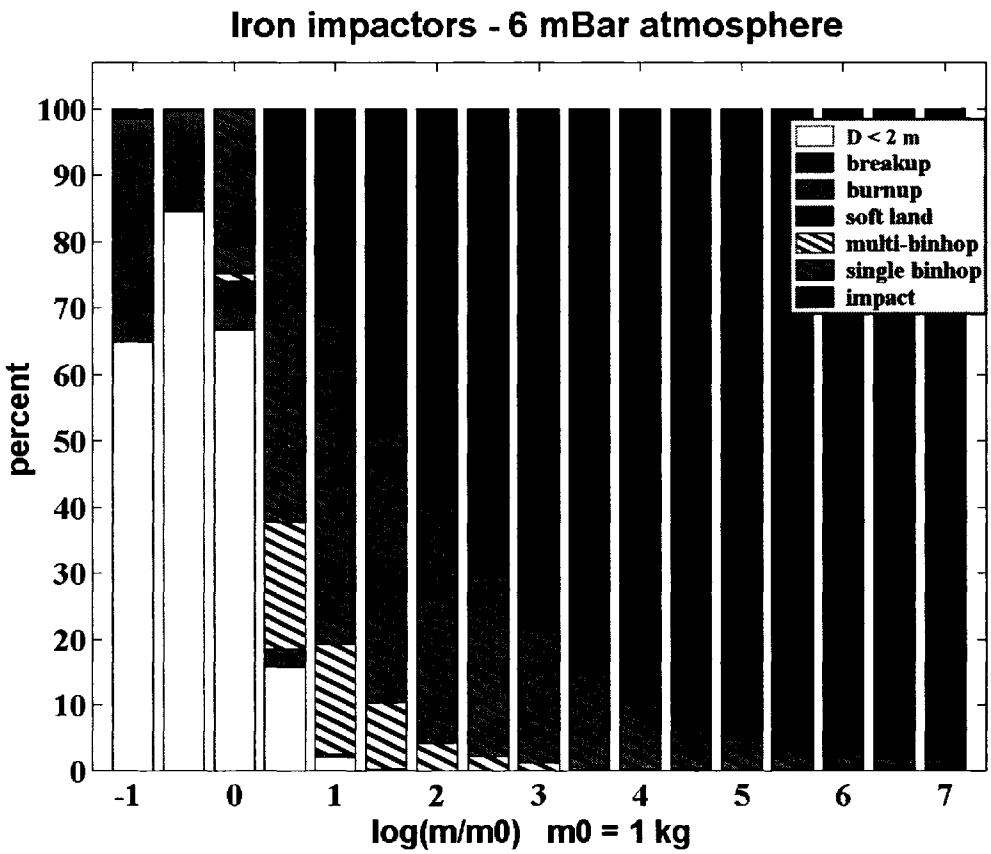

Figure 3.4f: Outcomes for irons passing through 6 mbar atmosphere Stacked histograms of outcomes for iron impactors passing through a 6 mbar martian atmosphere. Cross-hatched area represents crater-forming impacts.

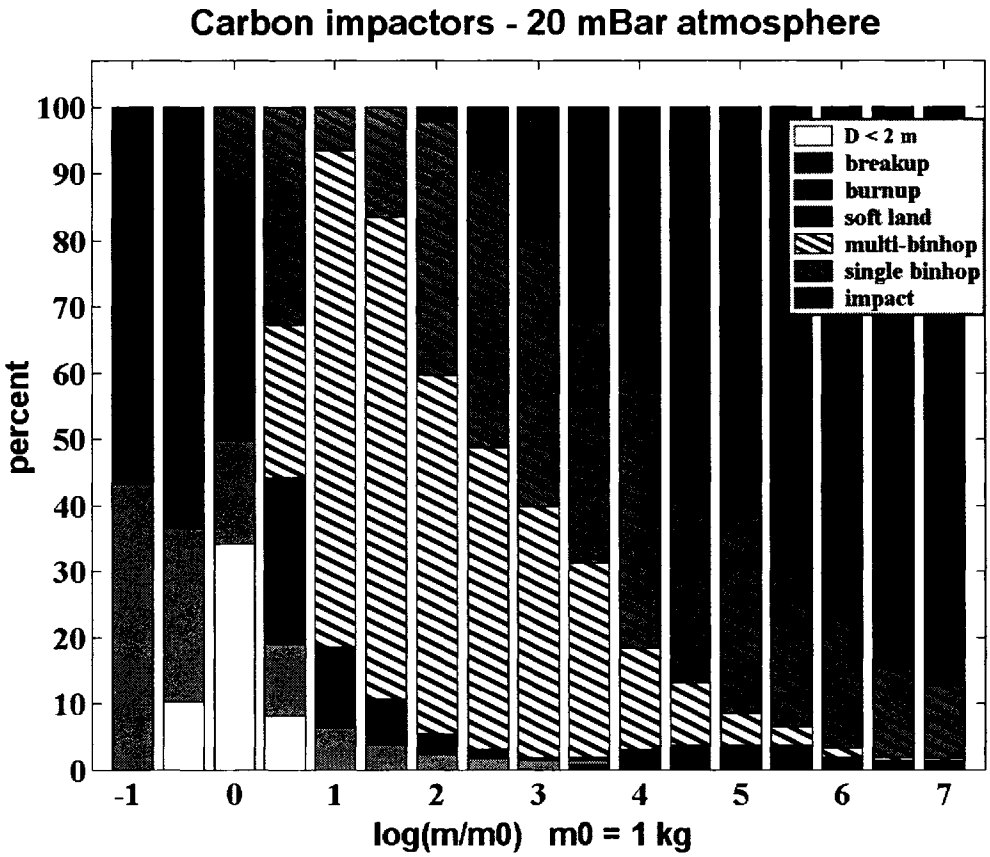

Figure 3.5a: Outcomes for carbonaceous chodrites passing through 20 mbar atmosphere. Stacked histograms of outcomes for carbonaceous impactors passing through a 20 mbar martian atmosphere. Cross-hatched area represents crater-forming impacts. The anomalous 'single binhop' results in the fourth column is due to a crater sub-population falling near a bin-boundary.

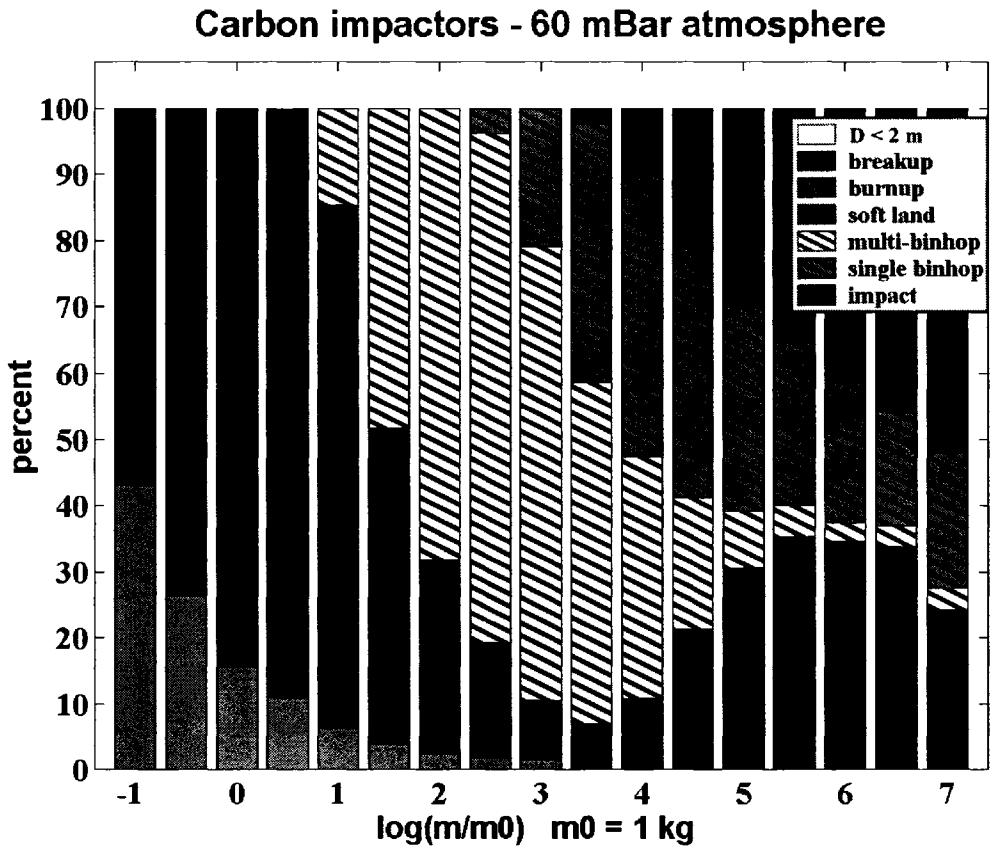

Figure 3.5b: Outcomes for carbonaceous chodrites passing through 60 mbar atmosphere. Stacked histograms of outcomes for carbonaceous impactors passing through a 60 mbar martian atmosphere. Cross-hatched area represents crater-forming impacts.

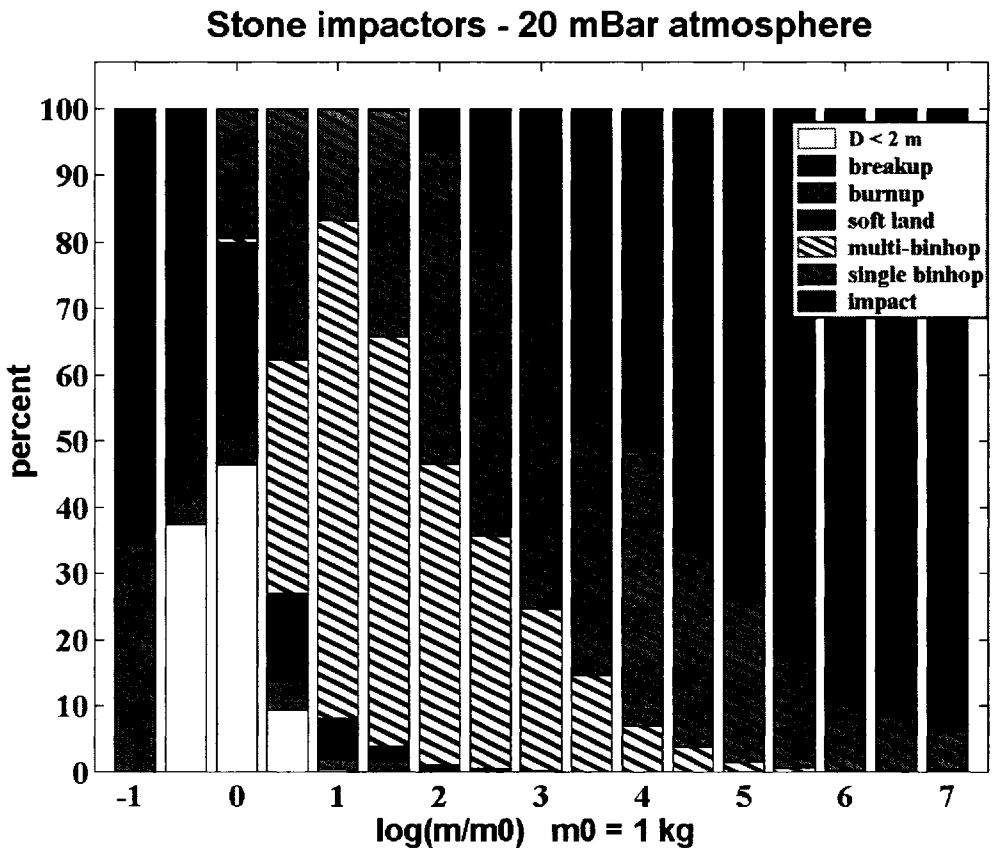

Figure 3.5c: Outcomes for stones passing through 20 mbar atmosphere. Stacked histograms of outcomes for stony impactors passing through a 20 mbar martian atmosphere. Cross-hatched area represents crater-forming impacts.

The anomalous 'single binhop' results in the fourth column is due to a crater sub-population falling near a bin-boundary.

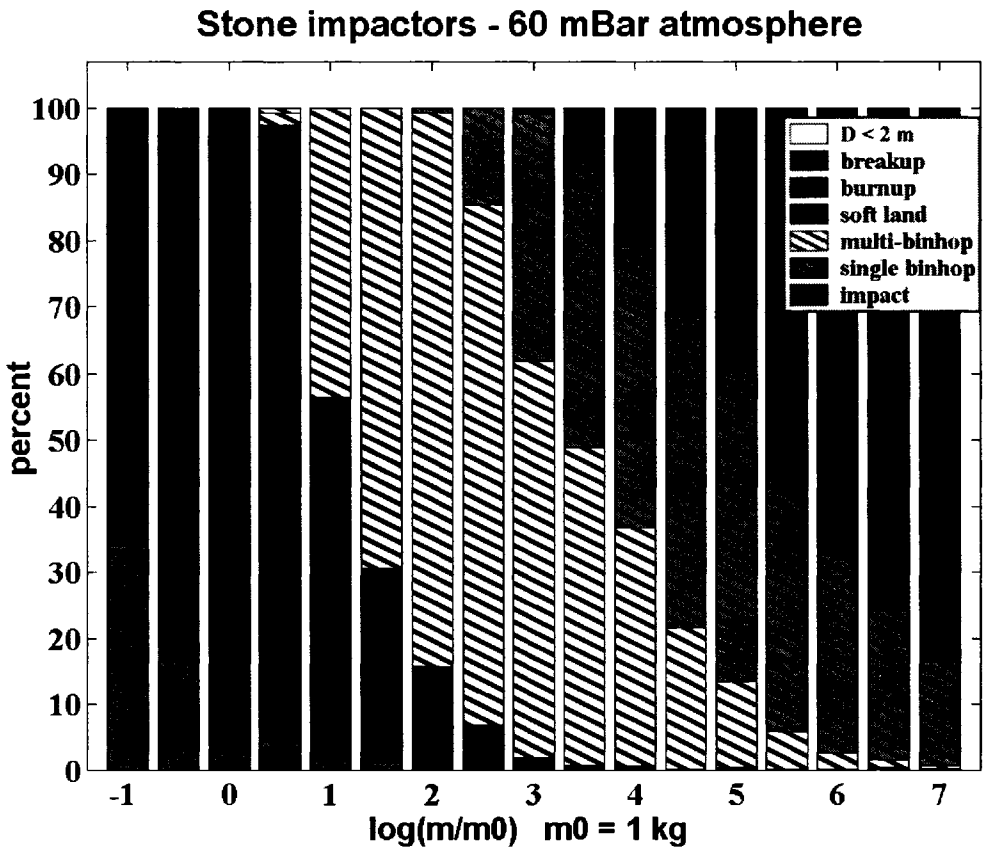

Figure 3.5d: Outcomes for stones passing through 60 mbar atmosphere. Stacked histograms of outcomes for stony impactors passing through a 60 mbar martian atmosphere. Cross-hatched area represents crater-forming impacts.

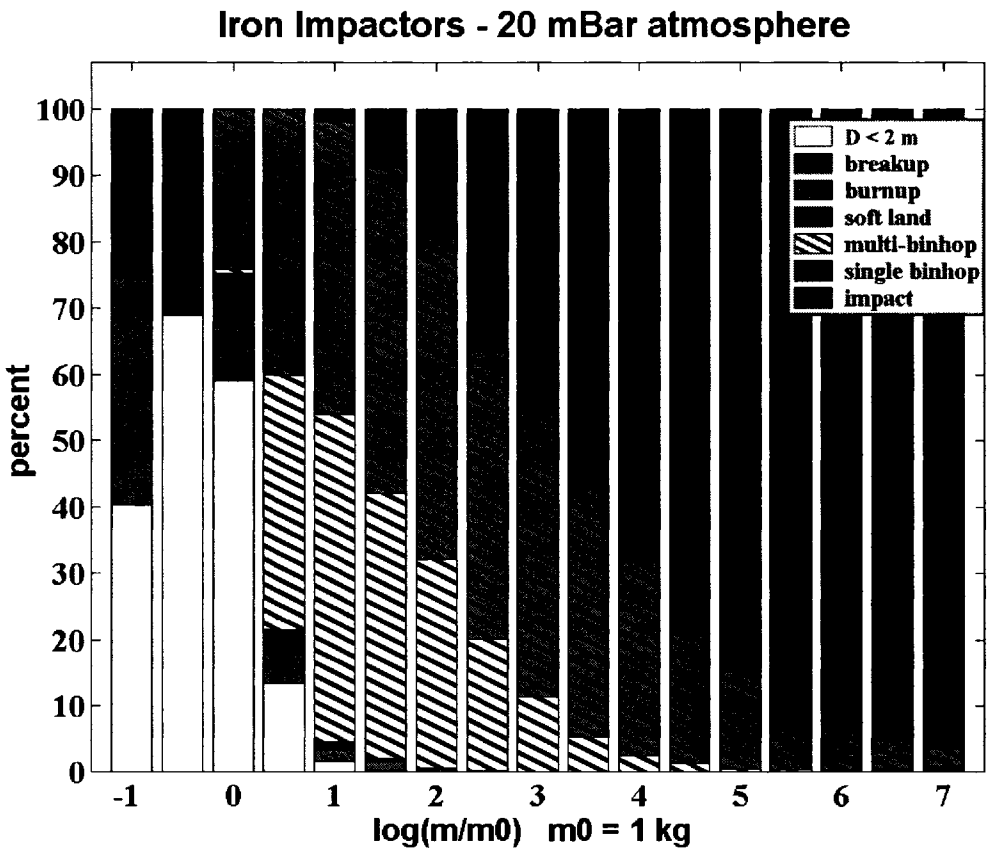

Figure 3.5e: Outcomes for irons passing through 20 mbar atmosphere. Stacked histograms of outcomes for iron impactors passing through a 20 mbar martian atmosphere. Cross-hatched area represents crater-forming impacts. The anomalous 'single binhop' results in the fourth column are due to a crater sub-population falling near a bin-boundary.

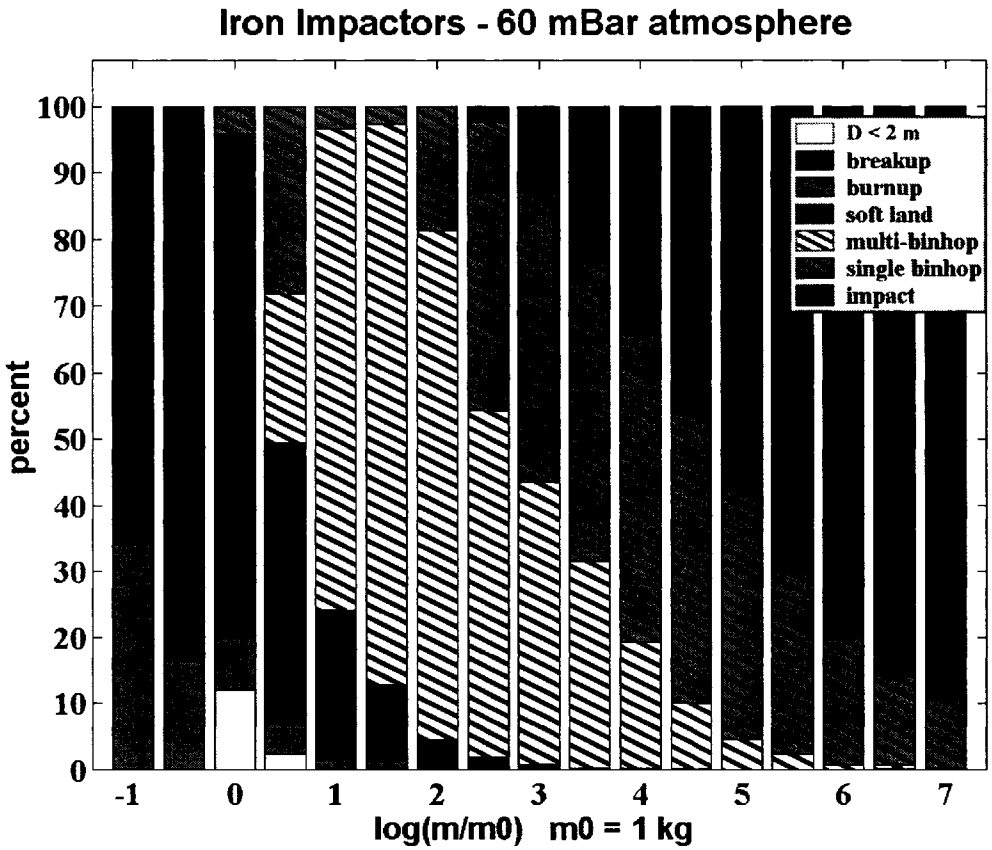

Figure 3.5f: Outcomes for irons passing through 60 mbar atmosphere. Stacked histograms of outcomes for iron impactors passing through a 60 mbar martian atmosphere. Cross-hatched area represents crater-forming impacts.

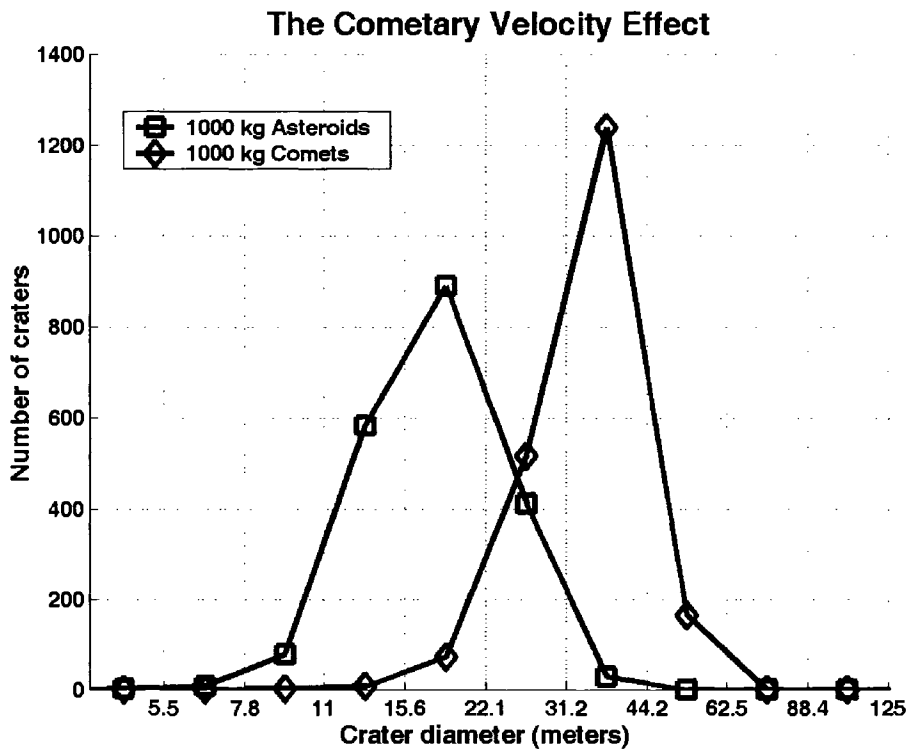

Figure 3.6: Comparison of cratering due to asteroidal and cometary projectiles. A comparison of cratering due to the 1000 kg sub-populations of 2000 asteroidal and 2000 cometary projectiles demonstrating the 'velocity effect'.

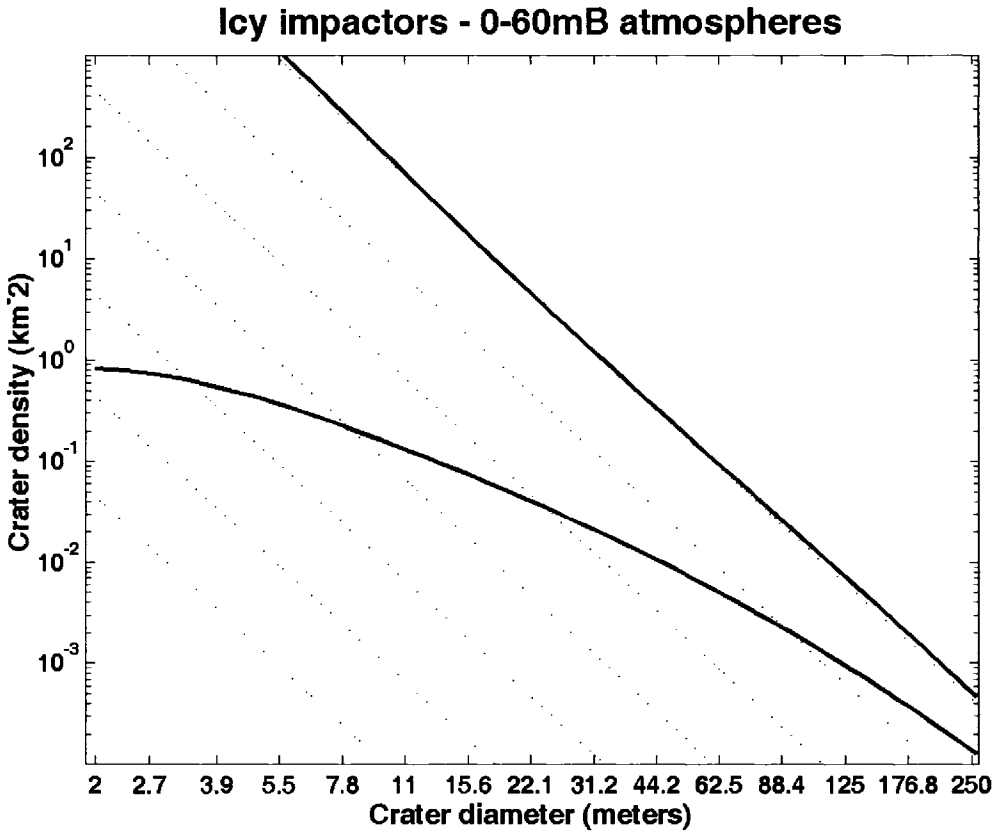

Figure 3.7: SFD for cratering by icy objects. Incremental size-frequency distributions for cratering by icy objects under atmospheres of (top to bottom) 0 and 2mbar, similar to Figs. 3.3, plotted over arbitrary reference isochrons. Data for 6 mbar and greater are not statistically significant and are not plotted. Cratering densities are arbitrary.

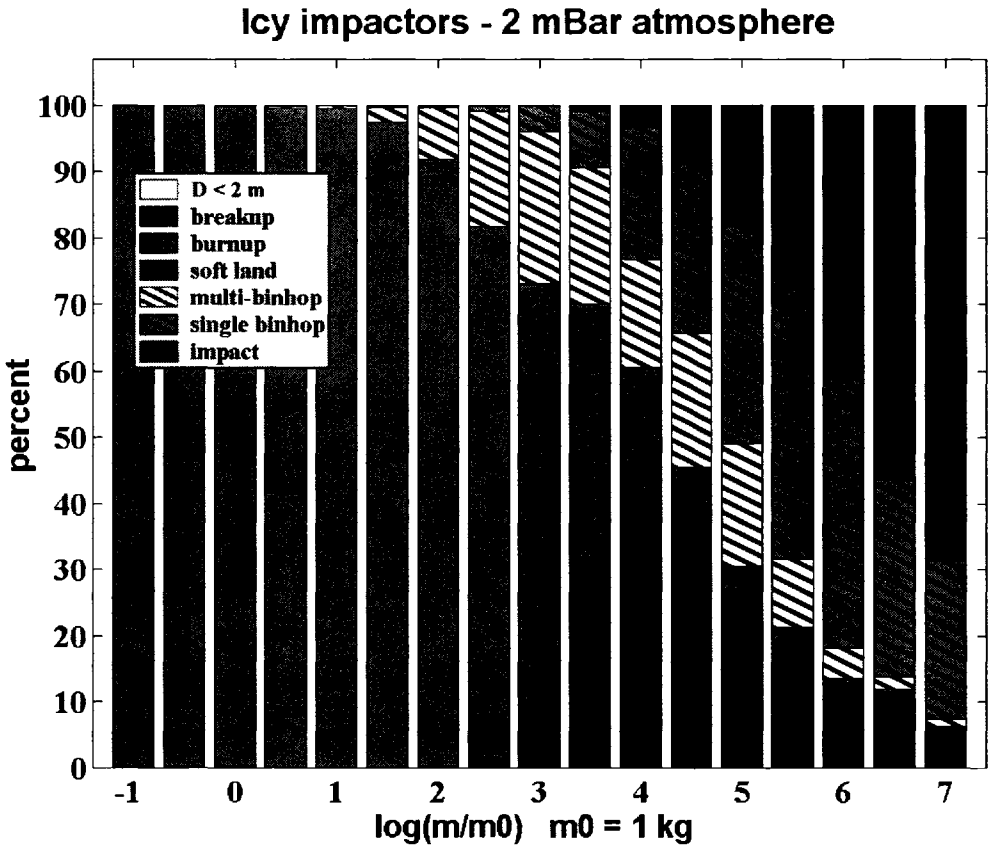

Figure 3.8a: Outcomes for icy impactors passing through 2 mbar atmosphere. Stacked histograms of outcomes for icy impactors passing through a 2 mbar martian atmosphere. Cross-hatched area represents crater-forming impacts.

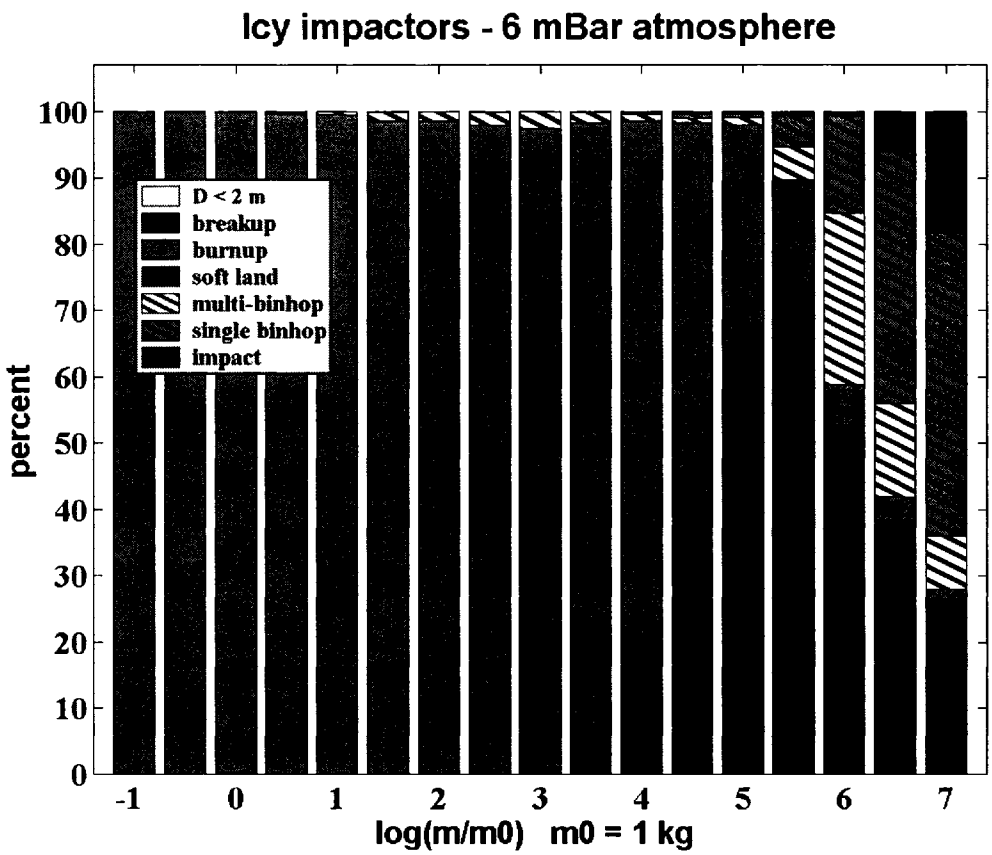

Figure 3.8b: Outcomes for icy impactors passing through 6 mbar atmosphere. Stacked histograms of outcomes for icy impactors passing through a 6 mbar martian atmosphere. Cross-hatched area represents crater-forming impacts.

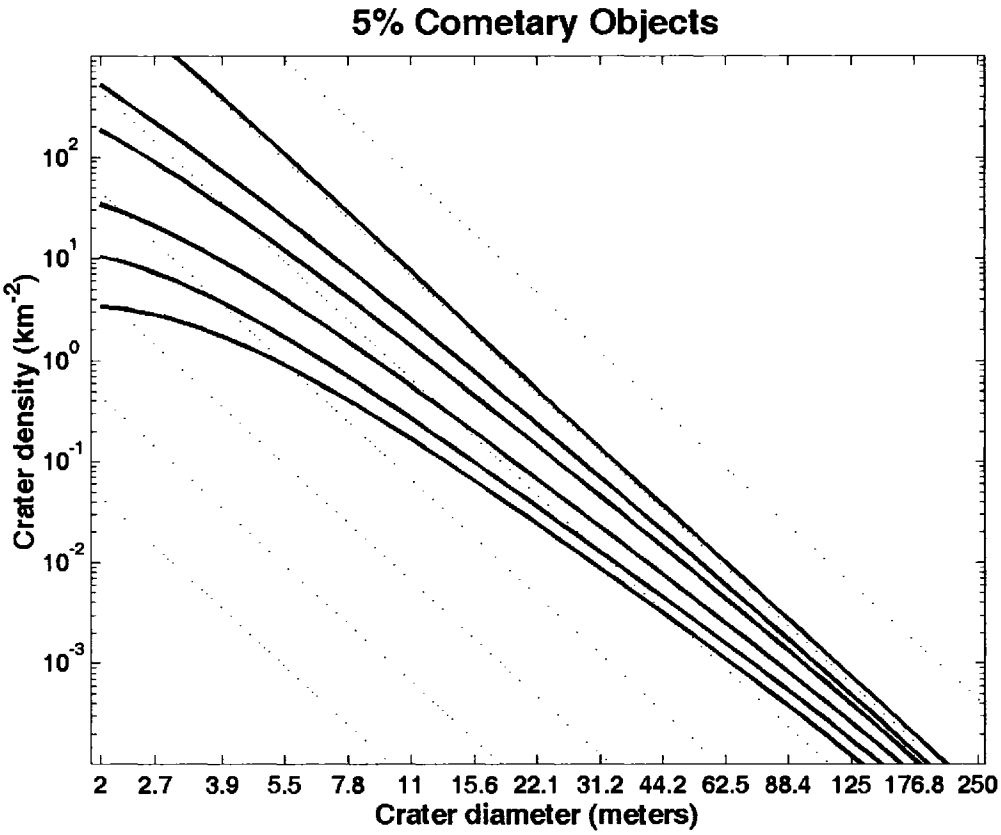

Figure 3.9a: SFD for cratering by a population of 5% cometary objects. Incremental size-frequency distributions for cratering by a population of 5% cometary objects under atmospheres of (top to bottom) 0, 2, 6, 20, 40 and 60 mbar, plotted over arbitrary reference isochrons. Cratering densities are arbitrary.

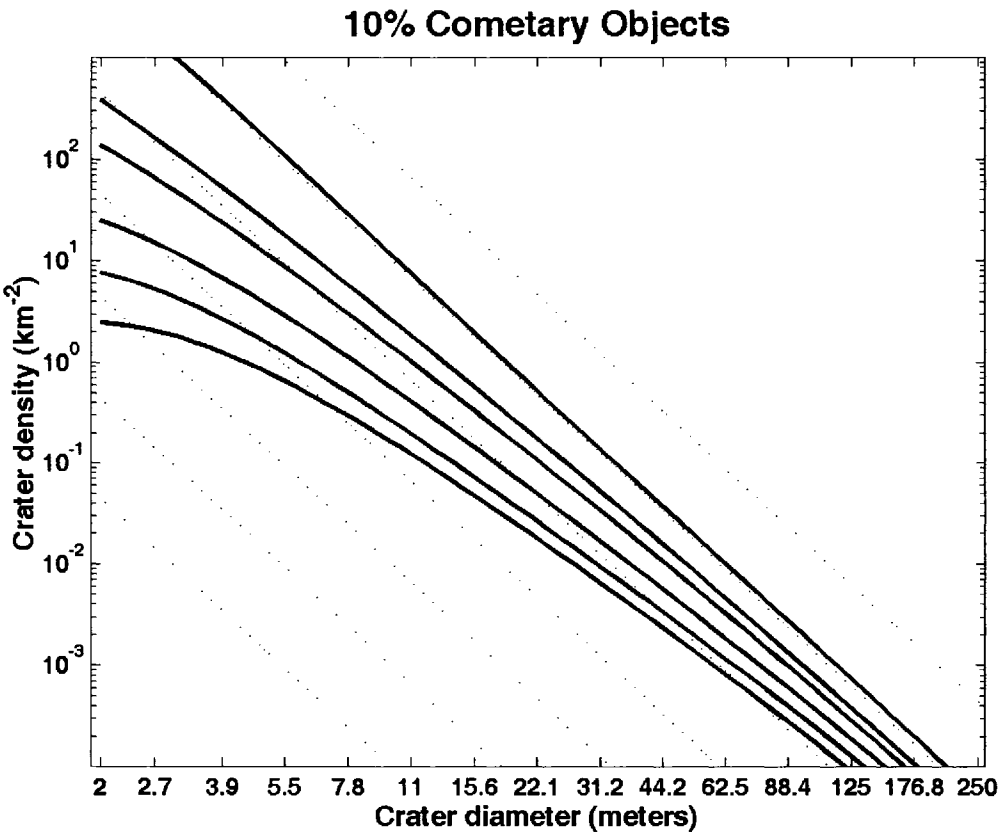

Figure 3.9b: SFD for cratering by a population of 10% cometary objects. Incremental size-frequency distributions for cratering by a population of 10% cometary objects under atmospheres of (top to bottom) 0, 2, 6, 20, 40 and 60 mbar, plotted over arbitrary reference isochrons. Cratering densities are arbitrary.

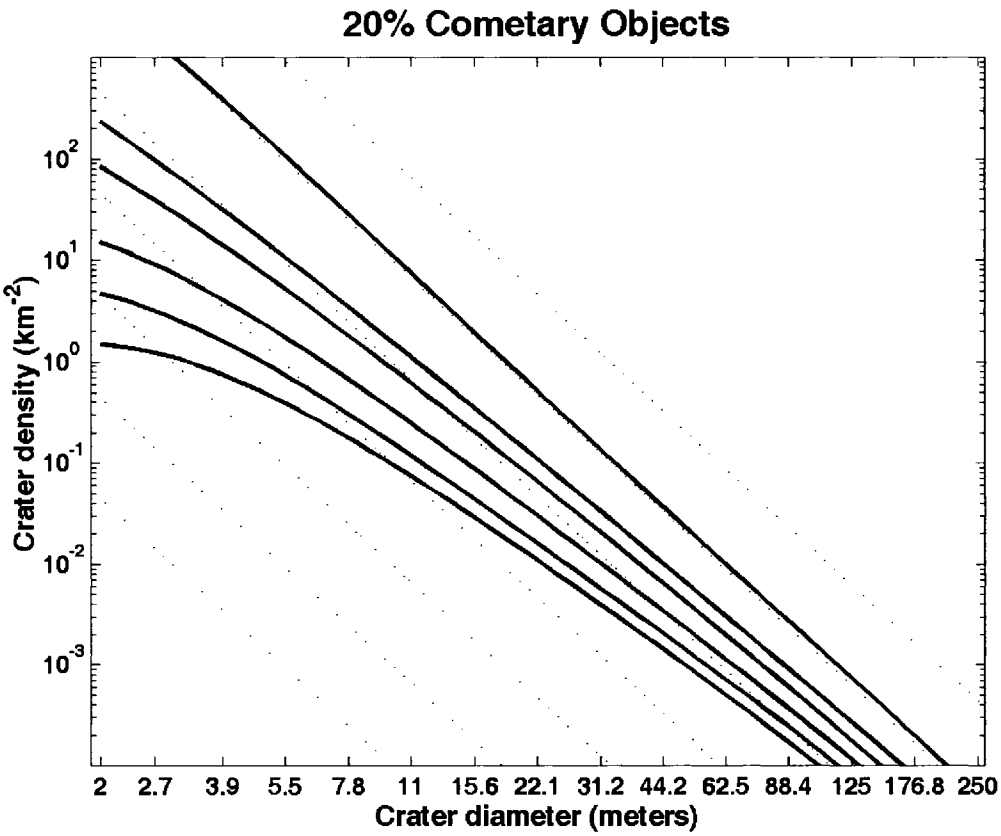

Figure 3.9c: SFD for cratering by a population of 20% cometary objects. Incremental size-frequency distributions for cratering by a population of 20% cometary objects under atmospheres of (top to bottom) 0, 2, 6, 20, 40 and 60 mbar, plotted over arbitrary reference isochrons. Cratering densities are arbitrary.

Chapter 4

Atmospheric variations and meteorite production on Mars*

4.1 INTRODUCTION

Essentially all meteoroids incident on a large planetary body without an atmosphere (e.g., the Moon) impact at their cosmic velocities of at least several kilometers per second, excavating impact craters and destroying themselves in the process. Meteoroids which encounter an atmosphere may be aerobraked, ablated and/or fragmented by it.

Ablation may completely "burn up" an entering object in a planet's atmosphere. Catastrophic fragmentation may pulverize it, essentially destroying it, and preventing it from cratering the surface. Meteoroids that manage to reach the surface may produce craters considerably diminished in size, compared to those they would have formed in the absence of an atmosphere, due to reductions in their impact masses and speeds (i.e., their impact energies) caused by ablation and drag deceleration. The combined effects of ablation and drag may reduce a meteoroid's speed so much that upon reaching the surface it "soft-lands", survives impact, becomes a meteorite, and produces little or no crater. Thus, one consequence of the presence of an atmosphere is to generally reduce planetary cratering rates and alter crater population distributions. This phenomenon has previously been investigated on Venus (e.g., Zahnle, 1992; Herrick and Phillips, 1994), Titan (Engel et al., 1995), and Mars (Popova et al., 2003; Chappelow and Sharpton, 2005).

Another result of atmospheric interference with meteoroid impact is the production of meteorites on planetary surfaces. Few, if any, large pieces of impacting bodies are expected to be found on airless bodies such as the Moon, but meteoritic phenomena are well documented and studied on Earth, and have been presumed to occur on Mars as well (e.g., Dycus, 1969; Bland and Smith, 2000). Some of the results of the previous Chapter (Chapter 3) strongly suggest that the current 6 mbar atmosphere of

* Prepared for submission to Icarus, September, 2005.

Mars is sufficient to aerobrake significant numbers of small (< 10 kg) carbonaceous chondrite, stony, and even iron meteoroids into low-velocity (< 500 m s^{-1}) impacts with the surface. Recently, the discovery by the Mars Exploration Rover (MER) Opportunity that Heat Shield Rock is an iron meteorite (http://marsrovers.jpl.nasa.gov/newsroom/pressreleases/20050119a.html), and confirmation that MER Spirit has photographed a meteor streak (Selsis et al., 2005) have established the presence of meteorites on the surface of Mars, and meteors in its atmosphere.

However, martian meteorite production has received relatively little attention. Dycus (1969) and Bland and Smith (2000) provide two rare studies that directly address the subject. A couple of others (Rochelle et al., 1999; Hörz et al., 2004) are aimed primarily at the question of minimum martian crater sizes, and approach the subject of meteorites only incidentally. All of these works generally consider only special cases of martian meteoroid entry, not the general problem.

No previous study considers meteorite production under other than the current martian atmospheric conditions. The martian atmosphere is believed to undergo large, obliquity-driven variations in density (e.g., Bills, 1990; Ward, 1992; James et al., 1992) which may cause the surface pressure to vary between lunar-like conditions of essentially zero mbar and pressures of tens or even hundreds of mbar over timescales of tens to hundreds of kyr. Atmospheric effects on both martian cratering and meteorite production rates may therefore vary with time. Both crater and meteorite populations may hold physical evidence of past variations in the martian atmosphere. Chapter 3 investigates the cratering implications of not only the current martian atmosphere, but of potential past and future ones as well. That work strongly indicates that meteorite production on Mars would increase dramatically under martian atmospheres only slightly denser than at present.

In Chapter 3 I explored the impact cratering effects of large populations of martian impactors over a very broad range of masses (10^{-1} kg - 10^{7} kg). In that study I was confronted by the need to simulate the atmospheric passage of statistically significant

numbers of objects of all masses within the stated range, yet retain the proportions specified by a realistic meteoroid mass-frequency distribution (MFD), given by

$$N_m(m_o) = \alpha \cdot m_o^{-1.27}, \tag{4.1}$$

(see Chapter 3) where N_m is the number of objects in the population more massive than m_o, α is an arbitrary constant and the subscript indicates initial (entry) values. Since this MFD requires, for example, that there be over 10 billion objects larger than 0.1 kg for every one larger than 10^6 kg in the population, it was computationally unfeasible to simulate the full required number of atmospheric passages.

My solution to this problem was to divide the mass-range into a manageable number of bins, each associated with a "weight-factor" consistent with the meteoroid MFD (Eq. 4.1) and each represented by its central mass value, a process which effectively discretizes the mass variable. Small (n = 2000) sub-populations of martian impactors, each corresponding to a mass-bin, were then generated; these, when multiplied by their associated weight factors and added together, form the complete impactor population of interest.

Here I expand this method to include all three parameters which describe the initial conditions of entering meteoroids (entry mass, m_o, entry velocity, v_o, and entry-angle, θ_o) in the discretization. In this case these three parameters may be conveniently viewed as the coordinates of a mathematical 3-space. Any given set of entry parameters is simply a point in this parameter space and the "bins" are actually 3-d rectangular cubes in the same space. The center point of each of these cubical bins (m_c, v_c, θ_c) then represents a small 3-dimensional range of possible Mars-incident meteoroids.

By creating a simulation of martian atmospheric passage and "scanning" it over a grid of points in parameter space, two things are accomplished. First, I can calculate the fractions of large populations of Mars-incident meteoroids (henceforth called "impactors", even if they do not actually impact the martian surface) that share certain outcomes. The fraction of the population that become martian meteorites is calculated by simply adding together the normalized weight factors of all the objects determined by the

atmospheric passage simulation to have soft-landed on the surface. The result is the fraction of the real population that can be expected to become meteorites. By varying the density of the martian atmosphere I can examine the dependence of meteorite production rates on martian atmospheric variations.

The resulting set of martian impactor outcomes vs. entry parameters can be used to answer questions such as: What ranges of entry parameters may result in meteorites on Mars? What ranges could produce the iron meteorite Heat Shield Rock? How do these ranges depend upon Mars's atmospheric density? What are the other possible fates of objects that enter Mars's atmosphere? These and other questions are addressed in this chapter. A secondary goal is to compare my results to existing works in this field and, if possible, use them to provide context for these previous works.

4.2 METHODS

A set of 3-d "bins" was set up in (m,v,θ) parameter-space by defining their boundaries and centerpoints (m_c,v_c,θ_c); these were chosen to cover pre-determined ranges of interest in each of the variables as densely as possible. Each bin was assigned a weight factor based on probability functions defined over each parameter. A computer program that uses a 4th order Runge-Kutta routine to integrate the equations of meteoritic flight in an atmosphere (see the Appendix to this thesis) was placed inside a loop which scans it through the 3-d grid of initial values (m_c,v_c,θ_c). Each integration was halted when the object being simulated burned up, impacted the surface, or escaped the planet. The results and weight factors were used to assemble 'virtual' populations of martian impactors. This entire process was repeated for martian atmospheres of 2, 6, 20, and 60 mbar of surface pressure and for each of two types of meteoroids: stones (ordinary chondrites) and irons (Table 2).

4.2.1 Setting up the bins and weight factors

Each bin represents a range of impactor initial masses, velocities and entry-angles with a single "test impactor" of initial values (m_c,v_c,θ_c). Therefore the smaller the bin size, the better the simulation of the test particle's passage through the atmosphere will

characterize the dynamics and fates of all other possible meteoroids in the same bin. However, since each bin also represents a time-consuming run of the computer simulation, the number of bins must be kept to a minimum, at the same time. Bin organization is dictated by these two competing factors, as well as by the parameter ranges of interest.

The meteoroid mass-range of interest in this study is 1 kg $\leq m_o \leq 10^9$ kg, selected because it covers all masses capable of producing meteorites more massive than 1 kg on Mars: 1 kg objects cannot soft-land with $m_{final} \geq 1$ kg, while 10^9 kg ones have no hope of soft-landing at all. Since this mass-range covers several orders of magnitude, it is broken down into mass-bins based on a log scale, instead of constant-width bins, the same way it was done in Chapter 3. Here bin centers are defined by $m_{c,i} = 10^{(i-1)/2}$ kg (i = 1,2 . . .18,19), with each bin's boundaries given by $m_{i-} = 10^{(i-1)/2-1/4}$ kg and $m_{i+} = 10^{(i-1)/2+1/4}$ kg.

Since N_m in Eq. 4.1 represents the number of objects in a population that are more massive than m_o, the number that actually fall between two bounds (e.g., bin-boundaries) is

$$N_{bin} = N_m(m_-) - N_m(m_+).$$

The probability that any given object out of the total population will fall within a given mass-bin is then

$$P_m = \frac{N_m(m_-) - N_m(m_+)}{N_{tot}}.$$

Substituting for N_m using Eq. 4.1

$$P_m = \frac{\alpha}{N_{tot}}\left(m_-^{-1.27} - m_+^{-1.27}\right), \tag{4.2}$$

where N_{tot} is the total number of objects in the population. Eq. 4.2 is henceforth referred to as the mass-probability-function.

The velocity-range of interest for asteroidal types of objects incident on Mars is about 6 km $s^{-1} \leq v_o \leq 32$ km s^{-1} (see Chapter 3), which I break down into 13 evenly

spaced, constant-size velocity-bins, 2 km s^{-1} wide and centered at v_o = 7, 9, 11 . . . 29, 31 km s^{-1}. The velocity-probability-function is essentially the same as that used in Chapter 3, i.e.,

$$P_v = A_v \exp\left(-(v_o - 7)^2 / 64\right) \cdot \frac{\Delta v}{v_{range}}, \tag{4.3}$$

where 6 km $s^{-1} < v_o < 32$ km s^{-1}, Δv, the bin-width, is constant, v_{range} is the velocity range of interest, and A_v is a normalization constant. This function has a maximum at v_o = 7 km s^{-1} and a 3σ width of 24 km s^{-1}.

The cumulative form of the generally accepted entry-angle probability distribution is $P_\theta^{cum} = A_\theta \cos^2\theta$ (Gilbert, 1893; Shoemaker, 1962), where P_θ^{cum} is the probability that any given meteoroid will enter Mars's atmosphere at an angle steeper than θ (measured from horizontal). Thus, the probability of any meteoroid falling within an entry-angle bin defined by upper and lower limits θ_+ and θ_- is

$$P_\theta = A_\theta \left(\cos^2\theta_- - \cos^2\theta_+\right), \tag{4.4}$$

where A_θ is another normalization constant. Eq. 4.4 is the entry-angle probability function.

Discretization of the entry-angle is considerably more involved than in the cases of velocity or mass. Preliminary runs of my atmospheric passage program demonstrated that the dynamics of very shallow entering impactors depend quite sensitively on the entry-angle and suggested that entry-angle bins of as little as 0.1° would be needed to capture the details of how entry-angle affects eventual outcome. This is especially important in the cases of the low density (2 and 6 mbar) atmospheres which only produce meteorites over very narrow ranges of very shallow entry-angles.

Fortunately the results are much less sensitive for impactors that enter the atmosphere at other angles, so much larger bin sizes can be used. To take advantage of this I used different size bins in different sub-ranges of entry-angle. After some experimentation I arrived at an entry-angle binning scheme that can be used for all of the

Mars atmospheres considered here (Table 4.1). In plotting the results, the smallest bins (0.1° and 1.0°) were combined into larger sizes (1.0° and 3.0°) for convenience and clarity.

Finally, the total weight factor associated with each 3-d bin (characterized by entry values $m_{o,i}$, $v_{o,j}$, and $\theta_{o,k}$) is the product of the probability functions,

$$W_{ijk} = P_m(m_{o,i}) \cdot P_v(v_{o,j}) \cdot P_\theta(\theta_{o,k}). \tag{4.5}$$

This number represents the probability that any given meteoroid encountering Mars, and falling within the mass, velocity and entry-angle ranges of interest defined above, will fall within the bounds of bin (i,j,k).

4.2.2 Simulation of atmospheric passage

The purpose of the atmospheric passage simulation is to determine the fate of a martian impactor, given its physical properties, the properties of the atmosphere it is entering, and its mass, velocity and trajectory angle at entry. Besides the fate of the object (discussed below), outputs include the final mass, velocity and trajectory angle.

The model used in the present study is almost the same as that used in Chapter 3. Two major differences are:

(1) The procedure used here does not make use of the "flat-Mars" approximation. The full set of meteor-flight equations of motion integrated here is therefore

$$dv/dt = -C_D \frac{\rho_{atm} A}{2m} \cdot v^2 + g_o \sin\theta, \tag{4.6a}$$

$$dm/dt = -C_H \frac{\rho_{atm} A}{2Q} \cdot v^3, \tag{4.6b}$$

$$d\theta/dt = \frac{g_o \cos\theta}{v} - \frac{v \cos\theta}{R+z}, \tag{4.6c}$$

where m, v, z and A are the projectile's instantaneous mass, velocity, altitude and cross-sectional area, respectively, θ is its trajectory angle (measured from local horizontal, positive-downward), R and g_o are Mars's radius and surface gravity, Q is the projectile's

heat of ablation, ρ_{atm} is the local atmospheric density, and C_D and C_H are the drag and heat transfer coefficients. The last term in Eq. 4.6c accounts for Mars's curvature.

(2) A further-improved approximation of the heat transfer coefficient is used, which includes its dependence on ambient atmospheric density. The results of Bibermann et al. (1980), upon which $C_H(v)$ in Chapter 3 was based, are given in terms of object velocity and altitude in Earth's atmosphere. The data were translated to the form $C_H = C_H(v,P_{atm}(z))$ and put into tabular form; in my computer program, C_H is obtained during every time-step by interpolation on this look-up table of $C_H(v,P_{atm})$ (see the Appendix to this thesis). The drag coefficient is still considered constant and equal to 1.

4.2.3 The martian atmosphere

The martian atmosphere is modelled here exactly as in Chapter 3. An exponential atmosphere, $P_{atm}(z)$, is defined by a fixed scale height (10,900 m) and a surface pressure value. The atmosphere is varied by changing the surface pressure. The atmospheric density profile, $\rho_{atm}(z)$, is calculated from $P_{atm}(z)$ using the Ideal Gas Law.

4.2.4 Impactor outcomes

For each 3-d bin in parameter space, a test impactor is run through the atmospheric passage simulation until one of the following occurs (numbers refer to Fig. 4.1): the impactor (1) burns up ($m \leq 0$), (2,3) hits the surface ($z \leq 0$), or (4) "skips out" of the atmosphere ($z \geq 200$ km). Whether an object that hits the surface is destroyed (2) or survives as a meteorite (3) is determined by a threshold velocity. This method is rather artificial, since in reality there is no sharp velocity-dividing-line between meteorite survival and hard-impact destruction, but there are no simple alternatives. Setting a value for the threshold is somewhat problematic, since projectile survivability is another subject which has not been extensively investigated.

Hörz et al. (1984) found that 1 g stainless steel spheres fired vertically into a regolith simulant at 1.35 km s^{-1} survived almost undamaged. Bland et al. (2001) found that 4 mm diameter by 5 mm long samples of iron meteorite also survived impact into simulants, deformed but whole, up to velocities of at least 1.8 km s^{-1}, while similar samples of stony materials were shattered by impact speeds as low as 1.4 km s^{-1}.

However, these experiments were conducted at normal incidence angles; Gault and Wedekind (1978) found that oblique impact angles promoted the survivability of aluminum projectiles fired into quartz sand. Based on these facts, and with Eq. 4.4 in mind (i.e., that most impacts occur at oblique angles), I adopted estimates of v_{thresh} = 1.5 km s^{-1} for stony objects, and v_{thresh} = 2.0 km s^{-1} for iron ones.

With these numbers established, Mars's atmospheric density sets a theoretical upper limit, m_{max}, on the masses of objects that can be decelerated to low enough speeds to become meteorites. Objects whose terminal velocities exceed v_{thresh} cannot possibly impact the surface slowly enough to survive. Note, for example, that Mars's current atmosphere cannot decelerate stones or irons more massive than ~10^4 kg sufficiently to meet the criteria for soft-landing adopted above (Fig. 4.2a,b). Figure 4.3 displays the dependence of m_{max} on atmospheric surface pressure.

After initially descending in altitude, some meteoroids which enter at very shallow angles later regain altitude as the planet curves away below them (Fig. 4.4). Whether these objects ultimately escape back into interplanetary space (a) or fall back to a terminal encounter with Mars (b), depends on how strongly they are affected by aerobraking and ablation as they pass through the atmosphere. For my purposes, objects that pass an altitude of 200 km are deemed to have "skipped-out" of the atmosphere and escaped Mars. While, strictly speaking, skip-outs whose velocities are less than escape velocity must eventually re-enter the atmosphere, test runs of my procedures indicated that these are very few in number, and they would still have to survive passage through the entire atmosphere to reach the surface. Therefore they are neglected, which avoids the need to integrate their time-consuming trajectories.

Projectiles that gain altitude, but do not reach 200 km altitude, eventually fall back toward the surface. Ones that then soft-land (b, Fig. 4.4) are singled out by my program, and termed "near skip-out" meteorites, to differentiate them from "direct meteorites" (c). Meteorites like these are kept track of, because they may contribute disproportionately to meteorite production under the thinner (2, 6 mbar) atmospheres

studied here, since their atmospheric paths can be many times longer than those of direct meteorites.

The last possible outcome shown on Fig. 4.1, aerial fragmentation (5), is not considered in this study because it is very difficult and computer-time intensive to treat, and because the results of Chapter 3 indicate that exceedingly few stony or iron objects break up in even a 60 mbar Mars atmosphere. However, Chapter 3 also indicates that significant numbers of carbonaceous chondrites do fragment, which is why they are not included in the present study. It should be noted, however, that their low densities, high heats of ablation, and relative abundance compared to stone and iron meteoroids (Table 4.2), make them excellent candidates to become martian meteorites, a conclusion which is supported by the results of Chapter 3.

4.3 RESULTS

I performed the procedures described above for two martian impactor types, stony and iron (Table 4.2), and for four different martian atmospheres: 2, 6, 20 and 60 mbar of atmospheric surface pressure. Table 4.3 displays the fractions of statistically large, realistic (i.e., which follow Eq. 4.1) populations of 1 kg $\leq m_o \leq 10^9$ kg stones and irons that meet each possible fate. In general, I found that production of both stony and iron martian meteorites increases by roughly an order of magnitude for each ~3-fold increase in atmospheric surface pressure from 2 mbar to 6 mbar to 20 mbar, until it saturates for the 60 mbar atmosphere. Thus variations in the martian atmosphere, well within the limits postulated by recent work (e.g., Vasavada et al., 1993; Popova et al., 2003; Nakamura and Tajika, 2003), may have profound effects on rates of meteorite accumulation on Mars.

The vast majority of both iron and stone impactors reach Mars's surface where they either hard-impact or soft-land, depending upon their impact velocities. Objects more massive than ~10^5 kg are largely unaffected by Mars's atmosphere (Figs. 4.5), except that the sizes of craters they form may be reduced (see Chapter 3). However, such large objects make up only very small fractions (~10^{-6}) of the populations of interest. For

smaller objects, which outcome (hard-impact or soft landing) dominates depends strongly on the atmosphere they encounter. The 2 mbar atmosphere decelerates fewer than 1% of stony and iron impactors into landing as meteorites (Table 4.3). These are limited to the smallest (Figs. 4.5a,e) and, apart from skip-outs, shallowest-entering (Figs. 4.6a,e) projectiles, with entry angles between 9° and 13° and masses less than 10 kg. More than one-quarter of the meteorites produced by the 2 mbar atmosphere, and 5-10% of those landed by the 6 mbar atmosphere follow near skip-out type trajectories (see (b) Fig. 4.4, and Table 4.3), making them significant contributors to meteorite production under the low-density (2 and 6 mbar) atmospheres.

Denser atmospheres are more effective at slowing impactors down, thus the numbers of impactors that end up as meteorites increase dramatically as atmospheric density increases, and the numbers that hard-impact drop. Unlike under the low-density atmospheres, meteorite production is not limited to a narrow range of shallow entry-angles (e.g. compare Figs. 4.6a,b to Figs. 4.6c,d). Under the thickest, 60 mbar, atmosphere, approximately 97% of both stones and irons (1 kg $\leq m_o \leq 10^9$ kg) soft-land including significant fractions of impactors up to 10^4 kg mass (Figs. 4.5d,h). The remainder consist almost entirely of objects more massive than 100 kg which either skip out of the atmosphere if their entry-angle is low enough ($\theta_o \leq 8°$; see Figs. 4.6d,h) or punch through it to hard-impact if their entry-angles are steeper. A very few, with entry velocities greater than about 24 km s^{-1}, burn up instead (Figs. 4.7d,h).

The fraction of near skip-out meteorites seems to be essentially independent of object type or atmosphere (Figs. 4.8, Table 4.3). Skip-outs decrease steadily with increasing atmospheric density, but near skip-outs remain virtually constant (compare Figs. 4.8a and 4.8b). Since the total numbers of meteorites increases dramatically with increasing atmospheric density, near skip-outs contribute a much larger fraction of the total for the low-density atmospheres than they do for higher density ones. In all cases, near-skipout occurs only for impactors entering within a narrow 3°- 4°-wide "corridor" of entry angles, somewhere within the range $7° < \theta_o < 14°$, depending upon the atmosphere in question (Figs. 4.8).

Under all four of the martian atmospheres studied, only very small numbers of impactors burn up in, or skip out of, the atmosphere. Because of this, impact cratering and meteorite production may be viewed as complimentary processes, strongly tied to the state of Mars's climate; as the atmosphere varies, losses in one process approximately equal gains in the other. During periods of thin atmosphere, impact cratering would dominate, while periods of denser atmosphere would feature much more meteorite accumulation.

Examination of the results demonstrates that only the smallest (Figs. 4.5) and fastest (Figs. 4.7) impactors burn up, and that the number that burn up is fairly independent of entry angle (Figs. 4.6). Practically no impactors with entry velocities of less than 22 km s^{-1} were found to burn up. Burnups peak for an atmosphere of about 6 mbar for stony objects and between 6 mbar and 20 mbar for irons. Martian atmospheres in this range have just the right density to ablate these objects without decelerating them too quickly (ablation rate is proportional to v^3 (Eq. 4.6b) so ablation drops off rapidly with speed). Thinner atmospheres (e.g. 2 mbar) do not ablate small impactors quickly enough to completely vaporize them before they hard-impact, while denser ones (e.g. 60 mbar) decelerate them rapidly to low velocities, resulting in meteorites.

4.3.1 Comparisons with other work

Separate runs of my procedures were performed for the purpose of comparing the results with those of the two previous studies of the potential for meteorites on Mars mentioned above. Both of these studies consider only the special case of stony meteoroids entering the current ~6 mbar martian atmosphere vertically (Table 4.4).

Dycus (1969) used a simple Euler's method numerical routine to approximate the dynamics of 10^{-2} kg - 10^{7} kg meteoroids entering Mars's atmosphere at 8.2 km s^{-1}. According to my classification system, Dycus's 0.010 kg and 0.032 kg impactors result in small meteorites, while all larger ones hard-impact on the surface. Table 4.5 shows that my results agree well with Dycus only at the large end of the mass range; this is because Mars's atmosphere has very little effect on such massive objects. For smaller masses,

which ablation and aerobraking affect much more strongly (see Chapter 3), my results disagree sharply.

This disagreement is definitely due to the very high value of the heat transfer coefficient (C_H = 0.4) used by Dycus, compared to values generally accepted today, and compared to the parameterized C_H I used (Fig. 4.9), which is based on Bibermann et al. (1980). This C_H has values less than 0.01, for velocities less than 10 km s^{-1} and gas densities found in a 6 mbar atmosphere. Because of this, I observe far less ablation and deceleration of the impactors than is reflected in Dycus's results and I find that none of the objects simulated come close to landing as meteorites. All of them hard-impact, and crater the surface (Table 4.5).

Bland and Smith (2000) used a semi-analytical approach to estimate the percentages of small (10s-of-grams) impactors that arrive at Mars's surface slow enough to survive impact. Their treatment allows for the full range of reasonable entry velocities, but only vertical entry. They consider two different values of the "ablation parameter", σ, which correspond to values of C_H of 0.05 and 0.20 (assuming a heat of ablation of 5 MJ kg^{-1} for stony material), and several values for the maximum impact survival velocity of stony meteorites, v_{thresh}, including v_{thresh} = 1.6 km s^{-1}, which is close to the value I use. The value C_H = 0.05 is close to the mean value of my parameterized $C_H(v,P_{atm})$ for the velocity range of interest (Fig. 4.9), though of course it lacks the variation with velocity my C_H features.

Figure 4.10 displays a comparison of the results of the present study with those of Bland and Smith (2000) for the case C_H = 0.05, v_{thresh} = 1.6 km s^{-1}. When the entry-angle is limited to 90°, the two sets of results agree very well. The systematic difference that occurs is likely due to the differences in treatment of C_H and the slightly different values of v_{thresh} used. This agreement of these two quite different methods provides some measure of confidence that the methods are consistent with each other.

Bland and Smith mention that limiting the entry angle to vertical probably yields conservative results, and I found that this is quite the case (Fig 4.10). The narrow range of masses that Bland and Smith found to produce 0.01+ kg meteorites also appears to be

a product of this limitation. When all entry-angles are included and my procedure re-run, the percentages of 0.01+ kg meteorites produced increase significantly, and are not limited to the $0.02 \leq m_o \leq 0.05$ kg range found by Bland and Smith, but extend all the way up to about m_o=100 kg (see Fig. 4.5b). This indicates that 90° is not the most favorable entry-angle for producing meteorites from these sizes of meteoroids.

In fact, I found that shallow entry-angles ($\sim 10^\circ < \theta_o < 30^\circ$) are the most effective at producing meteorites out of impactors in the 10s-of-grams range and that near-vertical is actually the least efficient mode of entry (Fig. 4.11). This observation is consistent with my results for the more massive stony impactors of interest in this study (e.g. Fig. 4.6b). When this observation is combined with the entry-angle probability distribution (Eq. 4.4), it turns out that angles in the range of 40°- 45° are the most meteorite-productive for 10s-of-grams meteoroids.

4.3.2 Heat Shield Rock

The discovery in Terra Meridiani, Mars by the rover Opportunity, that "Heat Shield Rock" (HSR) is in fact an iron meteorite led to some speculation that its presence implies that Mars must have had a denser atmosphere when it landed. However, to date no quantitative evidence either supporting or refuting this theory has been presented.

The description of HSR as "basketball-sized" (http://marsrovers.jpl.nasa.gov/newsroom/pressreleases/20050119a.html) implies that it has a diameter of about 0.12 m and mass of about 50 kg. Its exterior is covered with features consistent with surface ablation during high speed passage through an atmosphere (e.g., ablation concavities), and none suggestive that it is a fragment of a larger object that broke up in the atmosphere or upon impact (e.g., planar and angular features). The results of Chapter 3 also strongly suggest that aerial fragmentation is quite unlikely. Thus, in what follows, HSR is assumed to have been a single incident meteoroid which was aerobraked to soft-landing on Mars, and which did not fragment upon impact.

To investigate the conditions that turned out HSR, I used my results to narrow down the ranges of entry conditions that an impactor must have to be a potential HSR, for each atmosphere of interest. I repeated my simulation procedures over these new ranges

(at higher resolution), and sorted the HSR-like meteorites (40 kg ≤ m_{final} ≤ 60 kg) out of the results; their statistics are summarized on Table 4.6.

In order for sufficient aerobraking to occur in Mars's atmosphere to decelerate an HSR-mass iron object from more than 6 km s^{-1} to less than 2 km s^{-1}, a certain amount of ablation must also occur. This results in a lower limit to the entry mass HSR must have had at around 60-70 kg, for atmospheres of 6+ mbar (Table 4.6). Thus HSR must have been strongly ablated by passing through a lot of martian atmosphere at high speed, which accounts for the fact that potential HSRs are confined to narrow ranges of shallow entry angles and to relatively high entry velocities.

To become HSR-like, larger objects must lose more mass to ablation than smaller ones, and must therefore have higher entry velocities as well as higher masses. Thus the probability of an impactor landing as an HSR diminishes sharply with increasing mass (see Eqs. 4.2 and 4.3) above the lower limit of 60-70 kg. The overwhelming majority (>99.9%) of possible HSRs are less than 1000 kg in mass.

Under the current martian atmosphere, about one in every 20,000 iron impactors more massive than 40 kg, but less than 10^9 kg, becomes an HSR-like meteorite (Table 4.6). For denser atmospheres (20, 60 mbar surface pressure), the fraction of 40+ kg iron impactors that may yield HSRs increases to about 1-in-3500 and 1-in-500, respectively, due to these atmospheres' higher ablation and aerobraking efficiencies. Thus the production rate of HSRs increases by roughly a factor of 6 for each 3-fold increase in atmospheric surface pressure.

Using the same mass, velocity and entry angle resolution as for the 6 mbar atmosphere, the 2 mbar version appears incapable of producing any HSRs, even though terminal velocity for HSR would be only about 1 km s^{-1} (Fig. 4.2b). Indeed, according to my results this atmosphere produces no iron meteorites larger than 10 kg. Thus it appears highly unlikely that Heat Shield Rock could have landed under a martian atmosphere much less dense than today's, but rather is quite likely to have been brought in by an atmosphere denser than today's.

Finally, almost all of these prospective HSRs hit the surface at very shallow impact angles (Table 4.6), so it is quite possible they could survive impact at speeds somewhat higher than 2 km s^{-1} (Gault and Wedekind, 1978). This also makes it quite likely that Heat Shield Rock ricocheted when it impacted and does not currently rest where it struck the surface. Therefore, even if Heat Shield Rock landed very recently, the absence of a small ($D < 1$ m) impact pit or structure near it should not be surprising.

4.4 CONCLUSIONS

The vast majority of 1 kg $\leq m_o \leq 10^9$ kg stony and iron meteoroids that enter the martian atmosphere reach its surface; very few burn up. Whether they soft-land as meteorites or destroy themselves in hard-impact depends very strongly on the density of the atmosphere they encounter. Under low-density atmospheric conditions (surface pressure = 2, 6 mbar) more than 90% hard impact; only a few percent become meteorites under the 6 mbar atmosphere, and less than 1% do so under the 2 mbar atmosphere. For these low-density atmospheres, meteorites are limited to only those stones and irons less than 100 kg in mass, that enter the atmosphere at less than ~22 km s^{-1} and shallower than 20° but steeper than 7°, (at 100 km altitude). Many of these follow near-skip-out trajectories, making "near skip-outs" a substantial contributor to meteorite production for these atmospheres. This meteorite production would not be detected in any study limited to single, steeper entry-angles, such as 45° or 90°.

About one-half of stones and one-third of irons are slowed to soft-landings by the 20 mbar atmosphere, and more than 95% of each are soft-landed by the 60 mbar atmosphere. The ranges of mass and entry-angle that can result in meteorites are much larger for these atmospheres, reflecting their greater effectiveness at aerobraking and ablating impactors.

My results agree quite well with those of Bland and Smith (2000), for 0.01 kg - 0.15 kg meteoroid masses, when the entry-angle is limited to 90°. When all entry-angles are allowed, however, I find that meteorite production increases considerably, and is not limited to the small range of meteoroid masses found by Bland and Smith (2000). I found

that for 0.01 kg - 0.15 kg meteoroids, shallow ($\sim 10^{\circ} < \theta_o < \sim 30^{\circ}$) entry-angles are much more efficient at delivering meteorites to the surface.

My results do not agree well with those of Dycus (1969). I found far less ablation of martian impactors, probably due to the very high value of the heat tranfer coefficient Dycus adopted.

Heat Shield Rock, the ~50 kg iron meteorite recently discovered on Mars, falls within the purview of this study. My results indicate that HSR is most likely the result of a near skip-out type of event that occurred when Mars's atmosphere was at least as dense as it is today. HSR very probably entered the martian atmosphere at a shallow angle ($10^{\circ} < \theta_o < 25^{\circ}$), high velocity ($v > \sim 15$ km s^{-1}) and between 60 kg and 1000 kg in mass, was strongly ablated during atmospheric passage, and ricocheted on impact. It is highly unlikely that HSR could have been delivered by an atmosphere appreciably less dense than today's 6 mbar atmosphere. The production rate of HSR-like meteorites increases by roughly a factor of 6 for every 3-fold increase in atmospheric surface pressure, up to 60 mbar.

4.5 REFERENCES

Biberman, L. M., Bronin, S. Y., Brykin, M. V. 1980. Moving of a blunt body through the dense atmosphere under conditions of severe aerodynamic heating and ablation. Acta Astronautica 7, 53-65.

Bills, B. G. 1990. The rigid body obliquity history of Mars. J. Geophys. Res. 95, 14137-14153.

Bland, P. A., Artemieva, N. A. 2003. Efficient disruption of small asteroids by Earth's atmosphere. Nature 424, 288-291.

Bland, P. A., Smith, T. B. 2000. Meteorite accumulations on Mars. Icarus 144, 21-26.

Bland, P. A., Cintala, M. J., Hörz, F., Cressey, G. 2001. Survivability of meteorite projectiles-results from impact experiments. Proc. Lunar Planet. Sci. Conf. 32nd, abstract #1764.

Chappelow, J. E., Sharpton, V. L., 2005. Influences of atmospheric variations on Mar's record of small craters, Icarus, in press.

Chyba, C. F., Thomas, P. J., Brookshaw, L., Sagan, C. 1990. Cometary delivery of organic molecules to the early Earth. Science 249, 366-373.

Chyba, C. F., Thomas, P. J., Zahnle, K. J. 1993. The 1908 Tunguska explosion: atmospheric disruption of a stony asteroid. Nature 361, 40-44.

Dycus, R. D. 1969. The meteorite flux at the surface of Mars. Pub. Astron. Soc. Pacific 91, 399-414.

Engel, S., Lunine, J. I., Hartmann, W. K. 1995. Cratering on Titan and implications for Titan's atmospheric history. Planet. Space Sci. 43, 1059-1066.

Gault, D. E., Wedekind, J. A. 1978. Experimental studies of oblique impact, Proc. Lunar Planet. Sci. Conf. 9th, 3843-3875.

Gilbert, G. K. 1893. The Moon's face, a study of the origin of its features. Bull. Philos. Soc. Wash. DC 12, 241-292.

Herrick, R. R., Phillips, R. J. 1994. Effects of the venusian atmosphere on incoming meteoroids and the impact crater population. Icarus 112, 253-281.

Hörz, F., Cintala, M. J., Rochelle, W. C., Mitchell, C. M., Smith, R. N., Dobarco-Otero, J., Finch, B. K., See, T. H. 2004. Atmospheric entry studies and the smallest impact craters on Mars, Proc. Lunar Planet. Sci. Conf. 35th, abstract #1116.

Hörz, F., Cintala, M. J., See, T. H., Cardenas, F., Thompson T. D. 1984. Grain size evolution and fractionation trends in experimental regolith, Proc. Lunar Planet. Sci. Conf. 15th, J. Geophys. Res., 89, Supplement, C183-C196.

James, P. B., Kieffer, H. H., Paige, D. A. 1992. The seasonal cycle of carbon dioxide on Mars. In: Kieffer, H. H., Jakosky, B. M., Snyder, C. W., Matthews, M. S. (eds.), Mars. U. of Arizona Press, Tucson, 934-968.

Nakamura, T., Tajika, E. 2003. Climate change of Mars-like planets due to obliquity variations: implications for Mars. Geophys. Res. Let. 30, 18-1 - 18-4.

Passey, Q. R., Melosh, H. J. 1980. Effects of atmospheric breakup on crater field formation. Icarus 42, 211-233.

Popova, O., Nemtchinov, I., Hartmann, W. K., 2003. Bolides in the present and past martian atmosphere and effects on cratering processes. Meteorit. Planet. Sci. 38, 905-925.

Podolak, M., Pollack, J. B., Reynolds, R. T., 1988. Interactions of planetisimals with protoplanetary atmospheres. Icarus, 73, 163-179.

Rochelle, W. C., Kirk, B., Smith, N., DeVall, M., Hörz, F. 1999. Atmospheric entry and survival of small meteorites on Mars, Proc. Lunar Planet. Sci. Conf. 30th, abst.# 1651.

Selsis, F., Lemmon, M. T., Vaubaillon, J., Bell, J. F., 2005. A martian meteor and its parent comet, Nature 435, 581.

Shoemaker, E. M. 1962. Interpretation of lunar craters. In: Kopal, Z. (ed.), Physics and Astronomy of the Moon, Academic Press, New York, 283-359.

Vasavada, A. R., Milavec, T. J., Paige, D. A. 1993. Microcraters on Mars: Evidence for past climate variations. J. Geophys. Res. 98, 3469-3476.

Ward, W. R. 1992. Long-term orbital and spin dynamics of Mars. In: Kieffer, H. H., Jakosky, B. M., Snyder, C. W., Matthews, M. S. (eds.), Mars. U. of Arizona Press, Tucson, 298-320.

Zahnle, K. J. 1992. Airburst origin of dark shadows on Venus. J. Geophys. Res. 97, 10243-10255.

4.6 TABLES

Table 4.1: Entry-angle bin organization. The 0.1° and 1.0° bins were combined into larger bins in the construction of Figs. 4.6.

Entry angle range	Entry-angle bin size	# of bins	Comments
0.0° - 7.0°	-	0	All impactors in this range 'skip out'.
7.0° - 16.5°	0.1°	95	Outcomes highly sensitive to i.c.s
16.5° - 67.5°	1.0°	51	~ 75% of all objects fall into this range.
67.5° - 82.5°	5.0°	3	Outcomes quite insensitive to i.c.
82.5° - 90.0°	7.5	1	" "

Table 4.2: Physical properties of asteroidal impactors. Physical properties of the three basic types of asteroidal impactors.

Physical Property	Object Type		
	Carbon. Chond.	*Stony*	*Iron*
Density ($kg\ m^{-3}$)	2500.0[4]	3500.0[2,4,5]	7500.0[2,4,5]
Heat of ablation ($kJ\ kg^{-1}$)	3200.0[3]	5000.0[3]	5000.0[1,3]

[1] Passey and Melosh, 1980. [2] Podolak, et al., 1988. [3] Chyba et al., 1990.
[4] Chyba, et al., 1993. [5] Bland and Artemieva, 2003.

Table 4.3: Results for large populations of stony and iron martian impactors encountering different atmospheres. Values are fractions of total population. For example, the fraction of all 1 kg $\leq m \leq 10^9$ kg stony impactors encountering a 6 mbar martian atmosphere that burn up in the atmosphere is 0.0049.

Outcome: / Case:	skip-outs	burnups	hard-impacts	total meteorites	direct meteorite	near skip-out
Stones, 2 mbar	0.0229	0.0014	0.9667	0.0089	0.0064	0.0025
6 mbar	0.0171	0.0049	0.9225	0.0556	0.0531	0.0025
20 mbar	0.0106	0.0017	0.4443	0.5434	0.5408	0.0026
60 mbar	0.0049	0.0008	0.0070	0.9872	0.9849	0.0023
Irons, 2 mbar	0.0256	0.0006	0.9679	0.0059	0.0034	0.0025
6 mbar	0.0198	0.0037	0.9455	0.0310	0.0285	0.0025
20 mbar	0.0134	0.0036	0.6830	0.3000	0.2975	0.0025
60 mbar	0.0074	0.0014	0.0248	0.9664	0.9638	0.0026

Table 4.4: Statistics of two previous studies of martian meteorite production.

	Dycus, 1969	**Bland and Smith, 2000**
Mass ranges:	10^{-2} - 10^{7} kg	$>10^{-2}$ kg
Velocity ranges:	8.2 km s^{-1} only	> 5.0 km s^{-1}
Entry angles:	vertical only	vertical only
Meteoroid types:	stony only	stony only
Atmospheres:	5 mbar only	6 mbar only

Table 4.5: Comparison of results with Dycus (1969). Comparison of results of this work with Dycus (1969).

Entry mass	m_{final} (kg) (Dycus, 1969)	m_{final} (kg) (this study)	v_{final} (km s^{-1}) (Dycus, 1969)	v_{final} (km s^{-1}) (this study)
1×10^{7}	0.996×10^{7}	0.999×10^{7}	8.18	8.23
1×10^{6}	0.991×10^{6}	0.999×10^{6}	8.16	8.21
1×10^{5}	0.981×10^{5}	0.999×10^{5}	8.10	8.18
1×10^{4}	0.960×10^{4}	0.999×10^{4}	8.00	8.11
1000	919.0	998.0	7.77	7.87
100	84.5	99.6	7.28	7.49
31.6	25.1	31.4	6.87	7.21
10.0	7.4	9.94	6.29	6.84
3.16	2.17	3.14	5.49	6.40
1.00	0.64	0.99	4.42	5.44
0.316	0.197	0.313	3.10	4.85
0.100	0.062	0.099	1.66	3.85
0.0316	0.0196	0.0312	0.43	2.68
0.0100	0.0062	0.0099	terminal	1.55

Table 4.6: Heat Shield Rock statistics. The last column is the fraction of 40+ kg iron meteoroids incident on Mars that soft-land ($v_{impact} < 2$ km s^{-1}) with masses between 40 kg and 60 kg.

Atmosphere (mbar)	Minimum initial mass (kg)	Entry velocity range (km s^{-1})	Entry angle range	Maximum impact angle	Fraction HSRs
2	--	--	--	--	zero
6	70	16 - 24	12.7° -13.5°	11.2°	5.03×10^{-5}
20	60	16 - 31	11.7° -13.9°	21.4°	2.97×10^{-4}
60	60	16 - 31	11.0° - 23.0°	43.3°	2.06×10^{-3}

4.7 FIGURES

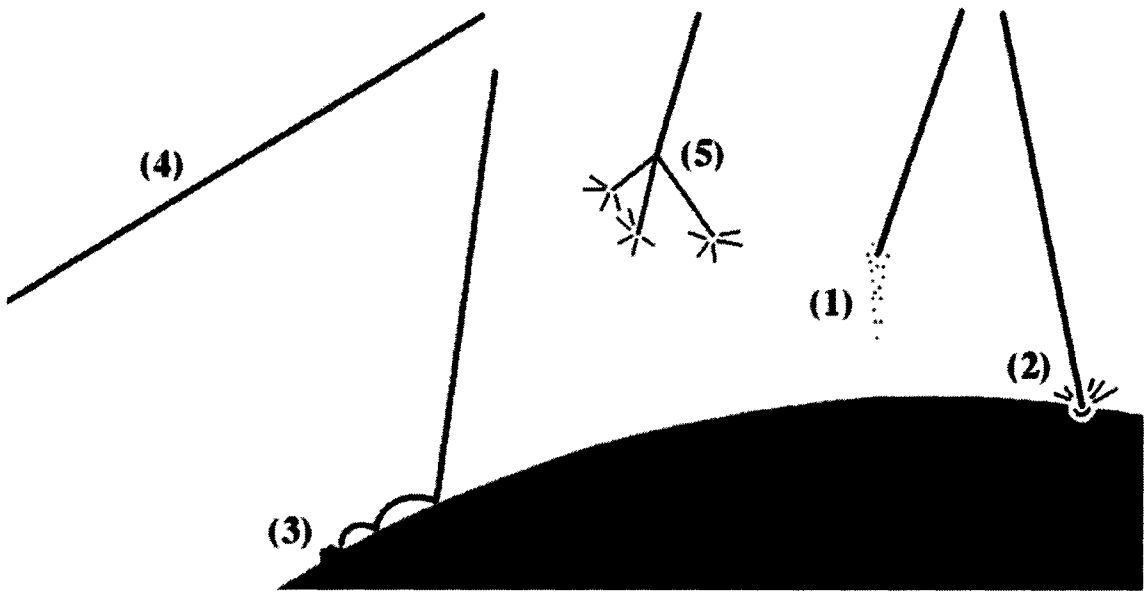

Figure 4.1: Possible outcomes of meteoroidal entry into an atmosphere. Summary of possible outcomes of meteoroidal entry into an atmosphere. (1) atmospheric burnup, (2) hard-impact, (3) soft-landing, (4) skip-out, (5) aerial fragmentation.

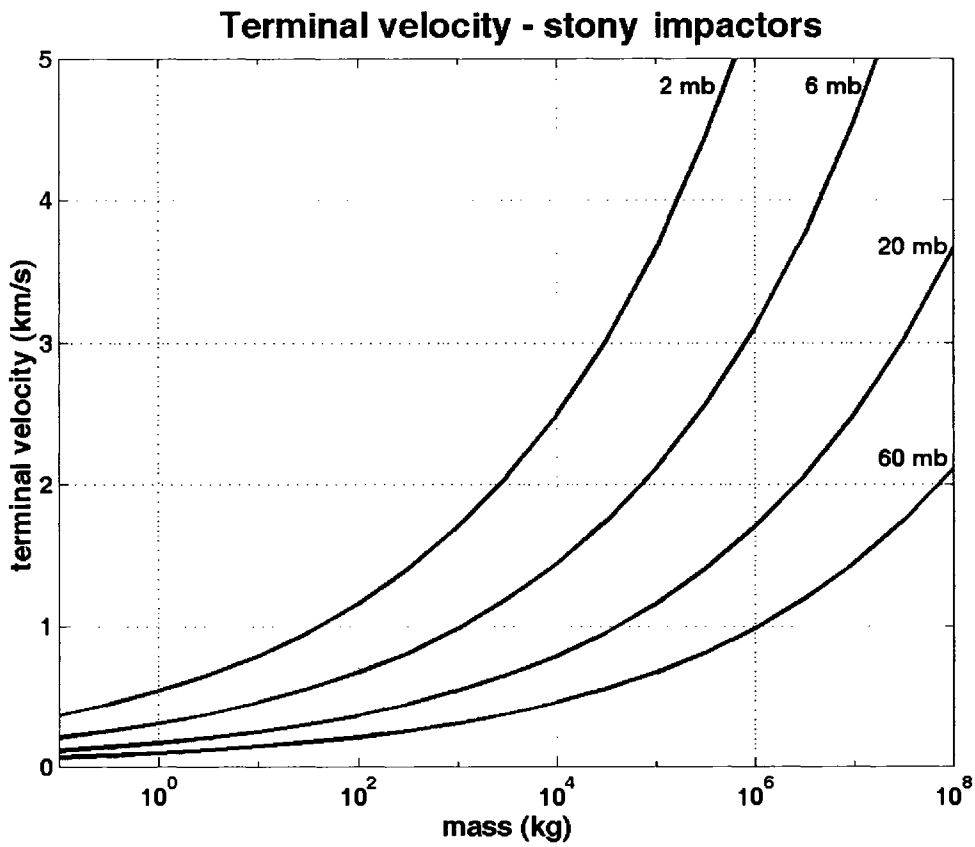

Figure 4.2a: Terminal velocity vs. mass for stony impactors. Terminal velocity vs. object mass for stony impactors, under four different martian atmospheres.

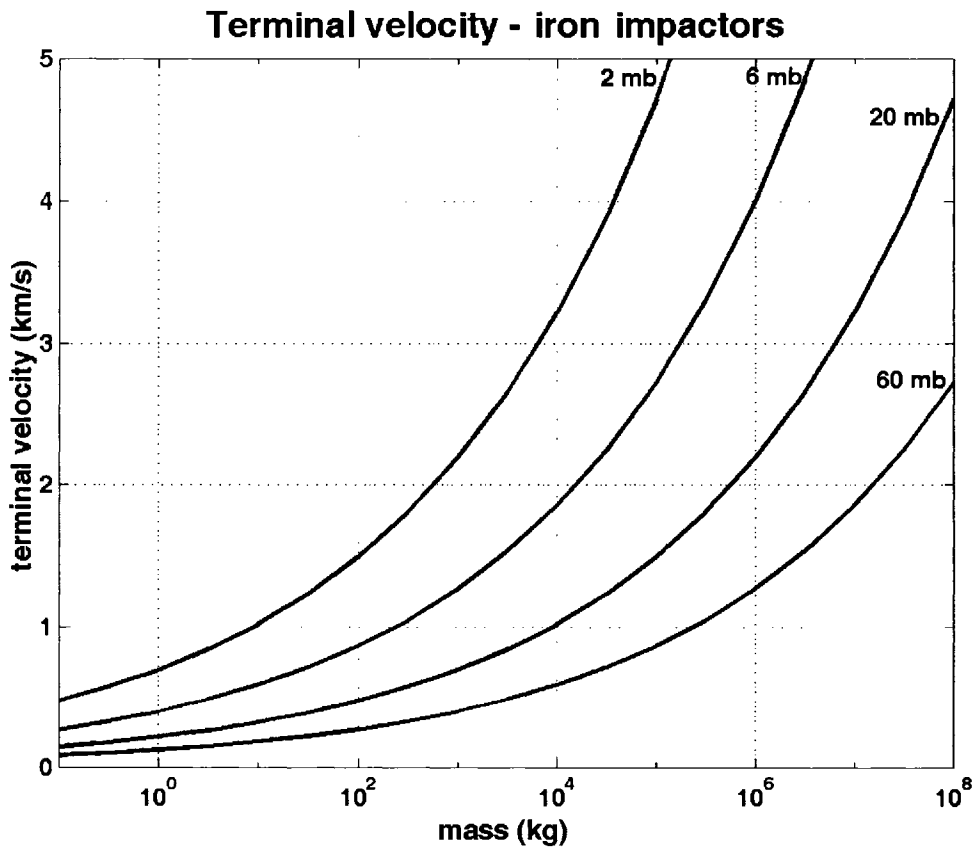

Figure 4.2b: Terminal velocity vs. mass for iron impactors. Terminal velocity vs. object mass for iron impactors, under four different martian atmospheres.

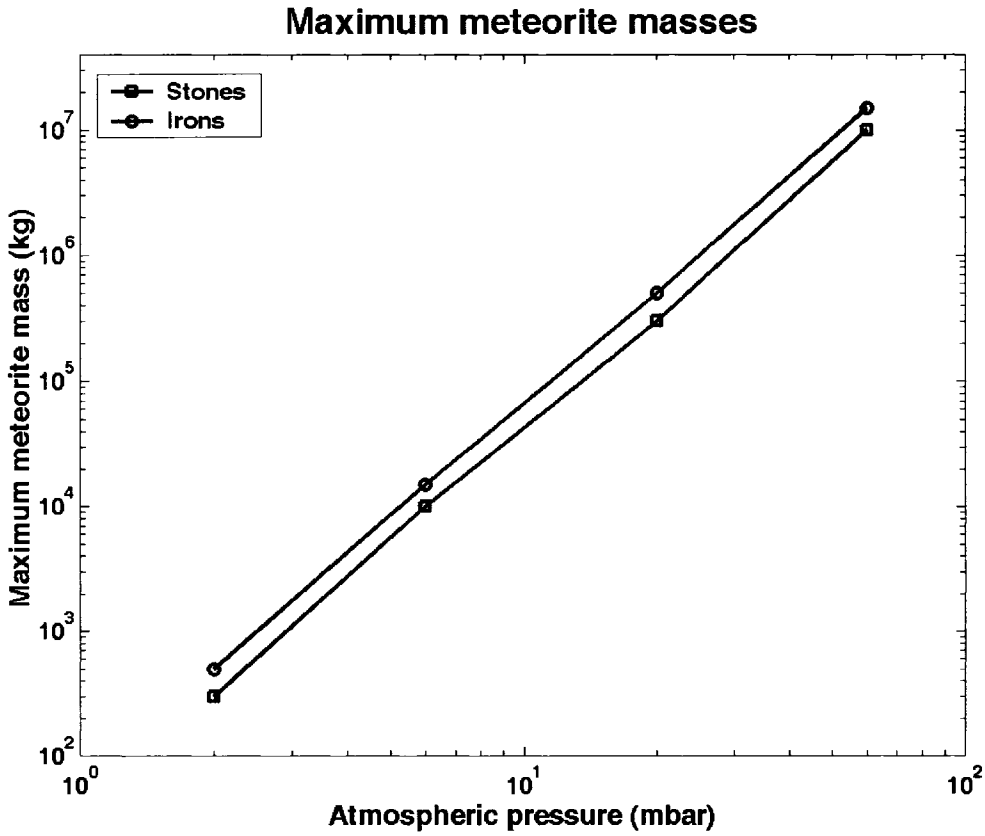

Figure 4.3: Upper limits on meteorite mass vs. martian atmospheric pressure. Theoretical upper limits on meteorite mass vs. martian atmospheric surface pressure. Objects more massive than the curves above have terminal velocities higher than v_{thresh} and therefore cannot be aerobraked sufficiently to survive impact and become meteorites, according to the criteria adopted in this work. Note that under the current 6 mbar martian atmosphere, this puts an upper limit of ~10,000 kg on the masses of both stony and iron meteorites that can theoretically be landed, if slowed to terminal velocity.

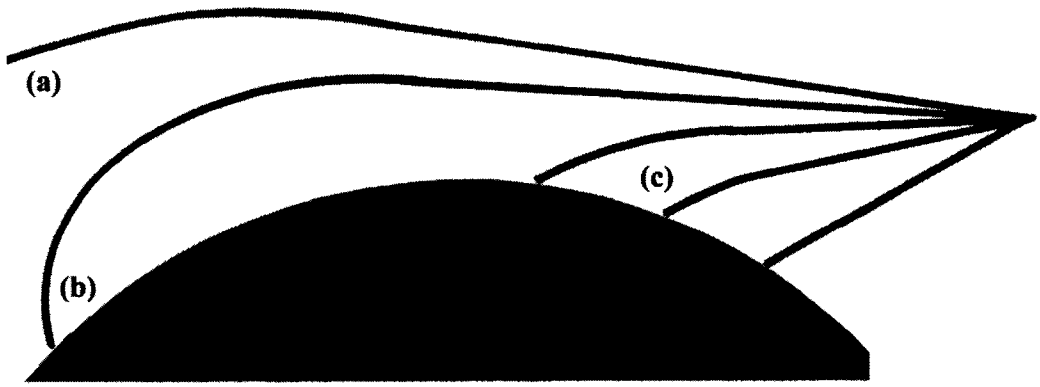

Figure 4.4: Meteoroidal trajectories. Meteoroidal trajectories: (a) atmospheric skip-out, (b) near skip-out, (c) direct entry. Like objects that skip-out, ones on near skip-out trajectories regain altitude after initially descending into Mars's atmosphere, but instead of escaping into space they eventually fall back toward the surface.

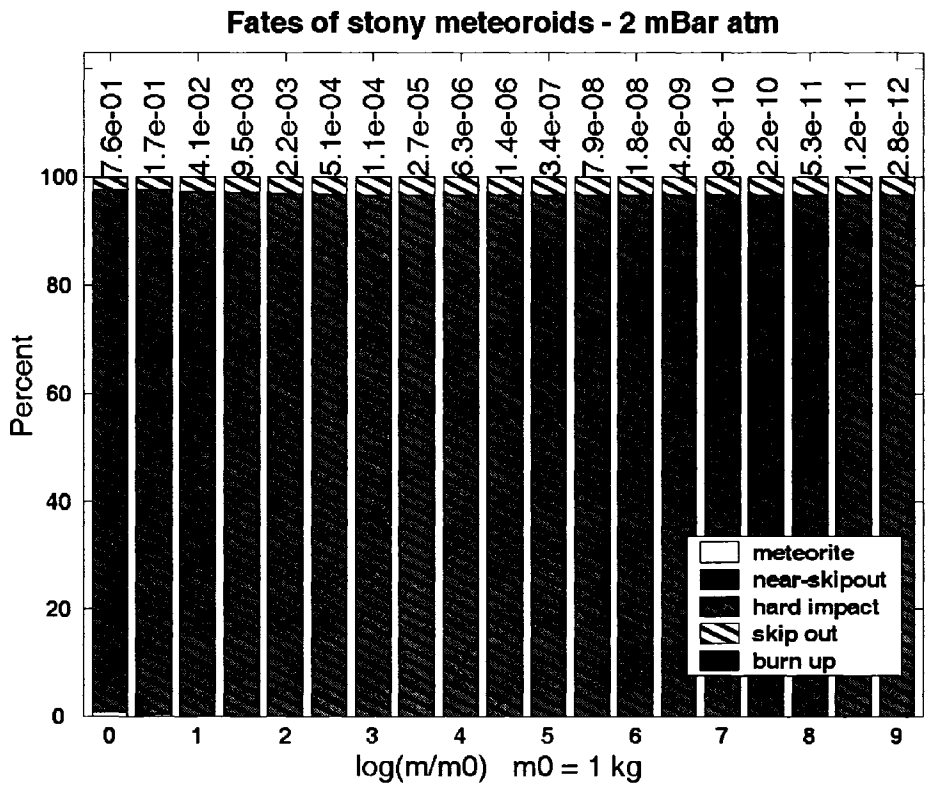

Figure 4.5a: Fates of stony impactors vs. entry mass: 2 mbar atmosphere. Numbers across the top are relative weights of each mass-bin (see Eq. 4.2).

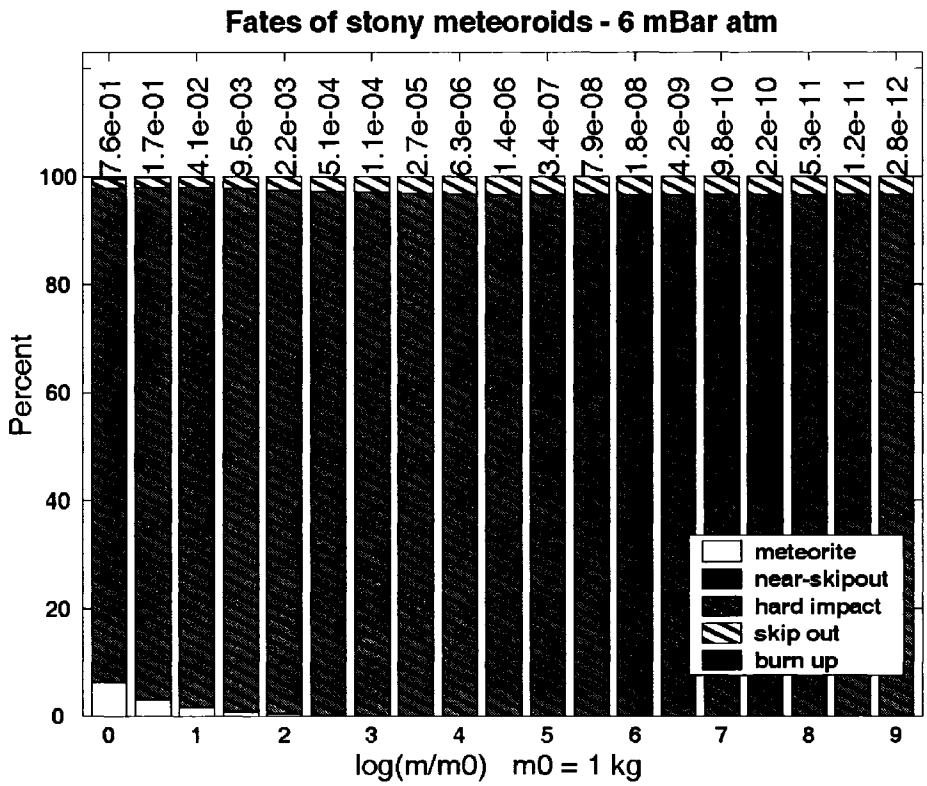

Figure 4.5b: Fates of stony impactors vs. entry mass: 6 mbar atmosphere. Numbers across the top are relative weights of each mass-bin (see Eq. 4.2).

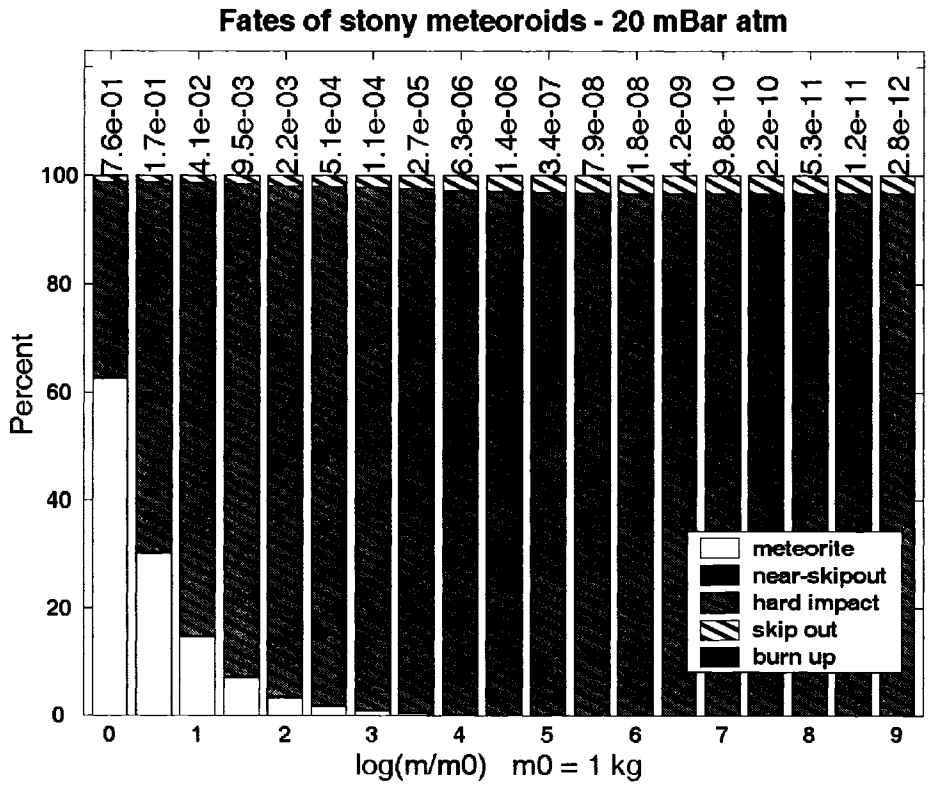

Figure 4.5c: Fates of stony impactors vs. entry mass: 20 mbar atmosphere. Numbers across the top are relative weights of each mass-bin (see Eq. 4.2).

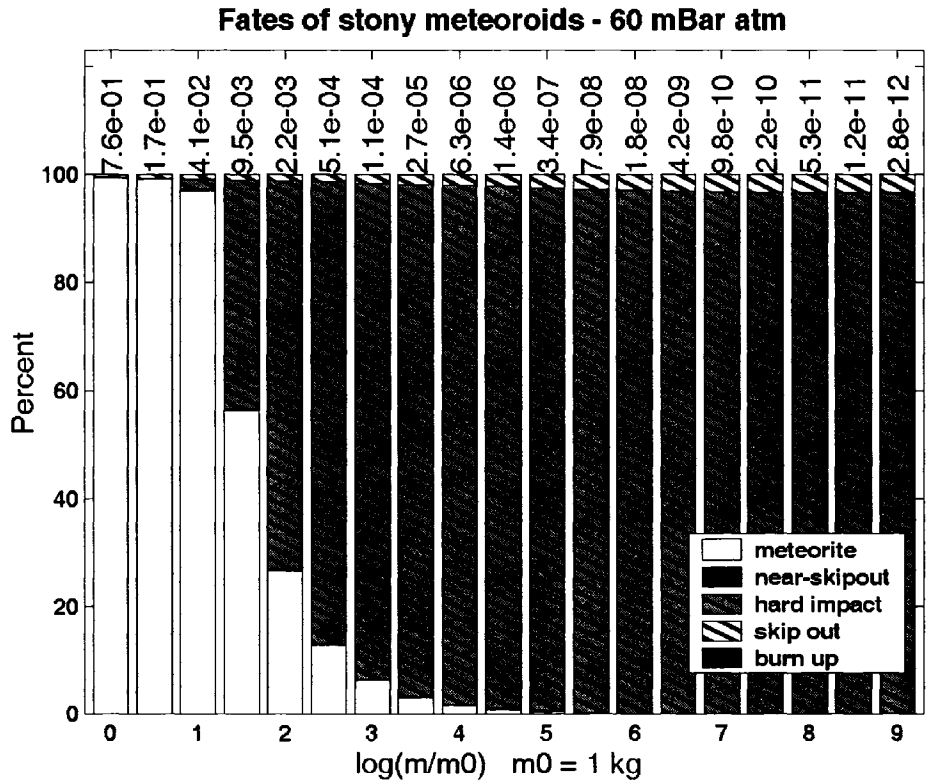

Figure 4.5d: Fates of stony impactors vs. entry mass: 60 mbar atmosphere. Numbers across the top are relative weights of each mass-bin (see Eq. 4.2).

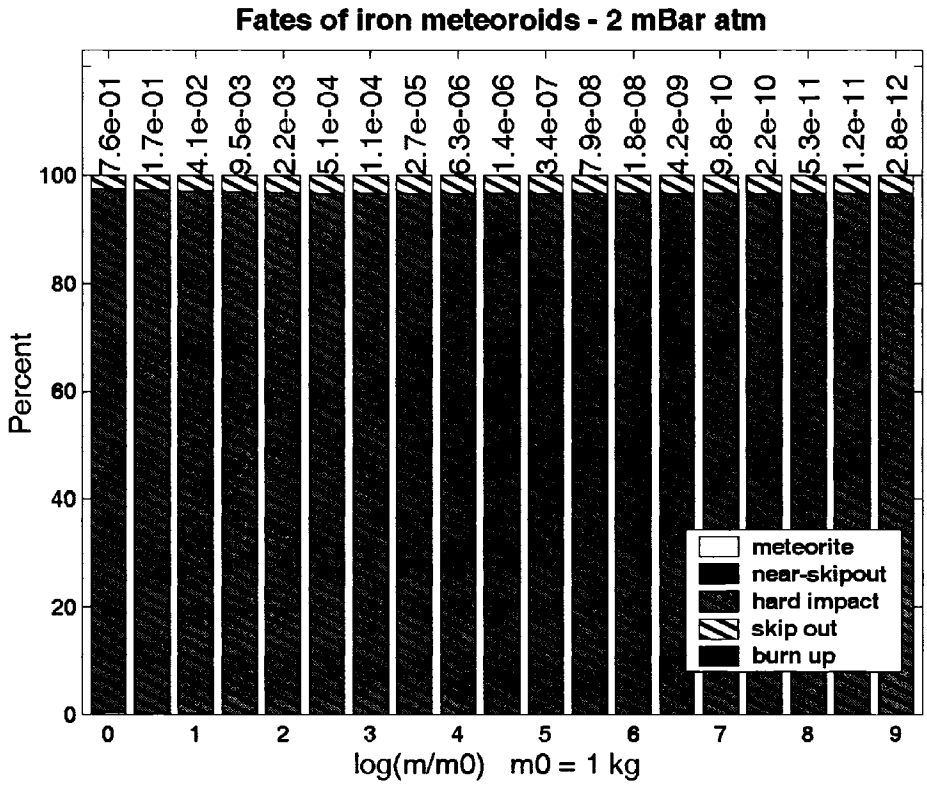

Figure 4.5e: Fates of iron impactors vs. entry mass: 2 mbar atmosphere. Numbers across the top are relative weights of each mass-bin (see Eq. 4.2).

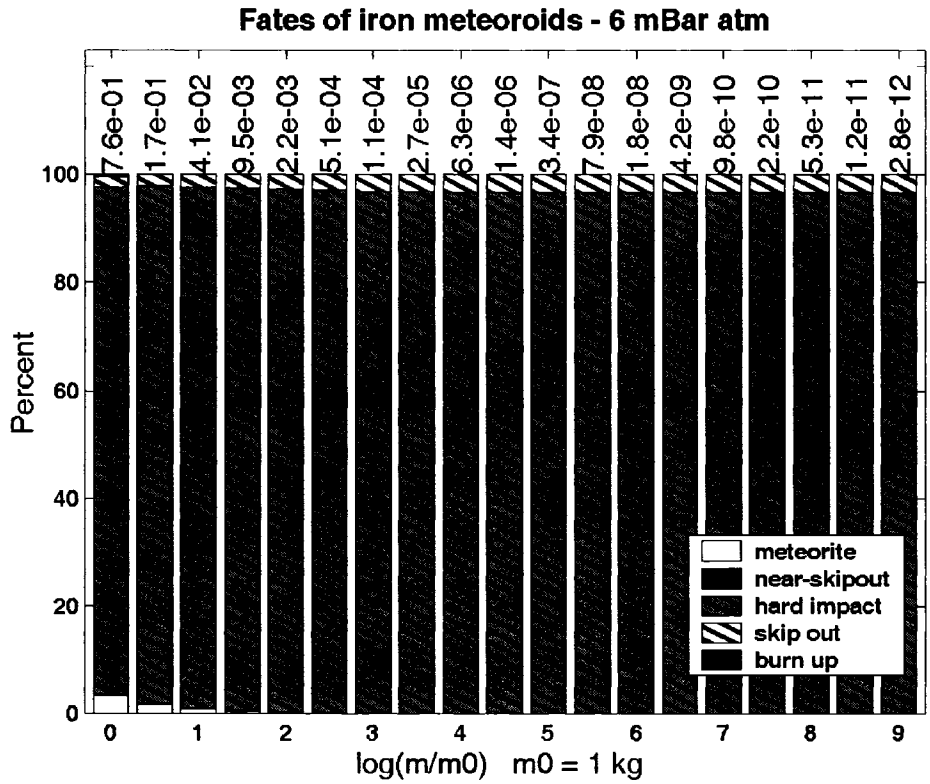

Figure 4.5f: Fates of iron impactors vs. entry mass: 6 mbar atmosphere. Numbers across the top are relative weights of each mass-bin (see Eq. 4.2).

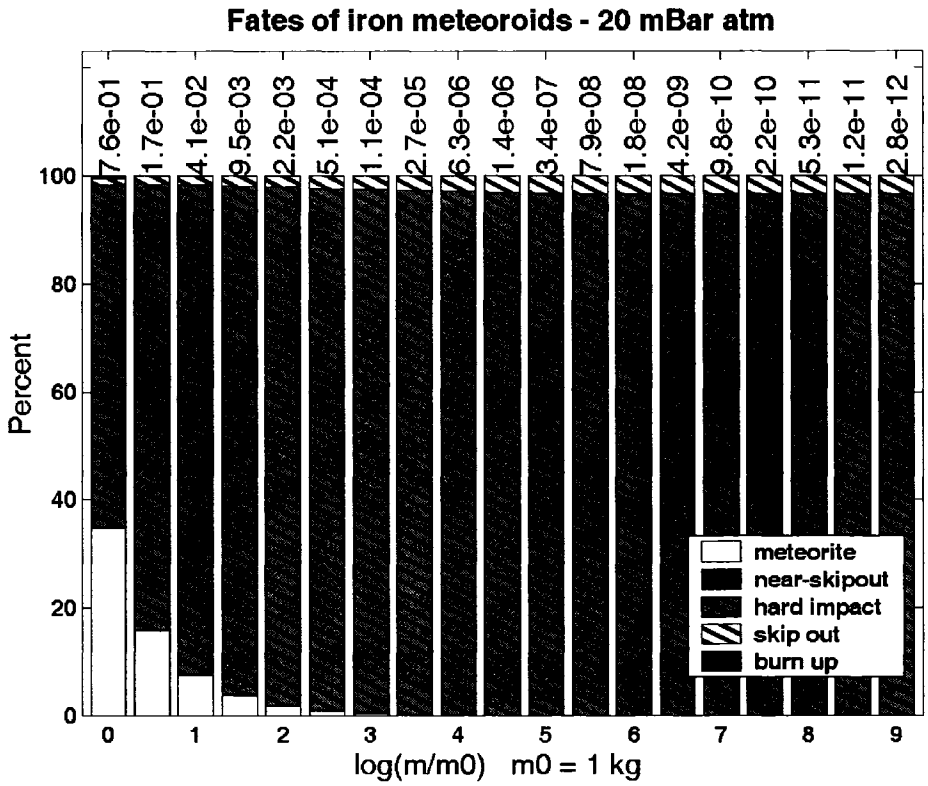

Figure 4.5g: Fates of iron impactors vs. entry mass: 20 mbar atmosphere. Numbers across the top are relative weights of each mass-bin (see Eq. 4.2).

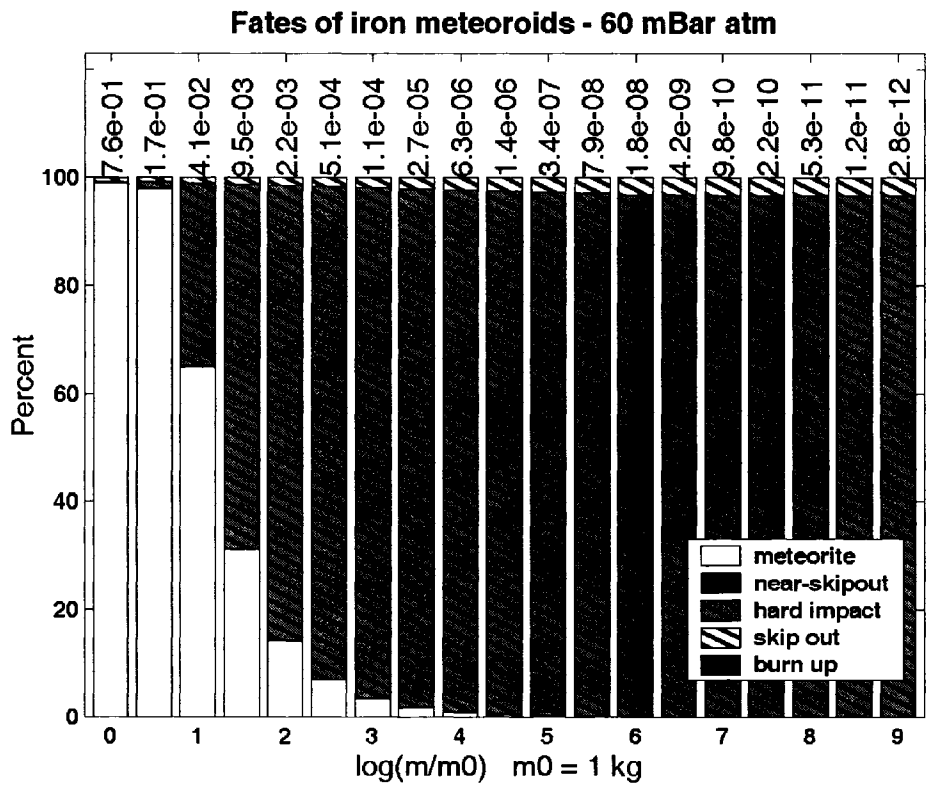

Figure 4.5h: Fates of iron impactors vs. entry mass: 60 mbar atmosphere. Numbers across the top are relative weights of each mass-bin (see Eq. 4.2).

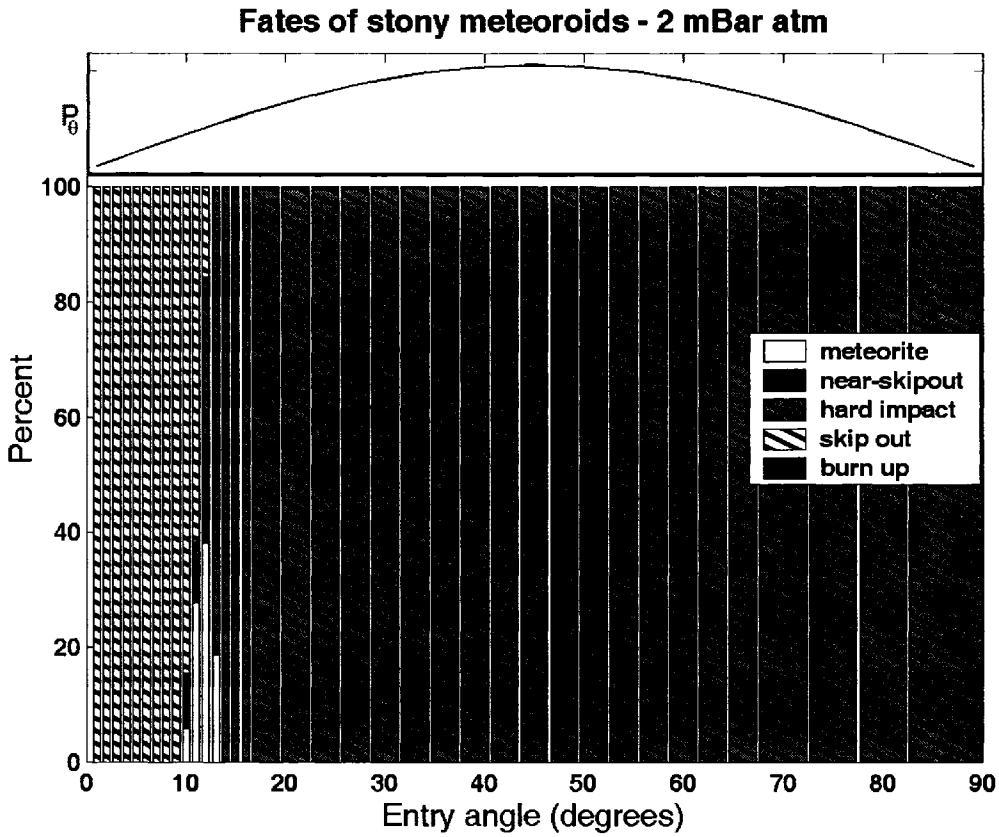

Figure 4.6a: Fates of stony impactors vs. entry angle: 2 mbar atmosphere. The entry-angle weight distribution is plotted across the top of the histogram (see Eq. 4.4).

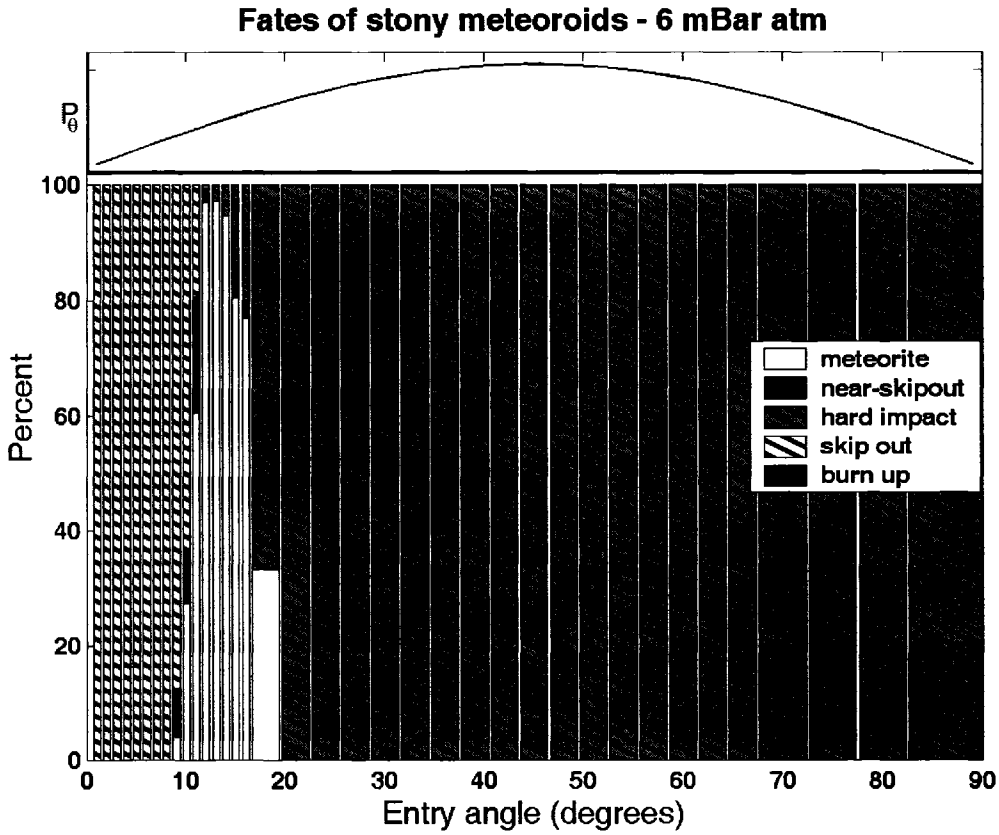

Figure 4.6b: Fates of stony impactors vs. entry angle: 6 mbar atmosphere. The entry-angle weight distribution is plotted across the top of the histogram (see Eq. 4.4).

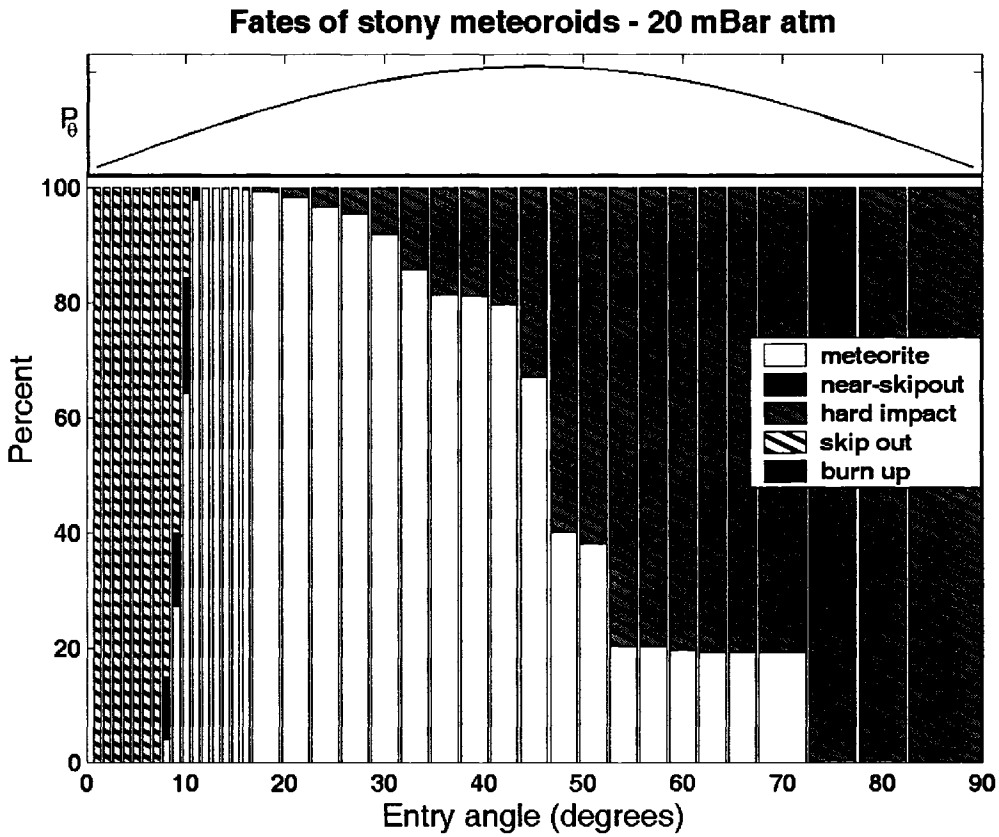

Figure 4.6c: Fates of stony impactors vs. entry angle: 20 mbar atmosphere. The entry-angle weight distribution is plotted across the top of the histogram (see Eq. 4.4).

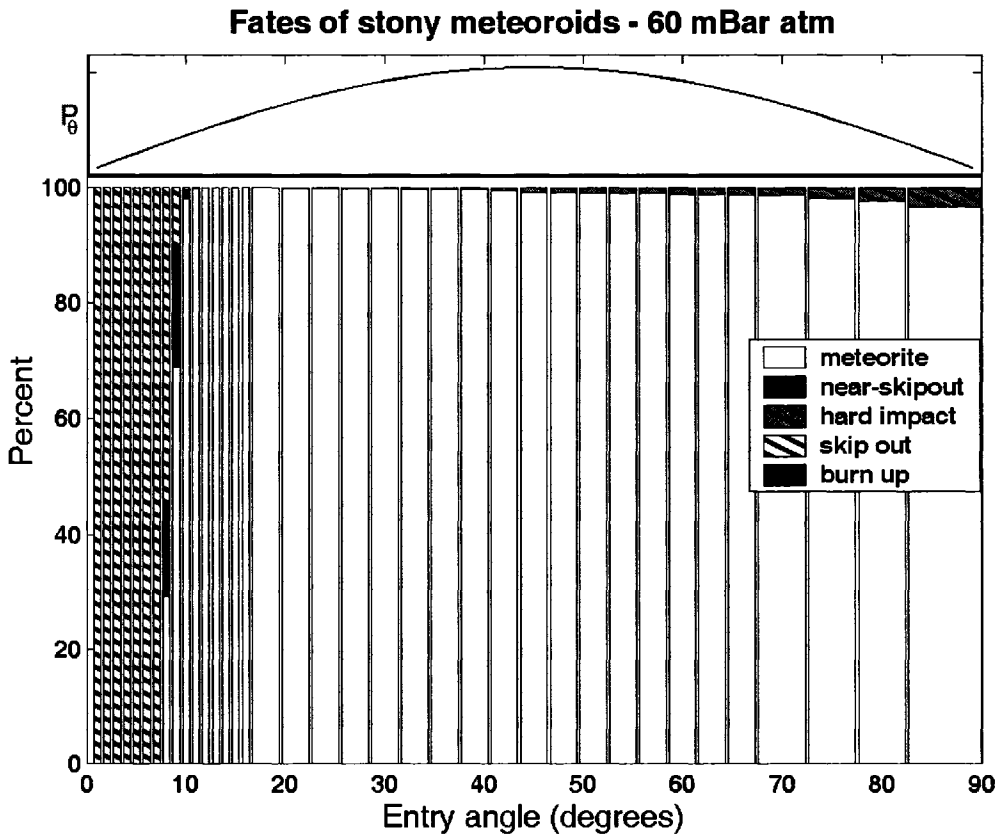

Figure 4.6d: Fates of stony impactors vs. entry angle: 60 mbar atmosphere. The entry-angle weight distribution is plotted across the top of the histogram (see Eq. 4.4).

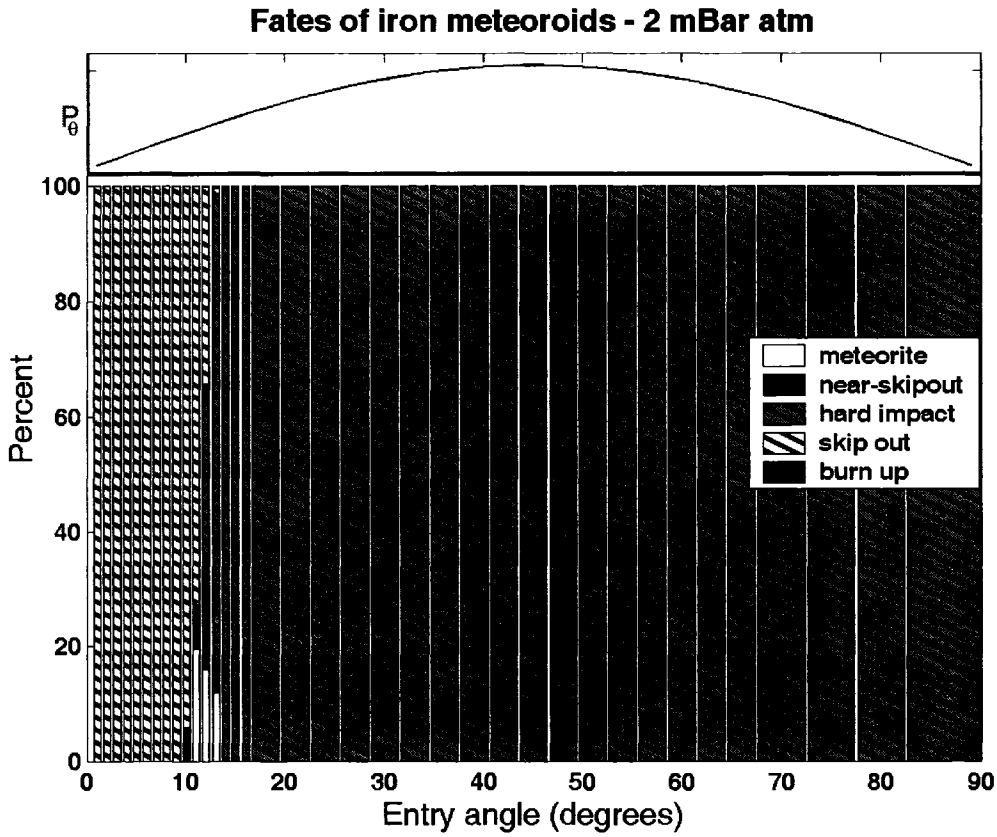

Figure 4.6e: Fates of iron impactors vs. entry angle: 2 mbar atmosphere. The entry-angle weight distribution is plotted across the top of the histogram (see Eq. 4.4).

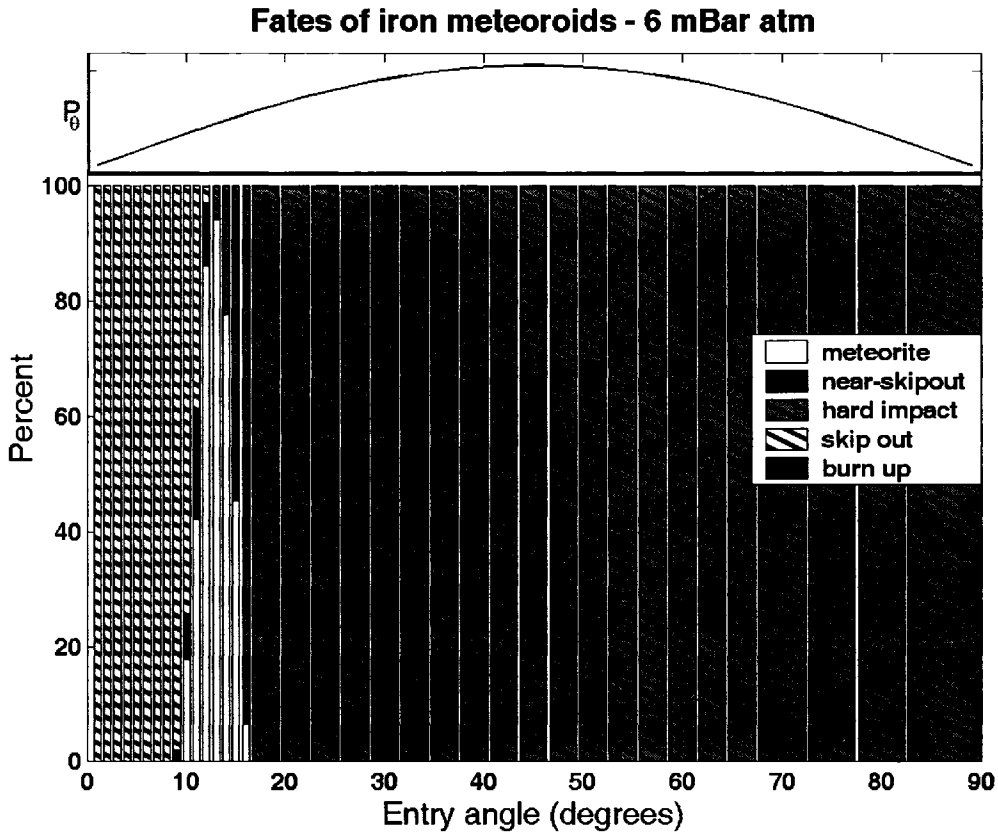

Figure 4.6f: Fates of iron impactors vs. entry angle: 6 mbar atmosphere. The entry-angle weight distribution is plotted across the top of the histogram (see Eq. 4.4).

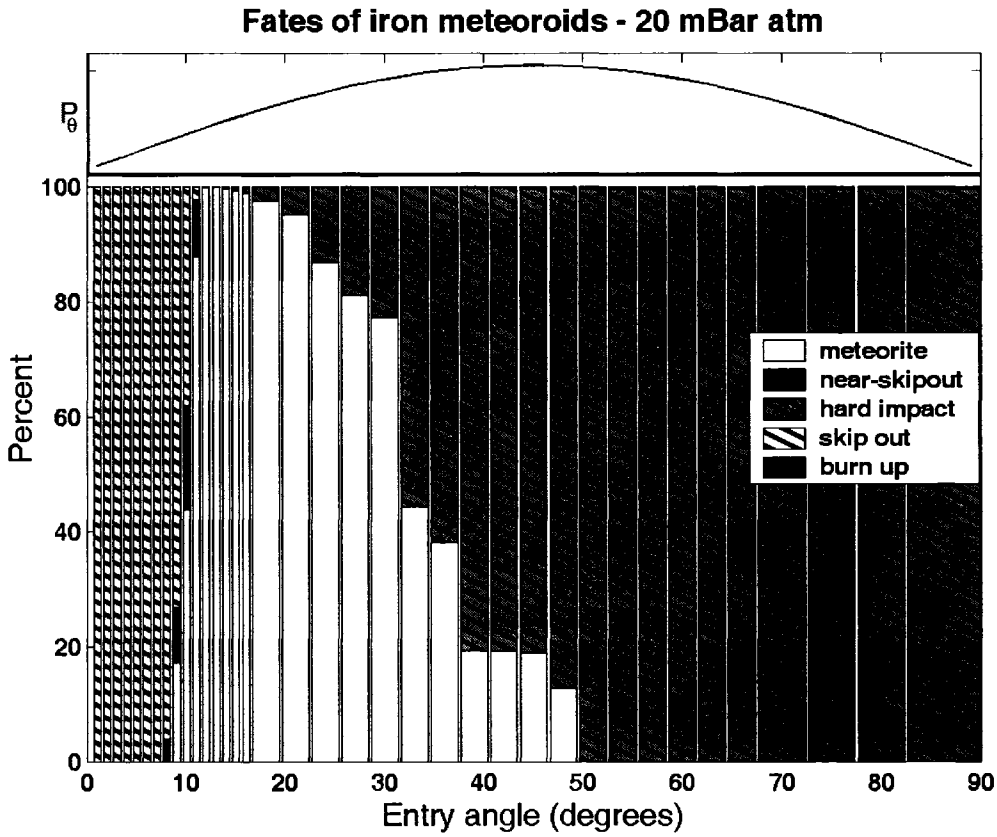

Figure 4.6g: Fates of iron impactors vs. entry angle: 20 mbar atmosphere. The entry-angle weight distribution is plotted across the top of the histogram (see Eq. 4.4).

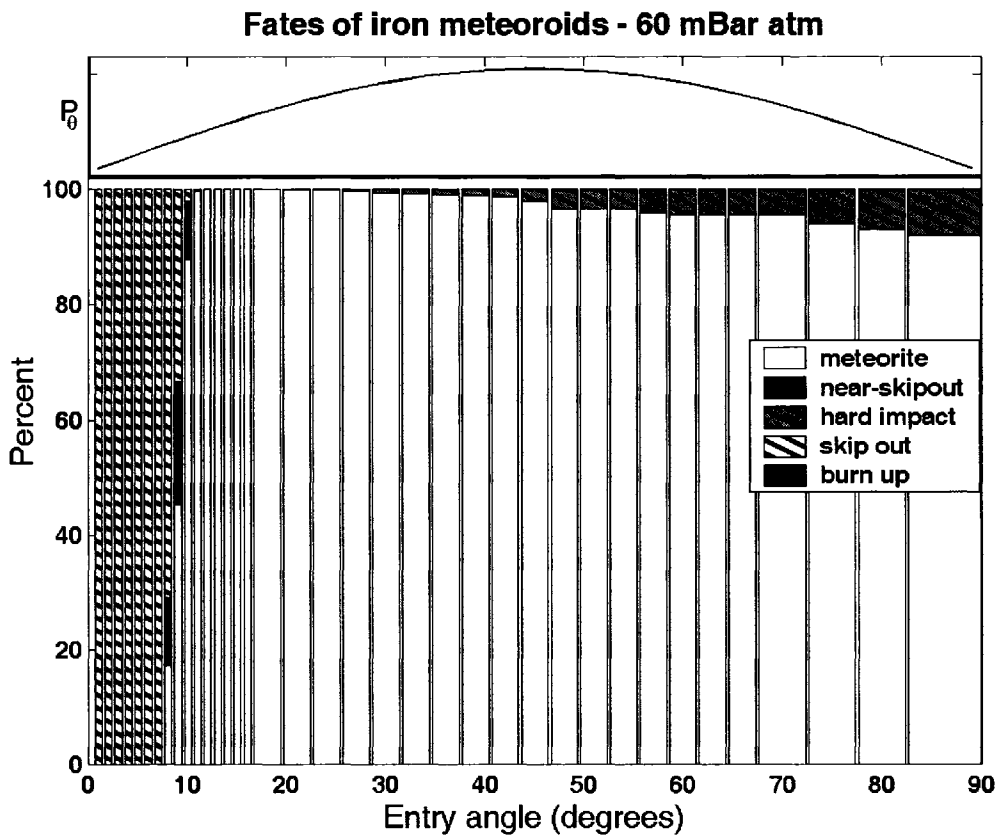

Figure 4.6h: Fates of iron impactors vs. entry angle: 60 mbar atmosphere. The entry-angle weight distribution is plotted across the top of the histogram (see Eq. 4.4).

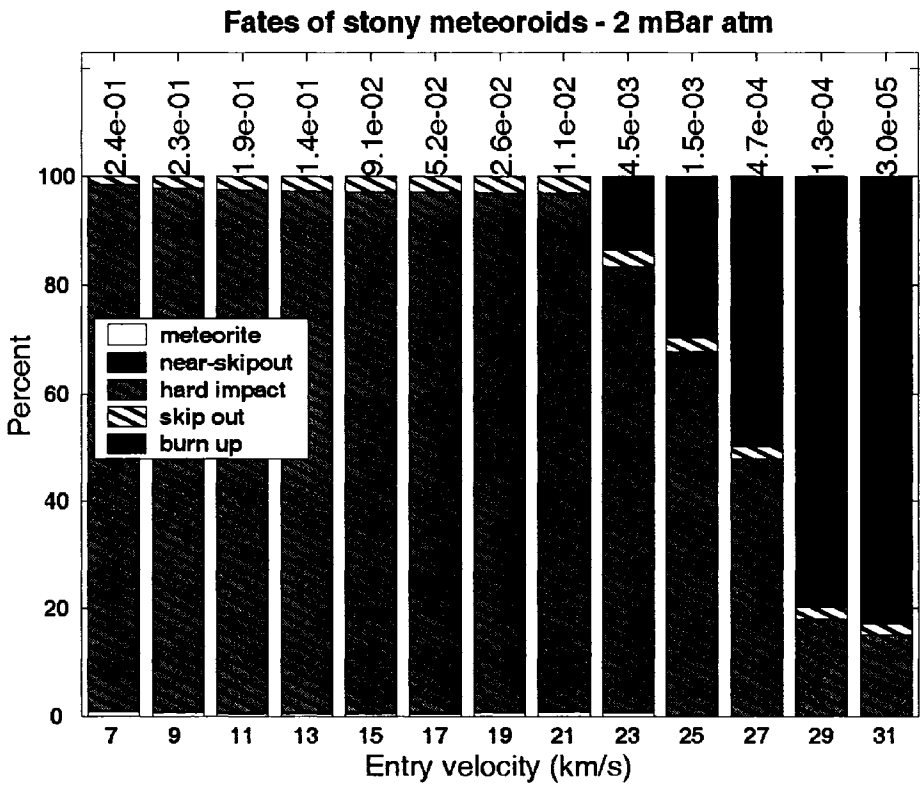

Figure 4.7a: Fates of stony impactors vs. entry velocity: 2 mbar atmosphere. Numbers across the top are relative weights of each velocity-bin (see Eq. 4.3).

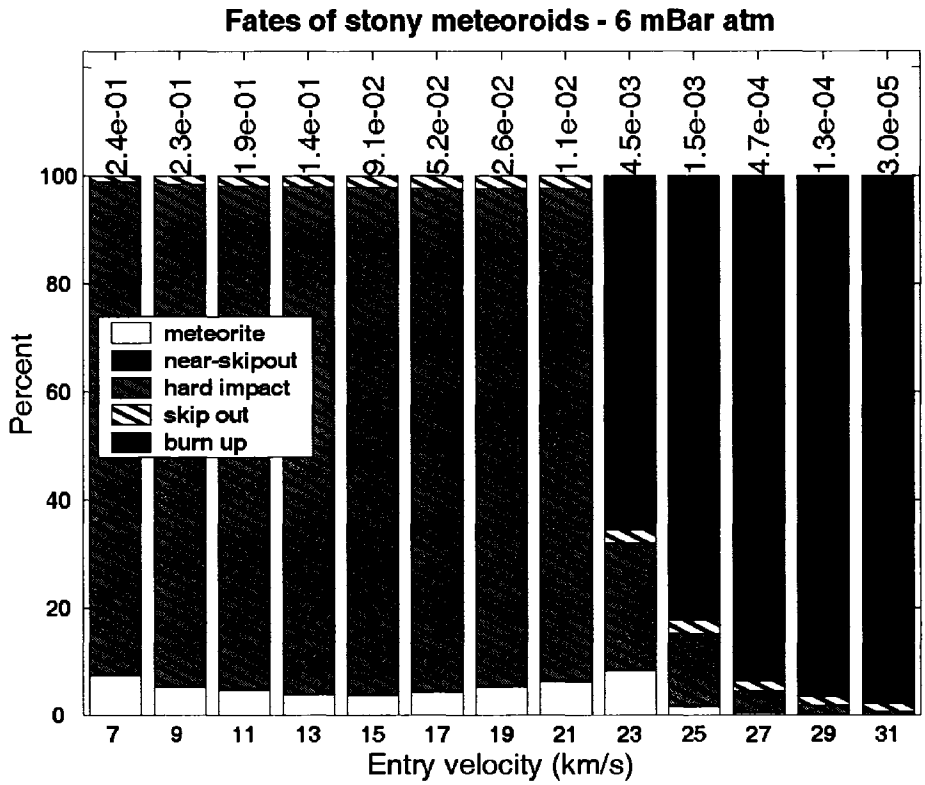

Figure 4.7b: Fates of stony impactors vs. entry velocity: 6 mbar atmosphere. Numbers across the top are relative weights of each velocity-bin (see Eq. 4.3).

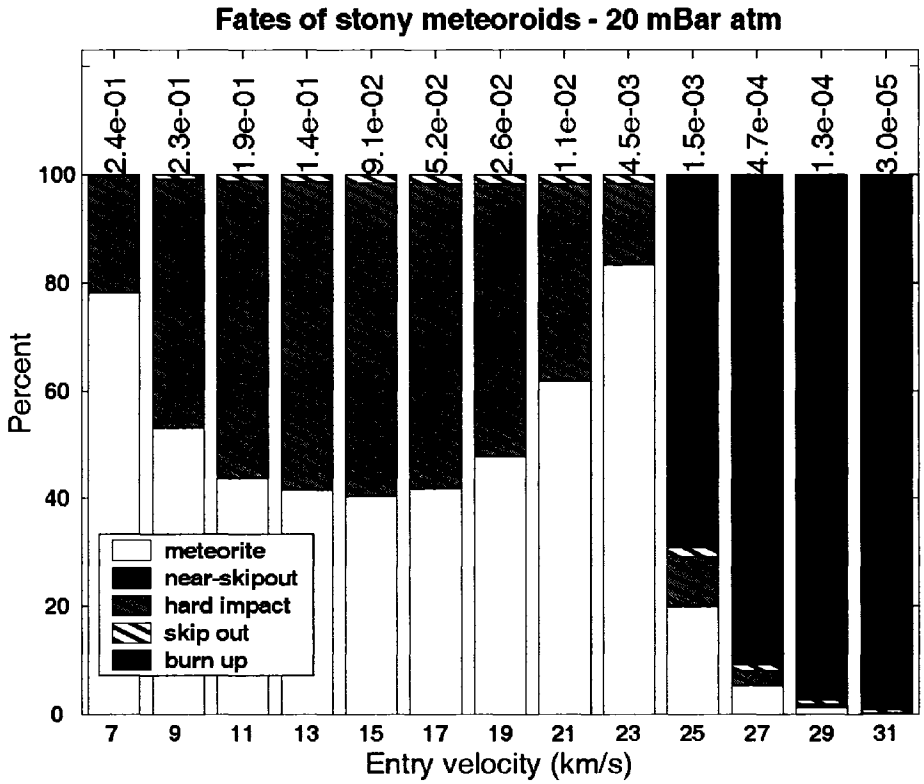

Figure 4.7c: Fates of stony impactors vs. entry velocity: 20 mbar atmosphere. Numbers across the top are relative weights of each velocity-bin (see Eq. 4.3).

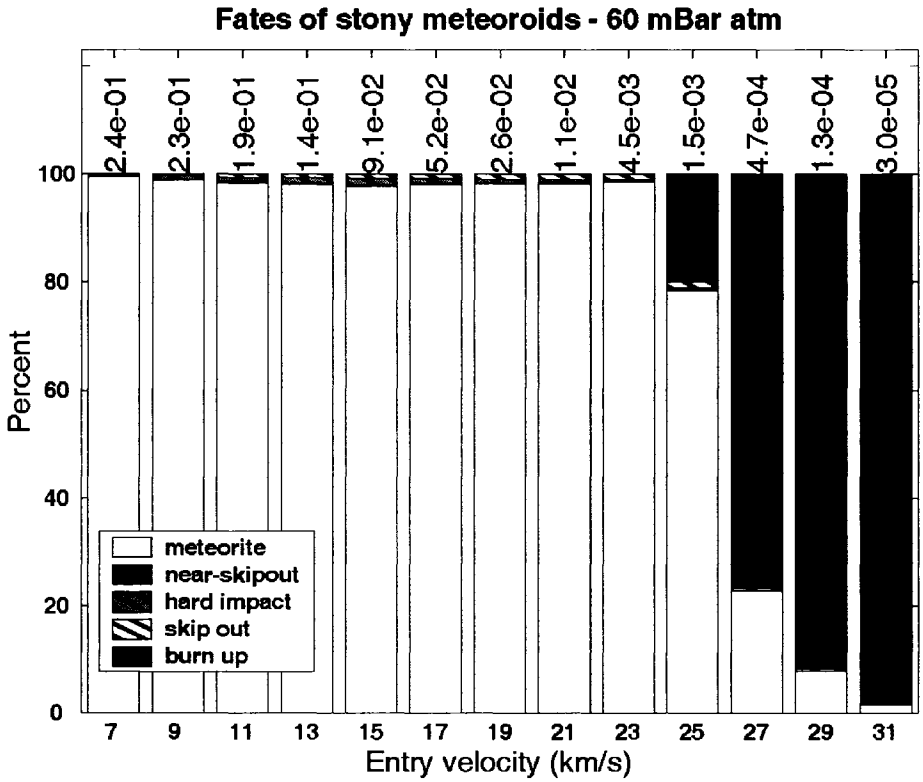

Figure 4.7d: Fates of stony impactors vs. entry velocity: 60 mbar atmosphere. Numbers across the top are relative weights of each velocity-bin (see Eq. 4.3).

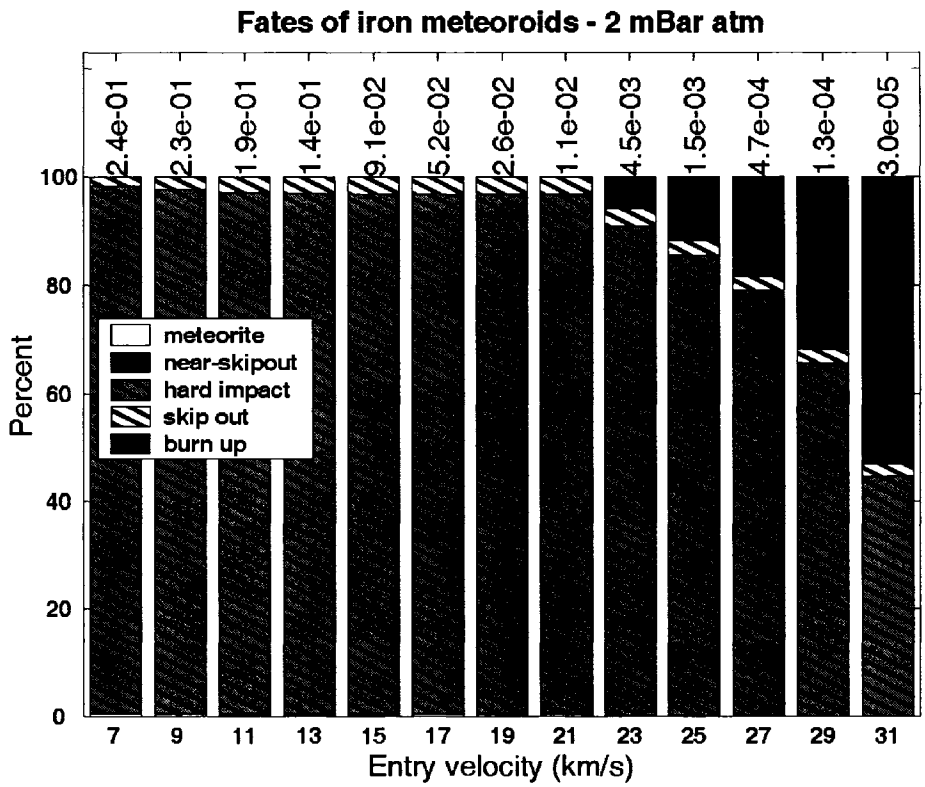

Figures 4.7e: Fates of iron impactors vs. entry velocity: 2 mbar atmosphere. Numbers across the top are relative weights of each velocity-bin (see Eq. 4.3).

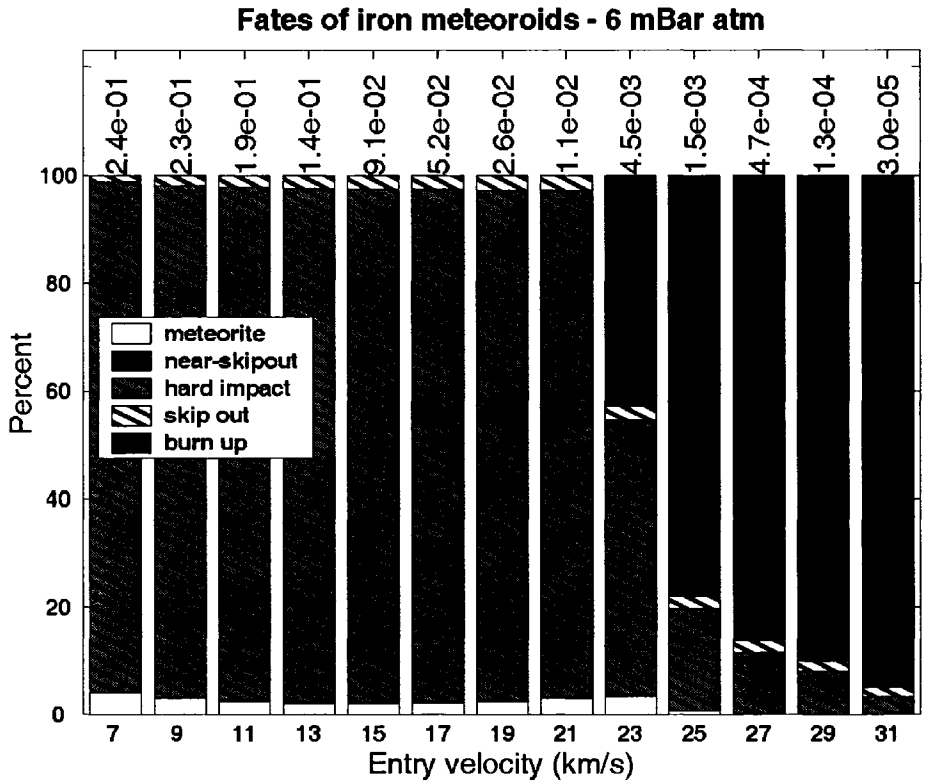

Figures 4.7f: Fates of iron impactors vs. entry velocity: 6 mbar atmosphere. Numbers across the top are relative weights of each velocity-bin (see Eq. 4.3).

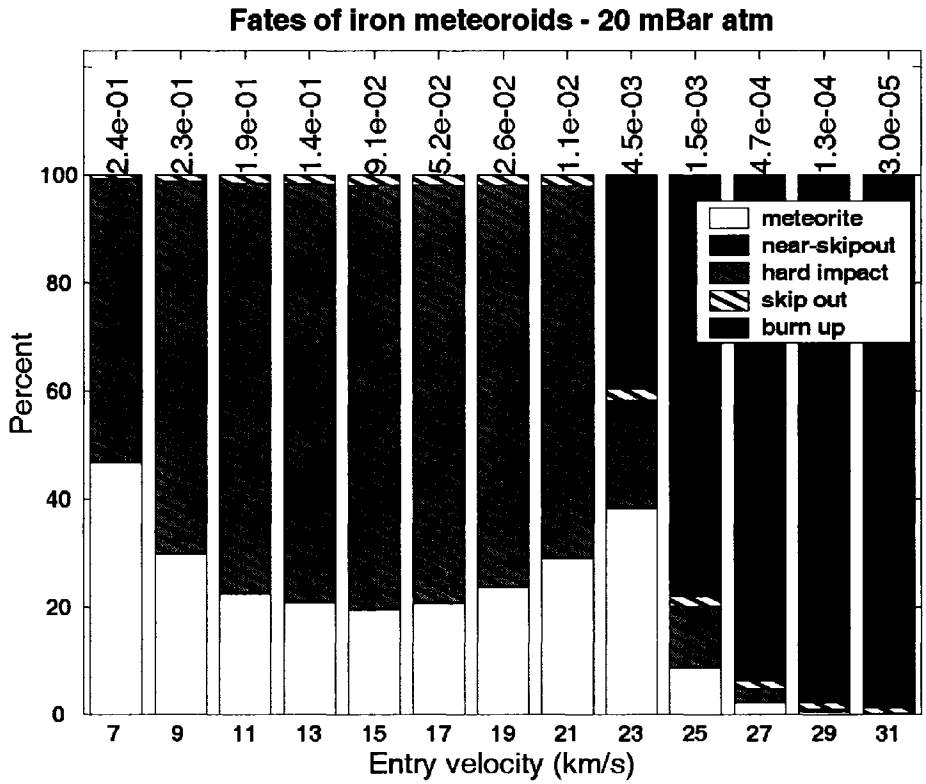

Figures 4.7g: Fates of iron impactors vs. entry velocity: 20 mbar atmosphere. Numbers across the top are relative weights of each velocity-bin (see Eq. 4.3).

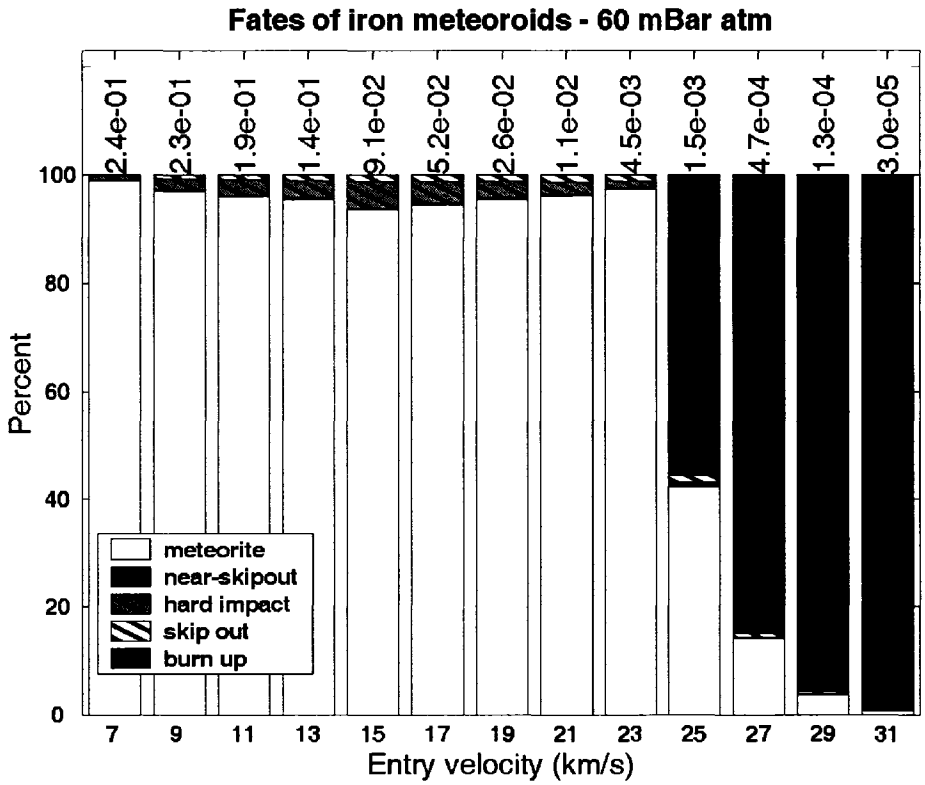

Figures 4.7h: Fates of iron impactors vs. entry velocity: 60 mbar atmosphere. Numbers across the top are relative weights of each velocity-bin (see Eq. 4.3).

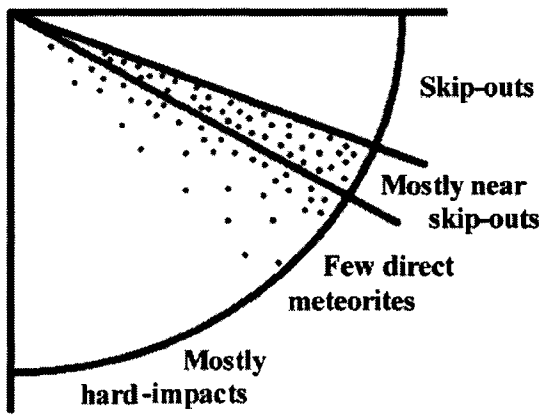

Figure 4.8a: General distributions of outcomes for a 2 mbar martian atmosphere. Illustration of the general distributions of outcomes vs. entry-angle for low-density (2, 6 mbar) martian atmospheres. Speckles indicate the approximate relative intensity of meteorite production as a function of entry-angle. Angles from the horizontal are approximate and are exaggerated for clarity. At near-horizontal entry ($\theta = 0^{\circ}$ to $\sim 11^{\circ}$), almost all iron and stony impactors skip out of the atmosphere (case (a) on Fig. 4.4). At slightly steeper entry-angles, most of them nearly skip out of the atmosphere, but eventually fall back to soft-land on the surface (case (b) on Fig. 4.4); the entry-corridor dominated by near-skipouts is empasized. At steeper angles still, a few stones and irons are slowed to soft-landings, but most penetrate the atmosphere and hard-impact on the surface. Finally, for angles steeper than $\sim 20^{\circ}$, all of the stony and iron meteoroids in the mass-range of interest impact the surface at high velocity.

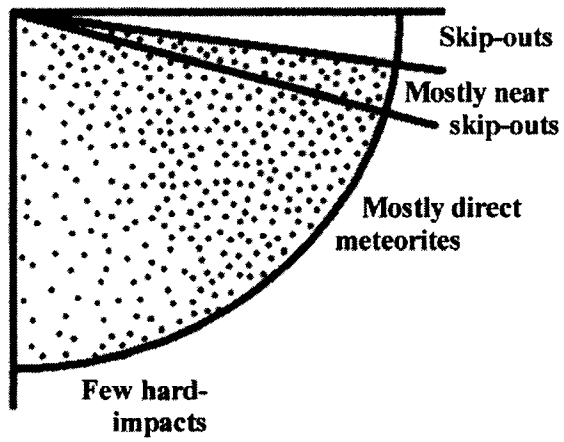

Figure 4.8b: General distributions of outcomes for a 60 mbar martian atmosphere. Illustration of the general distributions of outcomes vs. entry angle for high-density (20, 60 mbar) martian atmospheres. Speckles indicate approximate intensity of meteorite production as a function of entry angle. Angles from the horizontal are approximate and are exaggerated for clarity. For these denser atmospheres, the entry- angle range that results in skip-outs narrows and the corridor dominated by near skip-outs shallows (compare to Fig 4.8a). Many more meteorites are produced by steeper entry-angles, and only a few of the steepest-entering meteoroids hard-impact on the surface.

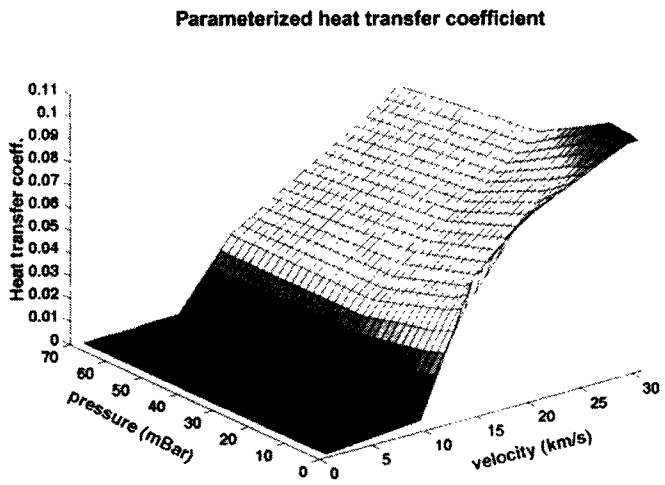

Figure 4.9: The parameterized heat transfer coefficient.

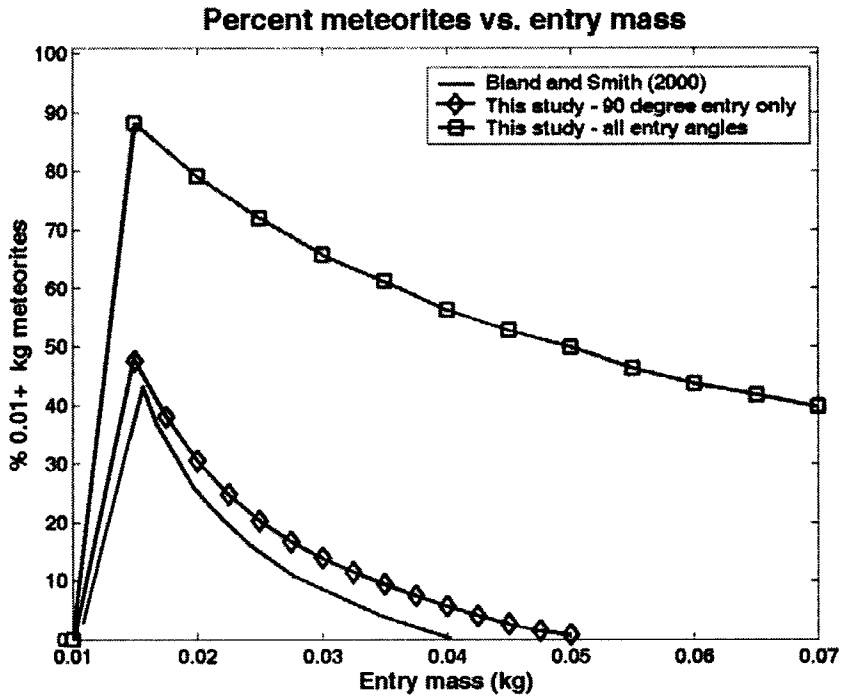

Figure 4.10: Comparison with Bland and Smith (2000). Comparison of small meteorite production using the methods of this study, with results of Bland and Smith (2000). The y-axis is the percent of objects that soft-land with remaining masses of at least 0.01 kg. The lowest curve is equivalent to the m_{min} = 20 g, σ = 0.04 s^2 km^{-2}, impact speed $\leq$ 1.6 km s^{-1} curve on Fig. 1 in Bland and Smith (2000).

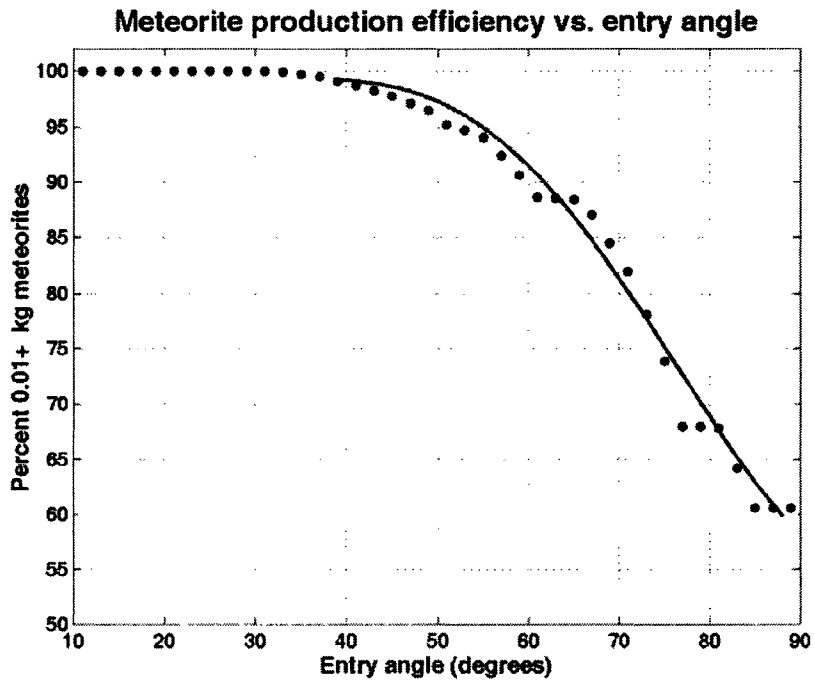

Figure 4.11: Meteorite production efficiency vs. entry angle. Meteorite production efficiency for 0.01 kg $\leq m_o \leq$ 0.15 kg impactors vs. entry angle. Essentially all objects in this mass-range, and entry angle less than 40° produce meteorites. The 'best-fit' curve is fit to the $\theta_o > 40^{\circ}$ data only.

Chapter 5
Conclusions

In Chapter 2 of this work a new method of determining the depth of an impact crater from the length of shadow cast within it was developed and demonstrated. Like all shadow techniques, this method is limited to imagery obtained when the Sun is low enough to cast shadows. Since it depends upon the shadow shape, as well as its length, the method it is also limited, at least for now, to nadir-looking or ortho-rectified imagery.

However, the new method does not suffer from the limitation that the old shadow method does, that the shadow-front must pass through the center of the crater. It does not require multiple images of the subject crater as stereogrammetry does, nor is it affected by albedo variations, as is photoclinometry. It is very simple to use, and is not computationally intensive, as are both stereogrammetry and photoclinometry. The method also recovers crater morphology information from the shadow shape and uses it to determine which of three different equation for the depth is appropriate. Conical and parabolic cross-sections, flat floors, and rounded rims can now be detected, by inspection, from the shape of the shadow in a crater.

In Chapters 3 and 4, an original method of simulating the effects of bombardment, by large numbers of impactors, on planetary surfaces was developed and applied to Mars. Short of 'brute force', Monte-Carlo-type methods (which are computationally impractical in this case), this technique is currently the only way of handling this problem. The approach is very general in nature and could be easily applied to the same problem for planets other than Mars, and maybe even adapted to other scientific problems.

Using this method I constructed a computer simulation to assess the fate of a large population of impactors interacting with the present and predicted past and future martian atmospheres, and determine its effects on Mars's surface. I found that even Mars's present atmosphere significantly reduces crater production rates at small diameters (< 30 m); past denser atmospheres would have affected cratering even more strongly, and to considerably larger diameters. These effects are increased if the inner solar system's small

impactor population contains significant numbers of icy, cometary bodies. Because of these atmospheric reductions in cratering rates, martian surface ages derived from counts of craters of less than about 250 m in diameter may be underestimated.

Because small-cratering rates depend upon atmospheric density, evidence of recent atmospheric variations may be detectable in the martian small cratering record, possibly with future higher-resolution imagers. For example, the absence of a detectable 'turndown' in crater size-frequency distributions at the meter scale may provide evidence of a recent period of very low atmospheric density.

In Chapter 4 I expanded upon methods developed in Chapter 3 to investigate martian meteorite production rates, their dependence upon variations in Mars's atmosphere, and the ranges of mass, velocity and entry-angle that produce meteorites.
It was determined that almost all of the stony and iron objects in the mass-range of interest (1 kg $\leq m_o \leq 10^9$ kg) reach the surface, where they either hard-impact or soft-land. Very few burn up in, or skip out of, any of the atmospheres studied here.

For the low-density (2, 6 mbar) atmospheres, stone and iron meteorite production is confined to relatively narrow 'entry corridors' steeper than 7° and shallower than 20°, and masses less than 100 kg. These ranges expand for the denser (20, 60 mbar) atmospheres, which can land meteorites up to ~10,000 kg in mass; any entry angle steeper than 7° can produce meteorites under the 60 mbar atmosphere. Meteorite production is found to increase strongly, and impact cratering correspondingly decreases strongly, with increasing atmospheric density. When the atmospheric surface pressure increases to 60 mbar nearly all of the irons and stones in the mass-range of interest soft-land and become meteorites.

The results of this investigation were used to estimate the entry-parameter values that could have produced 'Heat Shield Rock'. I found that Heat Shield Rock may have been produced by the present martian atmosphere, but more likely landed under a denser one. It probably entered the atmosphere at a shallow angle ($10^\circ < \theta_o < 25^\circ$), relatively high velocity ($v >$ ~15 km s^{-1}) and with a mass of at least 60 kg. It most likely struck

Mars's surface at a shallow enough angle that it 'ricocheted' upon impact, and doesn't now lie where it impacted.

Each of the projects that constitute this thesis suggest further work that I may pursue in the future. For example, it may be possible to generalize the shadow-measurement technique developed in Chapter 2 beyond the two fundamental cross sectional types (conical and parabolic) treated there. If so it will be possible to apply this method to many craters whose cross sections fall between the conical and the parabolic, and even ones that fall outside of these shapes. In this way, the mathematical description of almost all simple impact crater shapes may be reduced to the specification of just two or three parameters.

The methods developed and employed in Chapters 3 and 4 for the simulation of a large population of impactors may be usefully applied to other planetary bodies, such as Earth, Venus and Titan, or to Mars under even denser-atmosphere conditions than treated here (and which may have prevailed very early in Mars's history). However, for bodies with atmospheres much denser than that of present-day Mars, a better way of dealing with fragmentation must be found than was used herein. I was able to get away without including crater-clusters in Chapter 3, and without including fragmentation at all in Chapter 4, only because results of Chapter 3 showed that few carbonaceous chondrites and almost no stones or irons break up in Mars's atmosphere. This would not be true in much denser atmospheres, and fragmentation followed by multiple independent crater-forming impacts or multiple meteorite falls would be the norm on such worlds, rather than the exception as on Mars.

Finally, these methods may be useful in completely different problems, where the net effects of large numbers of similar events are of interest. One such problem that comes to mind is the evolution of the mass-frequency distribution of asteroids in the asteroid belt.

Appendix - Runge-Kutta code used in atmospheric entry model

In the projects associated with both Chapters 3 and 4 the Runge-Kutta 4th order method is used to integrate the equations of motion of meteor flight. Details of this method can be found in practically any text on numerical methods. The annotated MATLAB code specifically written for, and employed in this thesis is reproduced here.

```
for j1=1:100000                              %Begin integration time step

   %GET ABLATION COEFFICIENT:
   ch=interp2(vdata,zdata,Chdata,v1,z1);  %"look up" heat transfer coef
   c3=ch/(2.0*Q);                         %calc. ablation coefficient

   %CALCULATE 1ST ROUND OF R-K4 COEFFICIENTS:
   kv1=-0.5*Cd*rhog*area*v1*v1*dt/m1+g0*sin(th1)*dt;
   kth1=(g0*cos(th1)*dt/v1)-v1*cos(th1)*dt/(z1+Rp);
   km1=-c3*rhog*area*v1*v1*v1*dt;
   kz1=-v1*sin(th1)*dt;

   %CALCULATE 1ST ROUND OF PARAMETERS (ATM DENSITY, XSECTION AREA:
   rhog=c1*exp(-(z1+kz1/2.0)/H);
   area=c2*((m1+km1/2.0)^(2.0/3.0));

   %CALCULATE 2ND ROUND OF R-K4 COEFFICIENTS:
   kv2=0.5*Cd*rhog*area*(v1+kv1/2.0)*(v1+kv1/2.0)*dt/(m1+km1/2.0)+....
      g0*sin(th1+kth1/2.0)*dt;
   kth2=g0*cos(th1+kth1/2.0)*dt/(v1+kv1/2.0)-(v1+kv1/2.0)*....
      cos(th1+kth1/2.0)*dt/((z1+kz1/2.0)+Rp);
   km2=-c3*rhog*area*(v1+kv1/2.0)*(v1+kv1/2.0)*(v1+kv1/2.0)*dt;
   kz2=-(v1+kv1/2.0)*sin(th1+kth1/2.0)*dt;

   %CALCULATE 2ND ROUND OF PARAMETERS (ATM DENSITY, XSECTION AREA:
   rhog=c1*exp(-(z1+kz2/2.0)/H);
   area=c2*((m1+km2/2.0)^(2.0/3.0));

   %CALCULATE 3RD ROUND OF R-K4 COEFFICIENTS:
   kv3=0.5*Cd*rhog*area*(v1+kv2/2.0)*(v1+kv2/2.0)*dt/(m1+km2/2.0)+....
      g0*sin(th1+kth2/2.0)*dt;
   kth3=g0*cos(th1+kth2/2.0)*dt/(v1+kv2/2.0)-(v1+kv2/2.0)*...
      cos(th1+kth2/2.0)*dt/((z1+kz2/2.0)+Rp);
   km3=-c3*rhog*area*(v1+kv2/2.0)*(v1+kv2/2.0)*(v1+kv2/2.0)*dt;
   kz3=-(v1+kv2/2.0)*sin(th1+kth2/2.0)*dt;

   %CALCULATE 3RD ROUND OF PARAMETERS (ATM DENSITY, XSECTION AREA:
   rhog=c1*exp(-(z1+kz3)/H);
   area=c2*((m1+km3)^(2.0/3.0));
```

```
    %CALCULATE 4TH ROUND OF R-K4 COEFFICIENTS:
    kv4=0.5*Cd*rhog*area*(v1+kv3)*(v1+kv3)*dt/(m1+km3)+....
       g0*sin(th1+kth1)*dt;


    kth4=g0*cos(th1+kth3)*dt/(v1+kv3)(v1+kv3)*cos(th1+kth3)*....
       dt/((z1+kz3)+Rp);
    km4=-c3*rhog*area*(v1+kv3)*(v1+kv3)*(v1+kv3)*dt;
    kz4=-(v1+kv3)*sin(th1+kth3)*dt;
    %CALCULATE FINAL VALUES OF VARIABLES:
    m2=m1+(km1+2.0*km2+2.0*km3+km4)/6.0;
    v2=v1+(kv1+2.0*kv2+2.0*kv3+kv4)/6.0;
    z2=z1+(kz1+2.0*kz2+2.0*kz3+kz4)/6.0;
    th2=th1+(kth1+2.0*kth2+2.0*kth3+kth4)/6.0;
    %END OF RUNGE-KUTTA STUFF

    %CALCULATE NEW ATM. DENSITY AND XSECTION:
    rhog=c1*exp(-z2/H);
    area=c2*((m2)^(2.0/3.0));

    %CALCULATE NEW X, VX, VZ, RADIAL COORDINATES AND DYNAMIC PRESSURE:
    vx2=v2*cos(th2);
    vz2=-v2*sin(th2);
    vxave=(vx2+vx1)/2.0;
    x2=x1+vxave*dt;
    Pdyn=rhog*v2*v2/2.0;     %new dynamic pressure
    dlong=(x2-x1)/radius1;   %dlongitude
    longitude2=longitude1+dlong;  %new areocentric longitude
    radius2=z2+Rp;           %new areocentric radius

    %CHECK IF FINISHED:
    Outcome;                 %run script to see if outcome reached

    %IF NOT, RESET ACTIVE VARIABLES FOR NEXT R-K TIME STEP:
    m1=m2;
    v1=v2;
    z1=z2;
    th1=th2;
    x1=x2;
    vx1=vx2;
    vz1=vz2;
    radius1=radius2;
    longitude1=longitude2;

end   %end time step loop
```

Definitions of important variables:

`j1` = Loop control variable.

`ch` = Heat transfer coefficient.

`c3` = Ablation coefficient.

`vdata zdata Chdata` = Heat transfer coefficient lookup table data.

`g0` = Mars surface gravity.

`x1 x2 z1 z2` = Local-horizontal, cartesian coordinates before and after time step.

`m1 m2 v1 v2 th1 th2` = Mass, velocity and trajectory angle before and after time step.

`vx1 vx2 vz1 vz2` = Velocity components before and after time step.

`rhog` = Ambient atmospheric density.

`Pdyn` = Dynamic ('stagnation point') pressure.

`area` = Impactor's cross-sectional area.

`radius1 radius2 longitude1 longitude2` = Areocentric radial coordinates before and after time step.

All variables beginning with `'k'` = Runge-Kutta coefficients.